OULU 2024
C 961

ACTA UNIVERSITATIS OULUENSIS

Muhammad Asad Ullah

MACHINE-TYPE DIRECT-TO-SATELLITE COMMUNICATIONS

MODELING AND PERFORMANCE ANALYSIS

UNIVERSITY OF OULU GRADUATE SCHOOL;
UNIVERSITY OF OULU,
FACULTY OF INFORMATION TECHNOLOGY AND ELECTRICAL ENGINEERING

ACTA UNIVERSITATIS OULUENSIS
C Technica 961

MUHAMMAD ASAD ULLAH

MACHINE-TYPE DIRECT-TO-SATELLITE COMMUNICATIONS

Modeling and Performance Analysis

Academic dissertation to be presented with the assent of the Doctoral Programme Committee of Information Technology and Electrical Engineering of the University of Oulu for public defence in the OP auditorium (L10), Linnanmaa, on 27 September 2024, at 12 noon

UNIVERSITY OF OULU, OULU 2024

Acta Univ. Oul. C 961, 2024

Supervised by
Associate Professor Konstantin Mikhaylov
Associate Professor Hirley Alves

Reviewed by
Professor Mohamed-Slim Alouini
Professor Juan A. Fraire

Opponent
Professor Symeon Chatzinotas

ISBN 978-952-62-4199-9 (Paperback)
ISBN 978-952-62-4200-2 (PDF)

ISSN 0355-3213 (Printed)
ISSN 1796-2226 (Online)

Cover Design
Raimo Ahonen

PUNAMUSTA
TAMPERE 2024

Asad Ullah, Muhammad, Machine-type Direct-to-Satellite Communications. Modeling and Performance Analysis
University of Oulu Graduate School; University of Oulu, Faculty of Information Technology and Electrical Engineering
Acta Univ. Oul. C 961, 2024
University of Oulu, P.O. Box 8000, FI-90014 University of Oulu, Finland

Abstract

Despite the massive progress in 5G and beyond systems, the deployed terrestrial networks do not provide ubiquitous coverage even on land; the situation is even worse in the open sea, which covers 70% of the Earth's surface. This disparity illustrates a significant digital divide. To address this vital need, global wireless coverage stands as one of the most crucial requirements for the upcoming 6G wireless networks to offer connectivity to both human and IoT machines.

This thesis advocates massive machine-type communication (mMTC) and low Earth orbit (LEO) satellite integration to enable direct connectivity from low-cost, low-power end devices to satellites without relying on a terrestrial network. This emerging form of new connectivity, machine-type direct-to-satellite (DtS) communications, promises to bridge the digital divide. However, DtS presents exciting challenges which need to be carefully examined and addressed. Among these challenges is LEO satellite mobility, which introduces a strong Doppler effect and time-varying channel conditions. Similarly, the long link distance ranging from hundreds to thousands of kilometers and the wide satellite footprint contributes to high propagation losses and massive interference, respectively. Additionally, terrestrial end devices possess limited energy resources. Therefore, successful DtS operation requires high energy efficiency, allowing the low-power signals to reach satellites orbiting thousands of kilometers away from Earth.

Motivated by the low-power and long-range capabilities of LoRaWAN, this thesis selected LoRa and LR-FHSS-based solutions for the modeling. This thesis develops novel Monte Carlo simulation and analytical models for DtS communications performance analysis. The results confirmed the feasibility and potential of both LoRa and LR-FHSS for DtS communications and highlighted the trade-off of different parameter configurations. In summary, LR-FHSS reveals better performance compared to LoRa, primarily due to its high sensitivity, robust Doppler resistance, and increased capacity, making it a suitable choice for DtS communications.

LR-FHSS end devices are expected to be powered by battery, therefore, it is vital to investigate the energy consumption of LR-FHSS. This work conducts experiments using real-life end devices and measures the LR-FHSS air-time and current consumption. We leverage these empirical measurement results to develop analytical models which give us the energy efficiency and battery lifetime of LR-FHSS end devices. LR-FHSS air-time model is highly important for accurate collisions modeling and scalability analysis.

Keywords: direct-to-satellite, global connectivity, internet-of-things, LEO, LoRa, LoRaWAN, LR-FHSS, mMTC, modeling, remote areas

Asad Ullah, Muhammad, Konetyyppinen suora satelliittiviestintä. Mallinnus ja suorituskykyanalyysi
Oulun yliopiston tutkijakoulu; Oulun yliopisto, tieto- ja sähkötekniikan tiedekunta
Acta Univ. Oul. C 961, 2024
Oulun yliopisto, PL 8000, 90014 Oulun yliopisto

Tiivistelmä

Vaikka 5G- ja uudemmissa järjestelmissä on edistytty merkittävästi, nykyiset maanpäälliset verkot eivät ulotu kaikkialle edes maalla, saati avomerellä, jota on 70 prosenttia maapallon pinta-alasta. Tästä erosta voidaan havaita merkittävä digitaalinen kahtiajako. Tulevien langattomien 6G-verkkojen tärkeimpiä vaatimuksia on maailmanlaajuinen kuuluvuus, jotta tähän elintärkeään tarpeeseen voidaan vastata ja yhdistää sekä ihmiset että koneet.

Esitän tässä tutkielmassa, miten massiivisen laitteiden välisen viestinnän (massive machine-type communication, MMTC) ja matalan kiertoradan (low earth orbit, LEO) satelliittien avulla edulliset ja pienitehoiset päätelaitteet voivat saada satelliittiyhteyden ilman maanpäällistä verkkoa. Tämä uusi yhteysmuoto, suora laitteiden välinen satelliittiviestintä (direct-to-satellite, DtS), voi kuroa edellä mainitun digitaalisen kuilun umpeen. DtS-tekniikkaan liittyy kuitenkin mielenkiintoisia haasteita. Haasteena on muun muassa LEO-satelliittien liikkuvuus, mikä aiheuttaa voimakasta Doppler-ilmiötä ja ajassa vaihtelevia kanavan olosuhteita. Samoin yhteyden huomattava pituus (satoja tai tuhansia kilometrejä) ja laaja satelliitin peittoalue aiheuttavat suurta etenemisvaimennusta ja häiriötä tässä järjestyksessä. Lisäksi maanpäällisten päätelaitteiden energiabudjetti on rajallinen. Näin ollen onnistunut DtS:n käyttö edellyttää erinomaista energiatehokkuutta.

LoRaWAN-teknologian pienet tehovaatimukset ja pitkä kantama saivat minut valitsemaan tämän tutkielman mallinnukseen ratkaisut, jotka perustuvat LoRa- ja LR-FHSS-teknologiaan. Kehitän tutkielmassa uusia Monte Carlo -simulaatioita ja analyyttisiä malleja DtS-tietoliikenteen suorituskyvyn analysoimiseksi. Tulosten perusteella sekä LoRa- että LR-FHSS-teknologiassa on potentiaalia ja ne ovat toteuttamiskelpoisia DtS-tiedonsiirtoon. Tulokset myös korostavat erilaisista parametreista seuraavia kompromisseja. Yhteenvetona totean, että LR-FHSS:n suorituskyky oli LoRa-teknologiaa parempi, ensisijaisesti sen suuren herkkyyden, hyvän Doppler-ilmiön siedon ja suuremman kapasiteetin ansiosta, minkä ansiosta se on sopiva DtS-tiedonsiirtoon.

LR-FHSS-päätelaitteet ovat oletusarvoisesti akkukäyttöisiä, joten LR-FHSS-teknologian energiankulutuksen tutkiminen on ehdottoman tärkeää. Tein tässä tutkielmassa kokeita oikeilla päätelaitteilla ja mittasin LR-FHSS-teknologian lähetysaikaa ja virrankulutusta. Sovelsin empiirisiä mittaustuloksia sellaisten analyyttisten mallien kehittämiseen, joilla saatoin päätellä LR-FHSS-päätelaitteiden energiatehokkuuden ja akkukeston. LR-FHSS-lähetysaikamalli on tärkeä työkalu tarkkaan törmäysten mallintamiseen ja skaalautuvuuden analysoimiseen.

Asiasanat: esineiden internet, LoRa, LoRaWAN, LR-FHSS, maailmanlaajuinen kuuluvuus, mallinnus, matala Maan kiertorata, mMTC, suoraan satelliittiin, syrjäiset alueet

To my family

Acknowledgements

The research for this thesis was primarily conducted at the Center for Wireless Communications (CWC) at the University of Oulu, Finland, from September 2020 to August 2023. During this period, I spent three months at Nokia Standards, Oulu and another three months on a research visit to the University of Bologna, Italy. The writing and revision of the thesis were completed at VTT Technical Research Centre of Finland Ltd, Oulu. The research work was primarily funded by Research Council of Finland (former Academy of Finland) 6Genesis Flagship project and partially supported by Hexa-X, Business Finland 6G-SatMTC and Drolo projects. I am very thankful to Nokia foundation, Walter Ahlström foundation, Tauno Tönningin foundation, and Riitta and Jorma J. Takanen foundation for the awards and supporting this research activity.

I am extremely grateful to my supervisors, Associate Professor Konstantin Mikhaylov and Associate Professor Hirley Alves for their continuous support, weekly meetings, guidance, and encouragement throughout this research. Their expertise and mentorship have greatly supported this research journey, making it both progressive and interesting. I also want to thank Professor Mourad Oussalah, Dr. Harri Saarnisaari and Dr. Nurul Huda Mahmood for their insightful feedback provided during the follow-up group meetings. Their suggestions have been fruitful in refining the research questions. During my employment at CWC, I had the opportunity to work with both CWC - Networks and Systems (CWC-NS) and CWC - Radio Technologies (CWC-RT) units. I am thankful to the CWC leaders Professor Jari Iinatti and Professor Markku Juntti for the support during my time there. Additionally, I express my sincere gratitude to my thesis pre-examiners, Professor Mohamed-Slim Alouini and Professor Juan A. Fraire, for dedicating their valuable time to the review my thesis. I am sincerely thankful to Professor Mohamed-Slim for the very positive assessment of my thesis and for awarding it with distinction. I am also thankful to Professor Symeon Chatzinotas for serving as the opponent in my doctoral defence.

I extend my sincere appreciation to my collaborators for their extensive support and the opportunity to learn from their expertise and experiences. I am grateful to Associate Professor Gianni Pasolini for his continuous support and collaboration. I thank him sincerely for graciously hosting and warmly welcoming me at the University of Bologna. It was a great honor to visit the University of Bologna, the world's first and oldest university. My time there was great, filled with great experiences, for which I am deeply thankful. Thanks for showing me Villa Griffone - Museo Marconi. Visiting the workshop of Guglielmo Marconi (renowned as the father of wireless communications) and the

place where he conducted his initial radio telegraphy experiments was both inspiring and memorable. I am also thankful to Dr. Kaiqiang Lin and Professor Tong Hao from Tongji University, Shanghai, China for collaborative work and further extending the boundaries of this research. To Dr. Federico Clazzer and Dr. Andrea Munari from the DLR - German Aerospace Center, I would like to show my appreciation for the collaboration, I have learned a lot from you both.

I would also like to extend my gratitude to my current and former colleagues at VTT Technical Research Centre of Finland Ltd, Professor Marko Höyhtyä (currently with Finnish National Defence University), Dr. Antti Anttonen and soon-to-be Doctor Anastasia Yastrebova-Castillo for their collaboration and support. I have learned much from our discussions and technical meetings. I am happy that we all are making good contributions to satellite communication in the New Space era. Thanks to Mika Lasanen for the Finnish translation services and for the meaningful discussions.

I would also like to thank my other colleagues at VTT (in no particular order), Dr. Petri Mononen for warmly welcoming me to VTT. To Dr. Kari Heiska, I am thankful for discussions, guidance as well as for your confidence in my abilities. Additionally, I am thankful to Janne Takalo-Mattila, Antti Heikkinen, Mikko Uitto, Jussi Kiljander, Arttu Tamminen, Juha-Pekka Käräjäoja, Olli Apilo, Juha Lehtikangas, Tapio Rautio, and Jarno Pinola for the great time we spent together and enjoyable coffee breaks. Thanks to Timo Lind for his collaboration. With our joint efforts and experimental activities, I have learned the practical aspects of satellite communications. I look forward to practically integrating drones and satellite communications. I would also like to thank Vadim Kramar for inviting me to contribute to the ANTENNAE project. I look forward to expanding this research within the scope of ANTENNAE.

I also extend my gratitude to both current and former colleagues at CWC. A special thanks goes to my office mates, Associate Professor Onel Luis Alcaraz López and Dr. Mohammad Shehab (currently with King Abdullah University of Science and Technology, Saudi Arabia) for the good memories. I am thankful to Dr. Jean Michel de Souza Sant'Ana, Dr. Ehsan Moeen Taghavi, Dr. Marata Leatile, Irfan Muhammad, Fahad Qasmi, Binod Kharel, Osmel Rosabal, Dian E. Pérez, Nelson Mayedo, Eslam Eldeeb, Sabbir Ahmed, Muhammad Danyal Khattak, Champaka Damuddara Gedara and Haider Israr for the amazing time and positive experiences.

I would also like to express my appreciation to colleagues at Nokia. To Dr. Ilkka Känsälä, I appreciate the opportunity you provided to work with your outstanding team and get insights of the industrial research. I am also thankful to my other colleagues at Nokia including Muhammad Tayyab, Rapeepat Ratasuk, Nitin Mangalvedhe, and SunYoung Lee, for their contributions on my invention idea and making my time at

Nokia highly productive. Additionally, I am grateful to colleagues from the University of Bologna, including Dr. Amir Shehni (now at Humboldt University of Berlin), Dr. Anna Guerra and Dr. Francesco Guidi, for making my research visit memorable and enjoyable. I am also thankful to Professor Richard Demo Souza from the Federal University of Santa Catarina (UFSC), Brazil, Associate Professor Akram Al-Hourani from RMIT University, Melbourne, Australia and Dr. Jeroen Wigard from Nokia, Aalborg, Denmark for their collaboration and for supporting me to address the research challenges identified in this thesis.

I would like to offer my special appreciation to my friend Rana Inzimam Ul Haq for the great times and memories we shared in Oulu. I miss your company in Espoo. I am also grateful to my friends Assistant Professor Héctor Javier Pijeira Díaz and Ahsan Raza for their sincere friendship and constant support.

Most importantly, a very special thanks goes to my parents—my father Nabi and my mother Sabira—my brother Rehman, my brother-in-law Amir Bajwa, my sisters, and my nephews Ayan and Ali, as well as my nieces Esha and Irha. Thank you for the love, support, and understanding this challenging journey.

List of abbreviations

3GPP	*3rd Generation Partnership Project*
5G	*Fifth Generation of mobile networks*
6G	*Sixth Generation of mobile networks*
AIS	*Automatic Identification System*
BT	*Bandwidth time product*
CR	*Code rate*
CRC	*Cyclic redundancy check*
DL	*Downlink*
DR	*Data rate*
DtS	*Direct-to-Satellite*
FEC	*Forward error correction*
GEO	*Geostationary orbit*
GMSK	*Gaussian minimum-shift keying*
HPA	*High-power amplifier*
IoT	*Internet-of-Things*
ItS	*Indirect-to-Satellite*
IP	*Internet Protocol*
LDRO	*Low Data Rate Optimization*
LEO	*Low Earth orbit*
LoRa	*Long Range*
LoRaWAN	*Long Range Wide Area Network*
LPWAN	*Low Power Wide Area Network*
LPA	*Low-power amplifier*
LR-FHSS	*Long Range - Frequency-Hopping Spread Spectrum*
MAC	*Medium Access Control*
MEO	*Medium Earth orbit*
MTC	*Machine-Type Communications*
mMTC	*massive MTC*
NB-IoT	*Narrowband Internet-of-Things*
OBW	*Occupied bandwidth*
OCW	*Operating channel width*
PDR	*Packet delivery ratio*
PHY	*Physical layer*
RQ	*Research question*

SF	*Spreading factor*
SIoT	*Satellite Internet-of-Things*
SIR	*Signal-to-Interference Ratio*
SNR	*Signal-to-Noise Ratio*
TDMA	*Time Division Multiple Access*
ToA	*Time-on-Air*
UAV	*Unmanned Aerial Vehicles*
U-DtS	*Underground Direct-to-Satellite*
UL	*Uplink*

Symbols:

B	Transmission bandwidth
c	Speed of light
C	The number of OBW frequency channels
C_{Battery}	Battery capacity
D	Total seconds in a hour
G_r	Receiver antenna gain
G_t	Transmitter antenna gain
h	Channel coefficient
H	Orbital height
I_{fs}	Current consumption of LR1120 Frequency Synthesis state
I_{off}	Current consumption of LR1120 Radio off state
I_{pre}	Current consumption of LR1120 Radio preparation state
I_{sleep}	Current consumption of LR1120 Sleep state
I_{std}	Current consumption of LR1120 Standby state
I_{tx}	Current consumption of LR1120 Transmission state
I_{wu}	Current consumption of LR1120 Wake up state
K	Rician K-factor
M	LoRa modulation alphabet
N_F	Number of LR-FHSS payload fragments
N_H	Number of LR-FHSS header replicas
P_A	LR-FHSS average success probability
P_B	Total number of encoded payload bits in the LR-FHSS packet
P_{ALOHA}	LoRa probability of multi-frequency-channel unslotted Aloha
P_S	Success probability
P_{SIR}	Capture probability
P_{SNR}	Connection probability

P_{tx}	Transmit Power
R_b	LR-FHSS bit rate
R_p	Reporting period
T_b	LR-FHSS single bit duration
T_{c}	LoRa chirp duration
T_F	LR-FHSS single payload fragment duration
$T_{F_{last}}$	LR-FHSS last payload fragment duration
T_{fs}	Time duration of LR1120 Frequency Synthesis state
T_H	LR-FHSS single header fragment duration
T_{lifetime}	Battery life time
T_{LoRa}	LoRa total time on air
$T_{\mathrm{notification}}$	Notification period
T_{off}	Time duration of LR1120 Radio off state
$T_{preamble}$	LoRa preambles duration
$T_{payload}$	LoRa payload duration without preambles
T_{pre}	Time duration of LR1120 Radio preparation state
T_{sleep}	Time duration of LR1120 Sleep state
T_{std}	Time duration of LR1120 Standby state
T_T	State transition time
T_{tx}	Time duration of LR1120 Transmission state
T_{wu}	Time duration of LR1120 Wake up state
Δf	Frequency separation between LoRa chirps
Γ	Path loss
η	Path loss exponent
δ	Capture effect power threshold
σ	Shadowing coefficient
σ_w^2	Variance of the additive white Gaussian noise

Mathematical operators:

$\lvert\cdot\rvert$	*absolute value*
$\lceil\rceil$	*ceil operators*
$\exp(A)$	*exponential function of A*
$\mathbb{P}(A)$	*probability of event A's occurrence*

Contents

1 Introduction

The past years have delivered immense technological progress in fields related to the Internet-of-Things (IoT), with connectivity among the most illustrative examples. Massive machine-type communications (mMTC) offers cost-effective wireless connectivity for many IoT end devices with limited connectivity requirements [1, 2]. Taking another step, the concepts of non-terrestrial networks (NTN) and non-terrestrial mMTC have been proposed to enable global connectivity for expanding IoT operation in remote areas [3–8]. NTN is a key component of the upcoming 6G communications networks [9–12]. Industry and academia are thus focusing on mMTC and satellite integration to enable direct-to-satellite (DtS) global connectivity for IoT services [13–19]. Ubiquitous DtS connectivity promises to offer services for humans and machines, and it is equally beneficial for life at sea and on land and for humans in urban and remote areas. The products and services based on the DtS concept can help achieve the United Nations Sustainable Development Goals (SDGs), which benefit both animals and humans. Specifically, DtS applications in remote areas can support the maritime, mining industry, agriculture, renewable energy sector, wildlife, and asset monitoring and tracking applications [20, 21].

The satellite communication sector is growing at an impressive speed. The number of active satellites offering broadband and IoT connectivity is expected to grow from 10,000 to 100,000 by 2030. The satellite IoT global market will exceed six billion dollars by 2025 [22]. According to Rethink IoT (RIoT) research statistics, around 30.3 million satellite IoT devices will be deployed globally by 2025. Under the umbrella of potential non-3GPP technologies, LoRaWAN is one of the most important and widely used protocols for establishing long-range communications to support low data rate satellite IoT. This makes LoRaWAN, which is based on the LoRa and LR-FHSS physical layer patented by Semtech [7, 23], a prospective choice to enable satellite-based mMTC networks for low data rate use cases providing low-cost global coverage. To this end, flight-test experiments confirm the feasibility of DtS communications between LoRaWAN end devices and LEO satellites [24, 25]. As a milestone towards 3GPP satellite IoT, the International Maritime Satellite Organization (Inmarsat) and MediaTek have demonstrated successful trials between a ground Narrowband Internet-of-Things (NB-IoT) end device and a geostationary (GEO) satellite. Similarly, the satellite operator Eutelsat plans to use Sigfox for IoT connectivity.

1.1 Motivation

Wireless communication is the cardiovascular system of modern society. Despite its significant technical progress along the different tracks towards and beyond 5G, connectivity remains challenging in remote areas [1, 3–5, 26, 27]. Additionally, offshore environments lack wireless coverage where connectivity is crucial for supporting activities such as maritime operations, offshore wind farms, and oil rigs. Unfortunately, only 10% of the Earth's surface benefits from terrestrial communication networks due to geographical, economic, and practical limitations, creating a large digital divide. Remote areas generally have a poor or absent communications infrastructures, which hinders the provision of IoT services [28, 29]. Nearly 3 billion people and machines in remote areas still do not have access to the Internet today. SDG 10 aims at reducing inequality between people, and satellite technologies contribute to achieving this goal. [30].

In the last few years, mMTC and satellite integration have been investigated for global wireless coverage [31–33]. Current mMTC DtS trials have pinpointed several major technical constraints and challenges, which leaves an opportunity for further research. For example, LEO satellites require a high velocity to maintain orbit. Consequently, the relative velocity between the end device and satellite introduces a significant Doppler shift, resulting in time-frequency synchronization issues [24, 34–37]. Similarly, a satellite has a larger coverage footprint compared to a typical terrestrial gateway [38]. Therefore, the satellite gateway will have to handle myriads of uplink transmissions from terrestrial end devices, which raises many challenges, specifically, co-channel interference [39]. To support the exponentially growing DtS demand and massive transmissions, there is a need for energy-efficient radio access technologies (RATs) for very low-power, very low-cost, and compact end devices. Besides the Doppler and interference, the propagation of radio signals over long link distances of hundreds to thousands of kilometers presents another major challenge. Specifically, the obstruction in the radio path connecting end devices and satellites, commonly called Line-of-Sight (LOS) blockage, degrades communication performance due to shadowing. Moreover, end devices require a long battery life, ensuring uninterrupted DtS operation for years.

LoRaWAN modulations, specifically LoRa and LR-FHSS, known for their low-cost and low-power communication capabilities, have emerged as potential solutions for providing DtS connectivity for supporting IoT applications in remote areas [1, 13, 40]. The idea of mMTC LoRaWAN DtS is brand new, and much research work is needed to develop mature solutions. This thesis investigates the feasibility of LoRaWAN over the LEO satellite by developing simulation and analytical models, conducting performance analysis, and identifying key challenges for further studies.

1.2 Scope and objectives

Scope: This thesis evaluates the feasibility of mMTC and LEO satellite integration to enable wireless connectivity in remote areas. Specifically, the study focuses on evaluating the performance of LoRaWAN DtS communication, considering the satellite communications channel conditions such as strong Doppler effect, massive interference, and high propagation losses, as well as measurements to study the energy efficiency. Our results confirm the feasibility of direct communication from terrestrial end devices featuring LoRaWAN modulations—LoRa and LR-FHSS to LEO satellite. This thesis defines the operational boundaries of these modulations for DtS communications. Specifically, this thesis pinpoints several open challenges and promising research directions that can motivate further studies. The solutions discussed in this study could positively impact society and help achieve certain SDGs. For example, mMTC DtS communications based IoT solution contributes to *Goal 7: Affordable and clean energy* by monitoring and assisting the renewable energy generation systems in remote areas, e.g., offshore wind farms. It holds the potential to facilitate the maximization of industrial automation, thereby minimizing the dependence on human labor, an objective which aligns with *Goal 8: Decent work and economic growth*. DtS has the capacity to introduce innovative applications such as situational awareness, wildlife monitoring, and infrastructure surveillance, just to mention a few. These applications play a pivotal role in advancing *Goal 9: industry, innovation, and infrastructure*. DtS has potential for providing global connectivity and combating the digital divide, thus making a valuable contribution to *Goal 10: Reduced inequalities*. The DtS end devices are expected to be battery powered. This thesis conducts experiments to measure LR-FHSS air-time and current consumption characteristics. The proposed analytical models derived from these measurement results help to estimate the battery lifetime. Furthermore, these models can serve as valuable tools for optimizing network performance, thereby extending the battery lifetime by several years. This optimization aligns with the principles of *Goal 12: Responsible consumption and production*. Similarly, DtS communication protects terrestrial ecosystems and offers support to combat desertification contributing to *Goal 15: Life on land*. For example, DtS solutions can monitor forestry, specially the area outside the terrestrial coverage. In unforeseen disasters (earthquakes and floods), DtS can offer reliable connectivity when terrestrial networks are damaged. Finally, the research publications, measurement data, and openly accessible analytical and simulation tools developed within this thesis will serve as valuable resources for analyzing the performance of DtS IoT systems. These contributions are expected to benefit academic and industrial stakeholders significantly.

Objectives: The main focus of this thesis is a modeling and performance analysis of mMTC DtS connectivity to LEO satellites. To this end, the thesis discusses network architectures in **Chapter 3** and examines the performance of LoRaWAN modulations, namely LoRa and LR-FHSS, for challenging DtS scenarios. Specifically, we introduce a modeling framework and conduct a performance analysis for four critical aspects that influence DtS communications, including (i) the Doppler effect, (ii) radio propagation, (iii) massive co-channel interference, and (iv) end device energy consumption and battery lifetime. Specifically, **Chapter 4** accounts for the Doppler effect caused by satellite mobility and investigates the performance of LoRa and LR-FHSS, thereby identifying the limitations in LEO scenarios. Then, **Chapter 5** evaluates the LoRa and LR-FHSS DtS performance and assesses the feasibility of maintaining a sufficient link budget and scalability under strong interference. Our results include the probability of successfully receiving a radio packet transmitted by a terrestrial IoT device at the satellite-based gateway. The performance of LoRa and LR-FHSS schemes is compared for variable data traffic models. This comparison considers an illustrative use case scenario, specifically situational awareness for ships in the Arctic region. The network configuration applies real-life data traffic models and geospatial data for ship positions.

LR-FHSS is designed to meet the requirements of satellite IoT applications. Notably, LR-FHSS support only uplink communication from end-device to satellite, while the downlink can use LoRa modulation. The LR-FHSS end devices intended for satellite IoT are expected to operate on batteries like typical IoT devices. However, the existing literature lacks comprehensive models for LR-FHSS air time and energy characteristics. To bridge this gap, the thesis conducts extensive measurements and develops analytical models to characterize the air time and current consumption of LR-FHSS technology in **Chapter 6**. The primary research questions addressed in this thesis are as follows:

- **Q1:** What alternative network architectures and configuration options are there for integrating mMTC and LEO satellites to enable DtS communication for IoT applications?
- **Q2:** How can the impact of strong Doppler effects on LoRa and LR-FHSS uplink DtS performance in LEO be modeled and examined?
- **Q3:** How can we model and conduct the link-level analysis of the LoRa and LR-FHSS DtS communications?
- **Q4:** How can we effectively compare the scalability of LoRa and LR-FHSS DtS networks and determine which technology demonstrates better performance for massive connectivity scenarios?
- **Q5:** How can the LR-FHSS air time and current consumption characteristics be accurately measured and modeled?

Methods: This research employs analytical modeling, computer simulations, and empirical measurements. First, the thesis conducts a state-of-the-art review to answer Q1. MATLAB is used for development of analytical and simulation models script codes, as well as for their validation and performance analysis of DtS network. Specifically, we have developed new Monte Carlo simulator and analytical models to address these research questions. For developing simulator and analytical models, we consider a satellite directly passes over the end device, assuming the elevation angle between end device and satellite reaches 90°.

To answer Q2 and account for impact of Doppler effect, the Satellite Communications Toolbox is used to conduct the realistic orbital analysis and to calculate the Doppler shift and Doppler rate caused by an actual satellite. We developed analytical framework to investigate the impact of the Doppler effect on LoRa and LR-FHSS performance. Notably, Satellite Communications Toolbox was introduced during the thesis work in MATLAB R2021a. This toolbox allowed integration with our existing analytical and simulation models developed in MATLAB, facilitating a seamless workflow and efficient use of resources. MATLAB provides extensive guidelines, tutorials, webinars, and example codes for using the Satellite Communications Toolbox. The availability of these valuable resources was another motivation for selecting this toolbox.

To address Q3, this thesis develops an analytical model as well as Monte Carlo simulators. In Q4, a realistic data traffic model, end device densities, and ship geospatial dataset for end device positioning are used to accurately study and compare the scalability of LoRa and LR-FHSS.

During our experimental measurements, only the LR1120 model development kits were commercially available, which support LR-FHSS modulation. Therefore, for the experimental work and Q5, this thesis uses LR1120 development kits as a reference LR-FHSS transmitter. We used Agilent N6705B as the DC Power Analyzer to evaluate the energy consumption and air time characteristics of LR-FHSS modulation. The Nooelec RTL-Software Defined Radio (SDR) is used to observe and visualize the frequency spectrum of the LR-FHSS transmissions. To conclude, we have made these models' script codes openly accessible. These script code and relevant data are available on author's GitHub profile [1] to facilitate the reproduction of the results and further research on this topic.

[1] https://github.com/MuhammadAsadUllah1

1.3 Thesis contributions

This thesis comprises seven chapters; next, we briefly summarize author and each chapter's key contribution.

1.3.1 Author's contributions to the publications

This thesis is written as a monograph based on the following eight original publications: six journal papers including five published [41–45] and one submitted manuscript [46], one conference papers [47] and one book chapter [48]. The author of this thesis is mainly responsible for finding new ideas, developing simulations and analytical models which are openly accessible at author's GitHub [49–53], conducting experimental measurements, generating and analyzing the results, and writing the papers. The other co-authors collectively contributed their expertise and provided guidance for research directions and support in developing the simulation and analytical frameworks. During the manuscript writing and revision, the co-authors' meaningful feedback helped to enhance the overall quality.

Other contributions

Additionally, the author has made five contributions (patent, journals and conference papers) related to the scope of the thesis that are not included in this thesis. The author has contributed to three journal papers [54–56] and one conference papers [57]. These studies extend the scope of DtS communications to challenging scenarios, specifically considering buried mMTC end devices (as in underground wireless sensor networks [58]). This novel form of connectivity is called underground DtS (U-DtS), and these works investigate the influence of the burial depth, soil moisture, and water content in the soil on DtS connectivity performance while illustrating real-world use cases, e.g., smart agriculture and pipeline monitoring. In addition to these publications, the author has also collaborated on a filed patent application [59] that enables device-to-device connectivity for 3GPP-standardized IoT devices.

1.4 Thesis summary and outline

1.4.1 Summary

First, **Chapter 2** presents an overview of the satellite communications system, including the network components, satellite orbits, form factors, and payloads. Second, it briefly discusses the existing systems and potential RATs for satellite communications. This thesis opted for LoRaWAN: LoRa and LR-FHSS modulations. Notably, the LR-FHSS is a brand-new technology introduced during this thesis work. Third, a state-of-the-art literature review was conducted to identify the research gap and understand recent developments.

Next, **Chapter 3** discusses two possible communication architectures and points out relevant practical constraints and trade-offs associated with these implementation strategies. In a direct-to-satellite setup, end devices communicate directly with a satellite. Meanwhile, in an indirect-to-satellite architecture, end devices send data to a ground network, which forwards the information to the satellite. This thesis focuses on the most challenging architecture – the direct-to-satellite. **Chapter 3** also introduces the system models used to develop analytical and Monte Carlo simulation tools for investigating the DtS performance in the next chapters.

Moving forward, **Chapter 4** discusses and thoroughly investigates the impact of the Doppler effect on the performance of LoRa and LR-FHSS in satellite links. The analysis accounts for the effects of key communications parameters and settings, such as bandwidths, carrier frequency, and LoRaWAN Low Data Rate Optimization (LDRO). The results identify the LoRa and LR-FHSS boundaries for successful operation in the LEO scenario. The achieved results can facilitate the selection of suitable parameters for future system designs.

Chapter 5 extends the analysis and conducts a link-level study of DtS connectivity. To obtain a more in-depth insight into the feasibility, this thesis considers a propagation model that accounts for the path loss attenuation (based on the Friis model) and the Rician fading (whose LOS component affects the elevation angle). For a scalability analysis, the model accounts for the co-channel interference due to the transmission of the other LoRaWAN end devices. In this thesis, the simulations-based interference model considers the capture effect, which allows the satellite to receive the strongest signal. The results conclude that DtS communication is feasible and a signal from a terrestrial end device could reach the satellite at a distance of hundreds to thousands of kilometers. However, the success probability decreases due to simultaneous transmissions from other end devices causing same-channel interference. This chapter analytically compares the LoRa and LR-FHSS scalability for an illustrative use case scenario—situational awareness for ships. Our results confirm that LR-FHSS offers a better capability than LoRa modulation.

The LoRaWAN LR-FHSS end devices envisioned for DtS IoT will be primarily battery-powered and perform better than LoRa. Therefore, it is crucial to investigate the current consumption characteristics of LR-FHSS technology. However, to our knowledge, no prior research has presented accurate ToA and current consumption models for this newly introduced scheme. **Chapter 6** addresses this shortcoming through extensive measurements and the development of analytical models. Finally, **Chapter 7** concludes the lessons learned from this thesis and highlights potential future research directions.

1.4.2 Outline

The rest of this thesis is organized as follows. Chapter 2 presents the background of satellite communication systems and the potential radio access technologies for satellite IoT services, while alternative network architectures and a system model for performance evaluation are discussed in Chapter 3. Then, the key results derived from the proposed framework accounting for the impact of the Doppler effect on LoRa and LR-FHSS DtS performance are analyzed in Chapter 4. Next, Chapter 5 uses the developed analytical and simulation tools to evaluate the DtS link-level performance considering the link budget and interference for LoRa and LR-FHSS scheme and compares the scalability of these two schemes. LR-FHSS experiment-based accurate air-time and current consumption analytical models are proposed in Chapter 6. Finally, Chapter 7 concludes this thesis with final remarks and future research directions.

2 Satellite IoT communications: technical background

This chapter summarizes the work reported in [47, 48] and discusses satellite communication systems, including network components, payload, and orbits. It also highlights why LEO satellites are suitable options for IoT services. The discussion focuses on major existing proprietary satellite systems and potential 3GPP and non-3GPP Low Power Wide Area Network (LPWAN) RATs for global satellite IoT. In the current 5G 3GPP NTN specifications, Narrowband Internet of things (NB-IoT) is primary candidate for satellite IoT services. In the non-3GPP umbrella, LoRaWAN modulations LoRa and LR-FHSS are among the prominent candidates and offer long-range and energy-efficient communication that closely aligns with the satellite IoT requirements. Both LoRa and NB-IoT are widely accepted terrestrial solutions for low data rate applications. These two technologies benefit from the mass and low-cost production of end devices, gateways, and other network infrastructure components, resulting in cost-effective solutions. Real-world experiments have confirmed the feasibility of using these technologies for satellite IoT applications. Unlike NB-IoT, the LoRaWAN works on unlicensed spectrum and its integration with LEO satellite aims to lower satellite connectivity costs for low data rate IoT applications while efficiently supporting many users. Recent flight test experiments conducted by universities and industries confirm the feasibility of LoRa signal reception by/from LEO satellites. Despite the feasibility of LoRa DtS communications, there remains a need for further research on this emerging topic. Specifically, most of these trials do not closely follow the requirements of the LoRaWAN protocol. Similarly, the technical details and timeline for LoRaWAN satellite IoT commercial services are scarce because technology is in the developmental stages. To lay the foundation for analysis in the forthcoming chapters, this chapter presents a comprehensive technological background to LoRaWAN modulations, namely LoRa and LR-FHSS. A thorough state-of-the-art review is conducted on LoRaWAN DtS IoT systems to identify the research gap and open challenges. The literature review considers real flight-test experiments, the Doppler effect, link budget assessments, network scalability, energy efficiency aspects.

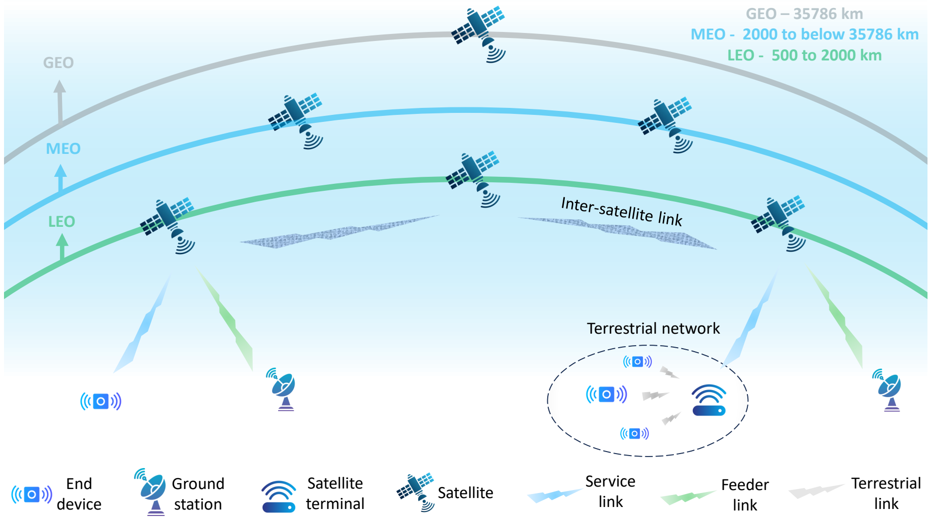

Fig. 1. The key components of a satellite communication system.

2.1 Satellite communications system

2.1.1 Network components

The network components of a satellite communications system include:

End device, user, and satellite terminals

In the terrestrial segment, the end device[2], often known as the user terminal (UT), is the key network component to transmit and receive data from the satellite, as illustrated in Fig. 1. The end devices envisioned for MTC DtS should support long-range transmission and be compact, affordable, and energy-efficient. For example, LoRaWAN Class A end devices are compact and battery-powered and use power-saving schemes to spend inactive time in deep sleep mode to avoid unnecessary power consumption and increase the battery lifetime [7]. On the contrary, the conventional STs such as Starlink are bigger and require a continuous power supply from an external power source.

[2]The thesis uses the terms user terminal (UT), satellite terminal (ST), user equipment (UE), and end device interchangeably.

Satellite

Communications satellites are Earth-orbiting wireless transceivers. The satellite launch costs highly depend on the orbital height and payload. Every single gram of payload that we put into space contributes to overall launch costs. Therefore, the space industry prefers small satellites, often called *Nanosatellites*, which has low weight for DtS IoT applications. *Nanosatellite*, as the name suggests, is a compact satellite with a weight of less than 10 kilograms [60]. It offers several benefits in terms of cost and development timelines compared to conventional satellites. *Nanosatellites* can be designed, built, and launched at a relatively lower cost, making them a more economically viable option for satellite IoT. The term *Cubesats* defines the design dimension of the satellite. In *Cubesats*, the term *U* such as $1U$, $2U$, $3U$, or $6U$ refers to a standard design dimension unit, where $1U$ is equivalent to $10 \times 10 \times 10$ cm cube. *Cubesats* can also be developed in larger sizes, e.g., $3U$ by integrating multiple cubes. Typically, *Cubesats* are designed to be launched into LEO, where communication undergoes a strong Doppler effect [61].

Gateway

A gateway is a radio transceiver responsible for receiving packets from the end devices and forwarding them to a server for further processing. It can be installed in terrestrial or non-terrestrial segments of the network depending on the implementation architectures [13].

- **A terrestrial gateway:** can be installed on the ground, receiving and transmitting the data from/to end devices on the ground. On receiving data from the end devices, the terrestrial gateway backhauls the data to a satellite using a service link.
- **A non-terrestrial gateway:** is a transceiver on a satellite that bridges the massive number of end devices and the ground stations. It directly receives data packets from end devices and forwards them to the ground stations, which are further connected to network and application servers.

To ensure DtS communications reliability, the gateway should be capable of supporting massive uplink transmissions simultaneously. To give one practical example, a single LoRaWAN LR-FHSS gateway designed for satellite connectivity can handle up to 11 million packets daily in the Federal Communications Commission (FCC) region [62, 63].

Ground station

Similar to user terminals, ground stations are the radio transceivers deployed on the Earth to communicate with satellites [64]. Unlike UT–end devices, the ground stations can control satellites, monitor the telemetry data, and configure the satellite onboard radio.

Communication links

The radio link between the end device and satellite is called the service link, as shown in Fig. 1. The satellite and ground station communication link is known as the feeder link [8, 60]. To enable global coverage a constellation is required that comprises multiple satellites. The communications link between satellites is called an inter-satellite link (ISL).

2.1.2 Payload

The satellite payloads typically belong to one of two categories (i) transparent which act as relay or (ii) regenerative with has advanced on broad processing capabilities [7,65–67]. The terms transparent and regenerative come from 3GPP. These architectural concepts can also be applied to non-3GPP technologies, with LoRaWAN serving as an example.

Transparent

Traditional satellite systems feature a transparent payload often known as bent pipe architecture, which acts as analog radio frequency repeaters. The onboard satellite transceiver filters, amplifies, and relays the received signals to the ground station without demodulating and decoding them. A satellite system featuring a transparent payload has low implementation complexity because it does not require additional onboard processing capabilities. On the downside, the lack of resources and functionalities in transparent payloads contributes to the lower spectral efficiency of the feeder link [65].

Regenerative

On the contrary, a satellite with a regenerative payload featuring an onboard processing unit recreates the received signals. Specifically, a regenerative payload demodulates, decodes, and performs error correction. Before forwarding the signal back to the target location on Earth, the non-terrestrial gateway on the satellite re-encodes and re-modulates the signal [65–67], which contributes to the improvement of feeder link spectral efficiency.

2.1.3 Orbits

Satellite communications systems are conventionally subdivided into three main groups: Low Earth orbit (LEO, 550-2,000 km), Medium Earth Orbit (MEO, between 2,000 and below 35,786 km), and Geosynchronous Earth Orbit (GEO at 35,786 km) [64]. With over 7,560 active satellites, the Earth's orbit is dominated by 6,768 LEO satellites as of March, 2024. Most of these satellites are orbiting at an altitude of 550-800 km [64]. The satellites in all three of these orbits are capable of providing DtS connectivity. However, each orbit possesses its own set of advantages, disadvantages, and associated trade-offs. The space industry is opting for LEO satellites to enable global MTC coverage due to the following major reasons [8].

– First, LEO satellites experience the lowest propagation losses due to the benefit of being close to the Earth.
– Second, the propagation delay of a radio signal from the Earth's surface to an LEO satellite is much lower than GEO satellites. For example, the expected propagation delay will be around 116 ms for the GEO satellites located at higher altitudes. The propagation delay is below 10 ms for the LEO satellites with an orbital height of 780 km.
– Third, the launch costs highly depend on the orbital height, satellite payload, and launch vehicle. Therefore, LEO satellites have the lowest launch costs, and the space industry prefers this orbit for IoT applications [60].
– Fourth, initial trials show the feasibility of the DtS connectivity between the mMTC end devices and LEO satellites using a reasonably low transmit power.

This thesis opted for LEO to investigate mMTC and LEO satellite integration for these reasons. However, there are also several challenges that LEO introduces. The two major ones are the dynamic channel conditions due to the satellite's mobility and the limited lifetime of a satellite in orbit.

A two-line element set (TLE) is an orbital data format used for encoding satellite information. TLE allows to estimate a satellite's position in orbit at any point in the past, present, or future with a certain degree of accuracy, depending on the used perturbation models. This thesis uses TLE data to account for satellite mobility and examines the impact of the Doppler effect on communication performance.

2.2 Satellite technologies landscape

In the landscape of satellite IoT applications, Argos stands out as one of the earliest systems. It is served by seven polar-orbiting satellites at an altitude of 850 km, which collect environmental data globally. Similarly, the Automatic Identification System (AIS) and Automatic Dependent Surveillance–Broadcast (ADS-B) are widely adopted protocols for ship and aviation surveillance, respectively.While both AIS and ADS-B can function independently of satellites, their performance is significantly enhanced with satellite availability. This chapter primarily discusses the general purpose radio access technologies. However, in Chapter 5, we delve into the discussion and evaluation of the performance of satellite-based AIS systems.

Driven by global digitization, mMTC technologies answer the need to provide massive ubiquitous wireless connectivity under very low energy consumption. 3GPP and non-3GPP LPWANs represent a group of technologies within the mMTC, which offer long-range, massive connectivity and scalability, subject to low energy consumption.

This section discusses existing satellite systems and several potential RATs, including the LPWAN technologies both within and outside 3GPP standardization, which may be potential for satellite IoT connectivity. For example, NB-IoT is 3GPP technology, serving both terrestrial and non-terrestrial networks. On contrary, LoRa and LR-FHSS are non-3GPP technologies. Initially, LoRa was developed for terrestrial IoT applications, now this technology is under investigation for its potential use for satellite IoT connectivity. On the other hand, LR-FHSS is an emerging technology specifically designed to support both terrestrial and non-terrestrial IoT requirements. Table 1 shows some satellite systems' key technologies, applications, and operational statuses.

Table 1. The list of the reviewed satellite technologies, including existing and potential.

Company	Technology	3GPP	LPWAN	Licensed	Operational status	Services
Starlink	Proprietary	✗	✗	✓	✓	Broadband
Iridium	Proprietary	✗	✗	✓	✓	Broadband, IoT
OQ Technology	NB-IoT	✓	✓	✓	✓	IoT
AST Space Mobile	5G NR	✓	✗	✓	Trials	Broadband
Lacuna Space	LoRa, LR-FHSS	✗	✓	✗	Trials	IoT
Fossa Systems	LoRa	✗	✓	✗	Trials	IoT
Wyld Networks	LoRa	✗	✓	✗	✓	IoT
	NB-IoT	✓	✓	✓	Planned	IoT
N/A	5G RedCap	✓	✓	✓	Being discussed	Mid-range IoT
Kinéis	LoRa	✗	✓	✓	Planned	IoT
EchoStar	LoRa	✗	✓	✗	Planned	IoT
	NB-IoT	✓	✓	✓	Planned	IoT
	Proprietary	✗	✗	✓	✓	Broadband
Satelliot	NB-IoT	✓	✓	✓	✓	IoT
Myriota	NB-IoT	✓	✓	✓	✓	IoT

2.2.1 Proprietary

Starlink

The Starlink constellation comprises over 6,000 LEO satellites, employing proprietary technology to deliver Internet across the Ku and Ka bands, specifically within the frequency ranges of 12-18 GHz and 26.5–40 GHz, respectively [68]. To establish a connection with the satellite, a Starlink ground terminal and a service plan are required [64, 69]. Presently, four ground terminal options are available as follows: (i) standard, (ii) standard actuated, (iii) high performance, and (iv) flat high-performance terminals. Starlink offers standard and mobile (roaming) service plans with prioritization options. The flat high-performance terminal promises to provide a downlink speed ranging from 40 to 220+ Megabits per second (Mbps) and a uplink between 8 and 25+ Mbps, with a latency of less than 99 milliseconds. Anticipating further advancements, the next generation of Starlink satellites will comply with 3GPP specifications.

Iridium

Iridium, whose constellation consists of 6 polar orbits, 11 satellites in each, with an 86.4^{o} orbital inclination at 780 km altitude, covers the entire Earth [69]. A specific location on the surface is served by a satellite for about nine minutes (as long as the elevation angle stays above 8.2 degrees, often rounded to 10 degrees). Iridium offers two-way satellite communications using the 1616 to 1626.5 MHz frequency band [64]. It features Time Domain Duplex (TDD) duplexing and Time Division Multiple Access (TDMA)/Frequency division multiple access (FDMA) multiplexing methods. Iridium Certus 9770 device provides up to 22 kilobits per second (kbps) and 88 kbps for uplink and downlink, respectively.

2.2.2 3GPP

Narrowband-IoT

The NB-IoT is an LPWAN radio technology developed by 3GPP to operate in licensed frequency bands. It is designed to meet the needs of mMTC and has already been commercially deployed globally [70]. Based primarily on orthogonal frequency-division multiplexing (OFDM) for downlink and single-carrier frequency-division multiple access (SC-FDMA) for uplink communications, NB-IoT employs significantly simplified LTE-based procedures for accessing the radio channel and transferring the data. As a milestone, MediaTek and Inmarsat's collaborative work reported successful experimental testing of a connection between a ground NB-IoT end device and a GEO satellite orbiting 35,786 kilometers above the Earth's surface. Sateliot and MediaTek contribute to NTN aspects of Release 17 of the 3GPP standardization. OQ technology company is compatible with 3GPP standards to provides satellite NB-IoT services with data rates of 30 kbps – 60 kbps [8].

5G new radio

5G new radio (NR) supports enhanced mobile broadband (eMBB), ultra-reliable and low latency communication (URLLC), and mMTC use cases. Several possible frequency band options are discussed within 3GPP specifications to support 5G NR NTN and satellite connectivity. 5G NR NTN spectrum includes the L-band, S-band, and Ka-band frequencies and uses frequency-division duplexing (FDD). The NTN band n255 (L-band) and n256 (S-band) are introduced in 3GPP Rel.18 TS 38.101-5 [71], and recently, n254 was introduced in Rel. 18 TR 38.741 [72] which uses the L-band for uplink and S-band for downlink. These bands are well-researched and proven to support legacy satellite communications systems. For example, Iridium uses the L-band frequency ranging from 1616 to 1626.5 MHz. Initial trials from AST SpaceMobile and Lynk Global have demonstrated the feasibility of 5G NR in LEO satellite links [73]. On September 8, 2023, the first 5G satellite call was successfully demonstrated using AST SpaceMobile's prototype satellite BlueWalker 3. This satellite is designed to operate directly with standard, unmodified mobile devices for broadband connectivity. Similarly, Lynk Global has three operational 5G compatible satellites which also confirmed the feasibility of messaging and low data rate connectivity services [64].

The 5G NTN ecosystem includes both NR for broadband services and NB-IoT for IoT services over satellite. In 3GPP Release 17, Reduced Capability (RedCap) technology is introduced to 5G NR ecosystem for terrestrial IoT. It is expected that the 3GPP Rel-19 will incorporate RedCap NTN support.

5G reduced capability

Reduced Capability (RedCap) was introduced in 3GPP Rel. 17, aiming at use cases between eMBB, URLLC, and mMTC. The RedCap features the functionalities between the NB-IoT, Sigfox, LoRaWAN, and 5G NR UE [74, 75].

- **3GPP release 17 RedCap:** 3GPP TR 38.875 [74] discusses the support of RedCap NR UEs. Introducing RedCap UEs aims to support mid-range IoT applications and reduce UE cost and complexity compared to legacy 5G NR UE. Rel. 17 specifies, among other objectives, the complexity reduction, such as UE power saving and battery life enhancement. The Rel. 15 legacy 5G NR UE operates on the 100 MHz bandwidth of the FR1 range. Rel. 17 RedCap reduces the bandwidth to 20 MHz for FR1 to achieve complexity reduction. For example, Rel. 17 RedCap UE peak bit rate requirements for wearable use cases can be up to 150 Mbps in downlink and 50 Mbps in uplink.

– **3GPP release 18 RedCap:** For operations in FR1, the RedCap bandwidth is further reduced to 5 MHz. Following this, the data rates is scaled by a 0.25 factor compared to Rel. 17 RedCap UEs. According to TR 38.865, [75], the Rel. 18 RedCap UEs aim to achieve a peak data rate of 10 Mbps.

2.2.3 Non-3GPP: LPWAN

In the non-3GPP LPWAN family, LoRaWAN and Sigfox dominate the market.

Sigfox

The Sigfox works on industrial, scientific, and medical (ISM) and Short Range Devices (SRD) bands globally from 862 to 928 MHz. Specifically, operations in Europe, the Middle East, Africa, and India (EMEAI) use the 862-876 MHz frequency range. Conversely, regions including the Americas, Asia-Pacific (APAC), and APAC 2 (including Japan and South Korea) use the 902-928 MHz band. Sigfox uses an ultra-narrowband signal with a differential binary phase shift keying (DBPSK) modulation scheme in uplink and a Gaussian frequency shift keying (GFSK) modulation scheme in downlink. Bandwidth in uplink is 100 Hz, whereas it is 1.5 kHz in downlink, offering a data rate of 100 bps with 12 bytes of maximum payload in UL and a data rate of 600 bps with 8 bytes of maximum payload in downlink. Eutelsat satellite operation company plans to launch LEO nanosatellites, which are expected to be integrated with the Sigfox terrestrial connectivity services for various sectors, e.g., transport, oil and gas, and agriculture.

LoRaWAN

LoRaWAN is one of the most important and widely used protocols for establishing energy-efficient, low-cost, and long-range communications [76–79]. This makes LoRaWAN a prospective choice to enable global connectivity for satellite IoT. Both industry and academia have launched several LoRa satellites into LEO orbit, which has confirmed the feasibility of LoRa DtS connectivity and highlighted the open challenges and interesting directions for further research [24, 80]. To align with recent academic and industrial developments [13–19, 34–37, 80, 81], this work opted LoRaWAN technologies LoRa and LR-FHSS for extensively investigating the mMTC and LEO satellite integration. Specifically, the reasons for choosing LoRaWAN are as follows:

- Unlike 3GPP LPWAN, LoRaWAN operates on a license-free spectrum, making LoRa and LR-FHSS prominent for low-cost low data rate satellite connectivity.
- LoRaWAN is emerging as one of the key technologies for global satellite IoT services. Unlike any other mMTC LPWAN technology, more than 20 active LEO satellites feature LoRa modulation. These satellites include Lacuna Space, Norby, FOSSA, FEES, and SATLLA-2B. These satellites transmit LoRa packets, and as of March 2024, thousands of ground gateways have successfully received over eight million LoRa packets [25].
- Only LoRaWAN gateways are readily commercially available, allowing deployment of so-called "private" networks, which are managed not by dedicated telecommunication service providers. A private person or a company can easily get LoRaWAN gateways from the market to deploy a private network, which is not true for Sigfox and NB-IoT.
- LR-FHSS has recently been introduced into the LoRaWAN protocol specification for terrestrial and non-terrestrial networks, notably satellite IoT. Additional studies are required to assess the technology's capabilities. This motivates the current thesis to develop simulation and analytical models and conduct measurements to investigate the potential of LR-FHSS for DtS communications.

It is worth to remind that LR-FHSS only support uplink, where LoRa support both uplink and downlink communications.

2.3 LoRaWAN technology

This section provides the technical background for LoRa and LR-FHSS modulations, serving as the basis for modeling and performance analysis in the forthcoming chapters.

2.3.1 LoRa

Physical layer

LoRa is a derivative of the Chirp Spread Spectrum (CSS) modulation. As is well known, a sine-wave chirp signal, concisely denoted chirp in the following, consists of a sinusoid whose frequency linearly sweeps within a given interval of bandwidth B [40]. LoRa's key features are

- $\mathrm{SF} \in \{7,8,9,10,11,12\}$, known as the spreading factor,
- $B \in \{31.25, 62.5, 125, 250, 500\}$ kHz, the bandwidth,
- $M = 2^{\mathrm{SF}}$, the cardinality of the modulation alphabet, and
- T_c the chirp duration, chosen such that $BT_\mathrm{c} = M$.

The SF is one of the key elements of the network configurations. The different SFs are quasi-orthogonal, which allows the simultaneous reception of the signals with different SFs if their power difference does not exceed a particular power threshold. The higher SFs improve the gateway's ability to demodulate a radio packet correctly in the presence of noise. It is observed that, for a given SF, the LoRa transmitter has at its disposal a set of $M = 2^{\mathrm{SF}}$ different chirps, each of which is in a one-to-one correspondence with one of the M symbols of the modulation alphabet $\mathscr{S} = \{0, 1, 2, \cdots, M-1\}$. Given the adopted SF, it follows that for each sequence of SF data bits to be transmitted, the modulator selects the corresponding modulation symbol within $\mathscr{S}$ and transmits the chirp with which that symbol is uniquely associated. It is worth emphasizing that the M chirps are different in that they start sweeping from different initial frequencies, which are regularly spaced with a frequency step $\Delta f = \frac{B}{M}$ Hz [23]. This means a larger SF, which corresponds to lower values of Δf, which are more sensitive to the Doppler effect because of the frequency separation between chirps.

Low data rate optimization (LDRO)

To increase the robustness to Doppler, LoRa features the LDRO mode, which reduces the number of bits carried by each symbol by two. This means that, for a given SF, the cardinality of the modulation alphabet reduces to $M = 2^{(\mathrm{SF}-2)}$, as does the number of chirps packed in the bandwidth B, which entails that the LDRO mode increases the frequency separation Δf between chirps by four times, and therefore the resistance to Doppler. This positive result comes at the cost of reducing the data rate [45, 80, 82, 83].

Frame structure

An LoRa packet has three key components that include preambles, a header (optional), and the data payload. The header is only available in explicit mode to carry the information on payload length, configured code rate, and cyclic redundancy check (CRC). The preamble helps to synchronize the receiver with the transmitter. By default, the

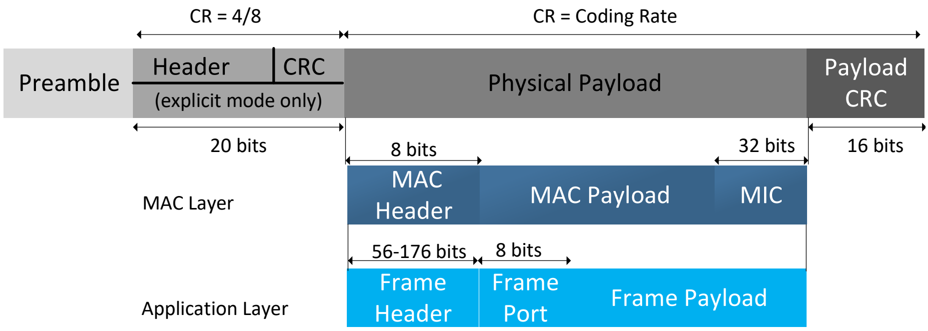

Fig. 2. The key components of the LoRa packet structure.

preamble consists of 12-symbol-long sequences; however, the preamble length is configurable between 6+4 and 65535+4 symbols. A typical physical layer LoRa packet carries 13 bytes as an overhead from the MAC and application layer. Fig. 2 shows the key components of the LoRa packet.

Time-on-Air model

The total time-on-air of a LoRa packet comprises both the duration of its preamble ($T_{preamble}$) and that of the transmitted packet payload ($T_{payload}$) itself as

$$T_{LoRa} = T_{preamble} + T_{payload}. \tag{1}$$

where $T_{payload}$ also accounts for the header. Notably, LoRa ToA highly depends on the SF; an increase in SFs almost doubles the on-air time for sending the same payload, thus increasing the probability of collisions.

2.3.2 LR-FHSS

Physical layer

The new LoRaWAN Data Rates (DRs 5-6 for the United States (US) and DRs 8-11 for the European Union (EU) region) feature LR-FHSS modulation [84, 85] for uplink i.e., end device to satellite link. LR-FHSS is based on Gaussian minimum-shift keying (GMSK) modulation, which uses bandwidth time (BT) products to define the pulse shapes. Currently, it features BT = 1; however, the other values of BT are reserved for future use [86]. BT = 1 offers an instantaneous bit rate $R_b = 488.28125$ bits per

Table 2. Comparison of LoRa and LR-FHSS key features.

Parameters	LoRa	LR-FHSS
Modulation	CSS	GMSK
Code rate	$\frac{4}{5} \cdots \frac{4}{8}$	$\frac{1}{3}, \frac{1}{2}, \frac{2}{3}, \frac{5}{6}$
Daily Maximum Capacity [1]	1.2M uplinks/GW	11M uplinks/GW
Frequency Drift Tolerance	120 Hz/s	300 Hz/s
Uplink	✓	✓
Downlink	✓	✕
Spreading factors	✓	✕
Header Diversity	✕	✓
Intra-packet hopping	✕	✓

[1] Capacity in million (M) uplink packets per day per gateway for a 1.5 MHz channel bandwidth i.e., operating channel width (OCW) [87].

second (bps) [87], including useful data as well as overhead, e.g., the preamble, coding redundancy, and CRC bits. Each coded bit (i.e., after forward error correction (FEC) has a duration of approximately $T_b = \frac{1}{R_b} = 2$ ms, as explained in [88]. To enhance the network capacity and minimize collisions, LR-FHSS uses intra-packet frequency hopping. Besides the improved capacity, LR-FHSS offers better robustness to the Doppler effect than LoRa [87]. With an occupied bandwidth (OBW) channel of 488 Hz, LR-FHSS offers a comparable link budget to LoRa DR0 (SF12) operating at a 125 kHz bandwidth while delivering 200 times greater capacity. Table 2 compares the key characteristics of LR-FHSS and LoRa.

LR-FHSS uses convolution encoding to carry out forward error detection and correction. Specifically, the header uses a fixed CR=$\frac{1}{2}$ while payload data fragments can use four code rate options CR=$[\frac{5}{6}, \frac{2}{3}, \frac{1}{2}, \frac{1}{3}]$. However, current LoRaWAN specifications only support two CRs $\frac{1}{3}$ and $\frac{2}{3}$ reserving the remaining two for future use, as mentioned in the LR1120 user manual [86]. Specifically, in the European Telecommunications Standards Institute (ETSI) region, DR8/DR10 and DR9/DR11 apply coding with the CR equivalent to $\frac{1}{3}$ and $\frac{2}{3}$, respectively. Similarly, in FCC operational areas, DR5 and DR6 use coding with the CR equivalent to $\frac{1}{3}$ and $\frac{2}{3}$, respectively. Notably, the lower CR improves the gateway's ability to correctly demodulate the packet in the presence of noise and interference.

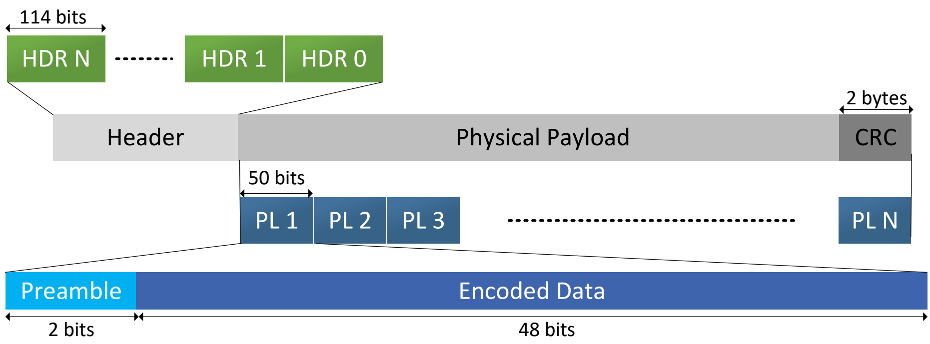

Fig. 3. The key components of the LR-FHSS packet structure, where HDR and PL denote header and payload fragments, respectively.

Frame structure

Fig. 3 illustrates the LR-FHSS frame structure. LR-FHSS divides the payload into small fragments and transmits over multiple OBW channels following the frequency hopping sequence picked by a pseudo-random number generator. The packet header contains essential information to notify the gateway about the frequencies and hopping sequence of the payload fragments [81]. Unlike LoRa, the LR-FHSS device transmits several replicas of headers ($N_H = 1 \ldots 4$), where the DR setting defines the number of replicas. A gateway should receive at least one of the N_H transmitted headers to decode a packet successfully. However, header diversity improves immunity against co-channel interference, which costs longer ToA. In the LoRaWAN protocol, DR5 (in the FCC region) and DR8/DR10 (in the ETSI region) specify $N_H = 3$, while DR6 (FCC) and DR9/DR11 (ETSI) feature $N_H = 2$ [89].

Each encoded header comprises $H_b = 114$ bits resulting in a header duration as $T_H = \frac{H_b}{R_b} = 233.472$ ms. In contrast, each encoded payload (payload plus CRC) fragment has $F_b = 50$ bits containing 48 payload bits and 2 bits preamble in each hop [86, 88, 90]. Therefore, each payload fragment is $T_F = \frac{F_b}{R_b} = 102.4$ ms long. However, the last payload fragment can be shorter. The FCC regulations impose a 400 ms dwell time limitation, which LR-FHSS comfortably adheres to. By employing intra-packet frequency hopping, the LR-FHSS header and fragments effectively comply with the packet dwell time restrictions [87].

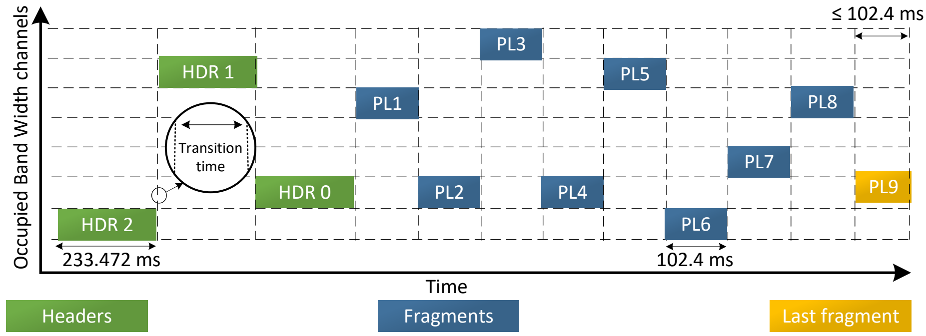

Fig. 4. Illustrative frequency hopping profile of a single LR-FHSS packet of payload $L = 15$ bytes and DR8 featuring CR =$\frac{1}{3}$ and $N_H = 3$

Channels and frequency hopping

LR-FHSS provides a range of configuration options for channel bandwidths, hopping grid size, and minimum frequency separation. The whole frequency band is divided into multiple operating channel width (OCW) channels, allowing the cumulative bandwidth to span from 39.06 kHz to 1.5742 MHz, depending on the local frequency regulations [87]. For frequency hopping, a single LR-FHSS OCW channel is further divided into multiple subchannels with a bandwidth of 488 Hz, named OBW channels. At any moment, a single end device can transmit its data (header or fragment) only on one OBW channel, also known as a hop. Note that multiple OBW channels are required to transmit the full LR-FHSS packet. Fig. 4 depicts the transmission of a 15 byte payload applying CR $= \frac{1}{3}$, and header replica $N_H = 3$, resulting in a number of payload fragments $N_F = 9$.

Time-on-Air models

The existing LR-FHSS ToA models are based primarily on the LoRaWAN regional specification document [62].

– **Model I:** Departing from the information in [85], the ToA of an LR-FHSS packet for physical payload of L bytes is expressed as

$$T_{model\_I} = \begin{cases} N_H T_H + T_F \left\lceil \frac{L+3}{2} \right\rceil & \text{for DR8/DR10} \\ N_H T_H + T_F \left\lceil \frac{L+3}{4} \right\rceil & \text{for DR9/DR11} \end{cases}. \tag{2}$$

This model assumes all the payload fragments have the same duration.

– **Model II:** Unlike the previous model, the work in [88, 90] accounts for the fact that the last fragment could be shorter than standard $T_H = 102.4$ ms. Following this model,

Table 3. Launched LEO DtS IoT systems [25, 47].

Satellite	CubeSat	Quantity	RAT	Frequency	Purpose
Norby	6U	1	LoRa	436.7 MHz	Research
FOSSA Systems	2P*	13	LoRa	401.7 MHz	Sat-IoT
Lacuna Space	3U	5	LoRa	868, 915 MHz	Sat-IoT
SATLLA-2B	2P	1	LoRa	437.2 MHz	Research
FEES	0.3U	2	LoRa	437.2 MHz	Experimental

* PocketQube

the ToA can be calculated as

$$T_{model\_II} = N_H T_H + \left(\frac{L + P_{\mathrm{CRC}}}{6\mathrm{CR}}\right) T_F, \tag{3}$$

where P_{CRC} =2 bytes accounts for the CRC. Since we know each hop can accommodate 48 bits (6 bytes), therefore (3) is divided by 6 to calculate the total number of fragments of 48 bits.

2.4 State-of-the-art review and open challenges

The thesis work started in September 2020. The state-of-the-art review includes the works published before and during the doctoral studies.

2.4.1 Initiative and flight-test experiments

Recent experiments have confirmed the feasibility of direct communication from a LoRa end device to a LEO satellite [80]. To give practical examples, Lacuna Space has launched five LEO satellites with a LoRa gateway on board and confirmed the LoRa message's reception feasibility. To further grow the mMTC connectivity for applications in remote areas, the company expects to increase the number of satellites to 240 by 2025. Swarm Space (SpaceX subsidiary) plans to adopt LoRaWAN to enable two-way communications for IoT applications locations such as oil rigs, wind turbines, and ships in the ocean.

Table 3 provides the details of the satellites featuring LoRa, including the satellites' structure and purpose. Real flight-test experiments reveal that LoRa suffers from a strong Doppler effect, high path loss, and same-channel interference. These observations further motivate this thesis to investigate these challenges. To this end, **Chapter 4** investigates the Doppler effect while **Chapter 5** dives deeper into the signal propagation and interference aspects.

2.4.2 Doppler aspects

As of today, the number of studies investigating the impact of the Doppler effect on LoRa performance remains limited, both for terrestrial and non-terrestrial networks. Compared with terrestrial networks [91, 92], LEO satellites cause a much larger Doppler shift by orbiting the Earth at an average speed in the order of thousands of kilometers per hour (e.g., 27000 km/h for an orbital height of 780 km). Only a few studies assess LoRa robustness against the Doppler effect in a LEO satellite scenario [24, 34–37, 80, 93]. Following laboratory and outdoor tests, the authors of [34, 37] launched a satellite–CubeSat named Norby that orbits at 560 km and operates on 436.7 MHz [24]. Norby has an on-board SX1278 transceiver which supports LoRa connectivity. In [80], Norby's flight-testing experiments are described, establishing the foundation for understanding the LoRa modulation's capabilities and constraints at 436.7 MHz. Similar to the results in [34, 37], the flight-testing experiments confirm LoRa's strong immunity to the Doppler effect when using $7 \leq SF \leq 11$ and bandwidth $B > 31.25$ kHz. These previous studies mostly report experimental results for a fixed and limited parameter subset, mainly for LoRa modulation. There remains a need to evaluate the LR-FHSS performance under the strong Doppler effect. Therefore, **Chapter 4** conducts analysis accounting for a range of communication and orbital parameters to identify the limits of LoRa and LR-FHSS in LEO. To the best of the author's knowledge, this work is the first study to examine the impact of the Doppler effect on LR-FHSS performance.

2.4.3 Frequency spectrum

Since attenuation increases with frequency, the satellite IoT industry focuses on Sub-GHz, L, and S bands for the low data rate use cases. The frequency band is normally divided into channels with limited bandwidth capacity to allow simultaneous transmissions. In DtS networks, interference from simultaneous transmissions of the other end devices is one of the major problems. In earlier studies [94, 95], it was extensively found that an increased traffic load degrades the mMTC connectivity performance and packet delivery ratio (PDR) due to co-channel interference. Similarly, the limited radio spectrum challenges the downlink communication implementation [96, 97]. To avoid the signaling overhead and save resources, earlier studies assume that satellite IoT communications are solely uplink. However, some MAC protocols may require downlink transmissions for traffic scheduling and synchronization. LoRa works on ISM radio bands, and the frequencies are 433 MHz (Asia), 868 MHz (Europe), and 915 MHz (North America). As shown in Table 3, most existing LoRa satellites operate around the 430 MHz band, which experiences the least impact from the Doppler effect and attenuation losses among those allowed for LoRa signals. There remains a need for extensive DtS performance analyses considering other bands, specifically 868 MHz, 915 MHz and the S band.

2.4.4 Massive and heterogeneous traffic

In IoT, data traffic requirements vary from application to application, including the reporting period, payload size, and transmission time. For example, the AIS is an automatic tracking system enabling collision avoidance and safe navigation for ships' operations in the sea. The AIS system broadcasts a message every 2 seconds when navigating at a speed higher than 23 knots [98]. On the contrary, many commercially available Condition Monitoring Systems (CMSs) have a standard 600 second report period. More than this, in smart agriculture applications, end devices efficiently monitor the soil conditions and transmit an uplink packet every 1,800 seconds [55]. Similar to the reporting period, each application's end device density, payload size, and transmission time differ. At the very same time, the number of MTC-enabled satellites is increasing at an impressive speed. Similarly, the number of end devices inside the coverage area of a single satellite could become too large (e.g., a spot beam may be pointed to a huge city, port, or wind farm filled up with a hundred thousand end devices). Massive simultaneous uplink transmissions can degrade the probability of correct packet reception due to high same-channel interference [7, 8]. In this thesis, **Chapter 3** discusses a system model which leverages a capture effect for same-channel interference link-level analysis. **Chapter 5** examines the LoRa and LR-FHSS performance accounting for the interfering signals. Notably, LR-FHSS was released after starting the work for this thesis. Therefore, the publication [43] contributing to **Chapter 5** proposed and developed analytical and simulation models openly available at GitHub [49] to evaluate the LR-FHSS scalability.

2.4.5 Link budget and scalability perspective

Recent state-of-the-art papers and flight tests have investigated the performance of direct communication between the MTC end device and the LEO satellite [24, 80]. Concerning the link budget, a low-power signal could successfully reach an MTC gateway at a satellite over the propagation distance of hundreds to thousands of kilometers. Most of these works examine the DtS link budget for a perfect LOS scenario. However, the network's performance significantly degrades when the channel conditions change due to shadowing, blockage, and obstacles. In conventional wireless communication networks, there are several ways to improve the link budget, including a high antenna gain, increasing the transmit power, implementing diversity techniques, and employing advanced modulation and coding techniques. Despite these options, the limited energy resources in the terrestrial and space segments are one of the key challenges to applying these techniques to satellite IoT networks. The end devices must comply with regional regulations restricting the maximum allowed transmission power [62, 63]. For LoRaWAN operation in Europe, the maximum Effective Isotropic Radiated Power (EIRP) is restricted to +16 dBm and is regulated by the ETSI. Therefore, MTC IoT devices cannot use an EIRP higher than +16 dBm in the ETSI region. Similarly, employing larger high-gain antennas for tiny end devices is very challenging, especially for mobile applications such as wildlife monitoring, which poses challenges. For these reasons, a sufficient share of complexity has to be moved to the satellites (e.g., by introducing high-gain antennas and sufficiently advanced signal processing techniques). The work in this thesis complies with the LoRaWAN protocol and the ETSI regional specifications when configuring the network parameters in **Chapter 5** for link-level analysis as well as the experimental measurements in **Chapter 6**.

2.4.6 Energy efficiency

The user end devices envisioned for DtS IoT will be compact, low-cost, and powered by a battery that is intended to last for years [99]. Optimal transmit power selection mechanisms are often used in terrestrial networks to ensure longer battery life. Therefore, it is important to understand the energy consumption characteristics of DtS IoT end devices. The energy consumption of satellite IoT technology has not been studied extensively. Only a few studies examine the energy efficiency of IoT devices. In [100], the authors model and evaluate the energy performance of Iridium satellite IoT devices. The current consumption was measured using a RockBLOCK Mk2 device with an Iridium 9602 module and supports satellite IoT services. According to their findings, an Iridium IoT device powered by a 2400 mAh battery can maintain operations for an estimated 43.8 days by transmitting a 12 byte message every 10 minutes. The works in [101–103] measure and model LoRa energy consumption for terrestrial networks. Specifically, in [101], experiments were conducted to measure the timing and current consumption of the different states (e.g., radio preparation, transmission, radio off, post-processing) involved in a LoRa transmission. The results also report the impact of LoRaWAN DR settings on battery lifetime. In [103], an empirical analysis of LPWAN reveals that LoRa is more energy efficient when compared to NB-IoT and Sigfox. To the author's knowledge, no previous study has investigated the LR-FHSS current consumption characteristics. Therefore, **Chapter 6** of this thesis bridges this gap by providing empirical insights into the current consumption and ToA of LR-FHSS, complementing the existing theoretical understanding of this technology.

2.5 Summary and discussion

Integrating mMTC and LEO satellites can enable numerous novel applications and global machine coverage. The future satellite communication systems envisioned for IoT must support low-power transmission and many MTC end devices generating radio packets. This chapter provides an overview of satellite IoT communications and key components. Specifically, we discuss network components, satellite form factors, orbits, and payloads. We examine promising satellite systems and radio technologies, including 3GPP and non-3GPP LPWAN. We present an extensive background to two LoRaWAN technologies, namely LoRa and LR-FHSS, which is crucial for understanding the following thesis chapters. This chapter conducts a state-of-the-art review of DtS connectivity developments and identifies open challenges. To summarize the identified challenges, the amount of resources (energy and processing power) available to an end device and satellite is limited. Therefore, it is crucial to investigate the impact of the Doppler effect on LoRaWAN in the LEO scenario to identify LoRa and LR-FHSS limits. For successful operation in LEO, the tiny terrestrial end devices and small satellites envisioned must be capable of estimating and compensating for Doppler shifts without additional computation and power resources. The MTC end devices use low transmit power. Thus, it is important to guarantee that the low-power signals possess a sufficient link budget to reach the satellites effectively. More than this, interference is also one of the critical challenges in MTC satellite networks. The DtS network must be capable of supporting many end devices. The interference coming from terrestrial and non-terrestrial network can degrade the performance. To handle this challenge, using directive antennas for end devices has great potential to improve the connectivity performance but will likely add complexity, increase costs, and result in higher power consumption and signaling overhead. Another practical limitation is that an LEO satellite's fast speed would require a rather complex procedure to track the satellite dynamically. This thesis thoroughly investigates the Doppler aspects in **Chapter 4**, and **Chapter 5** conducts a link budget and scalability analysis of massive LoRaWAN DtS networks for different application scenarios. Finally, **Chapter 6** measures and models the ToA and current characteristics of the LoRaWAN LR-FHSS scheme.

3 Networks architectures and system model

This chapter discusses the two network architectures to deploy satellite IoT networks and highlights their pros, cons, and challenges. This chapter also defines the system model and lays the foundation for the performance analysis in **Chapter 4** and **Chapter 5**. Specifically, it introduces the system model for the Doppler effect and link-level analysis accounting for LEO satellite mobility. The system model discusses the fundamentals of satellite geometry, the Doppler effect, path loss, and channel models used for modeling and performance analysis. The link-level model has two components: the link budget and interference, as in publication [41, 42]. The former evaluates the feasibility of connection between the end device and a satellite, while the latter considers the impact of same-channel interference on communications performance.

3.1 Alternative network architectures

This subsection discusses two alternative communication architectures for satellite IoT – illustrated in Fig. 5 and points out practical, relevant, associated constraints and trade-offs. The DtS allows end devices to communicate directly with a non-terrestrial gateway on a satellite. On the contrary, the second architecture – indirect-to-satellite (ItS) allows an IoT end devices to communicate with a terrestrial gateway further connected to a satellite terminal, which forwards the collected data to the satellite. Fig. 6 shows the alternative configuration options distinguished in blue, gray, and green.

3.1.1 Indirect-to-satellite

This approach forms a hybrid network that comprises a terrestrial network for data acquisition and a satellite backhaul link for transferring the data further. The main advantage is that this approach relies on well-established and proven terrestrial radio access technologies and products. Notably, the terrestrial gateway can aggregate and pre-process the data received from the end devices before being forwarded to a satellite. Three primary advantages of adopting this methodology include (i) the reduced distance between an end device and the terrestrial gateway in comparison to the distance between an end device and a satellite, leading to lower propagation delay and path loss; (ii) the relatively static nature of the link distance, facilitating the use of resilient and energy-efficient modulation-coding schemes, along with network optimization techniques; and (iii) the placement of a gateway on the ground, in contrast to a LEO

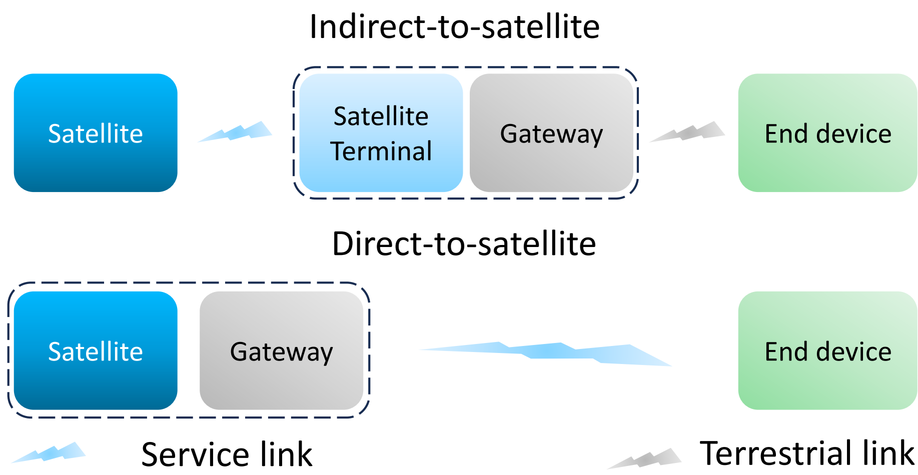

Fig. 5. The basic block diagram for indirect-to-satellite (top) and direct-to-satellite (bottom) connectivity.

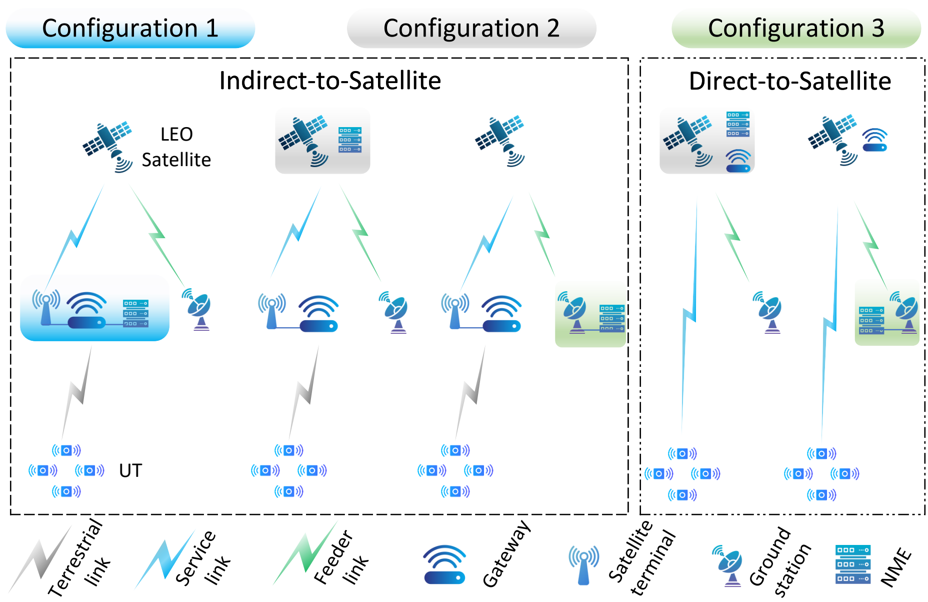

Fig. 6. Network architecture for direct (right) and indirect (left) MTC-based LEO satellite integration with alternative configuration options (Modified from Paper [42]).

satellite, results in a more predictable radio channel without Doppler effect. However, it is important to recognize the downsides of this approach, which are explained below:

- **Dependability on terrestrial infrastructure:** The downside of this approach is the need to create and support a terrestrial infrastructure, which may incur substantial costs. It may even be impossible to deploy a network in a highly dynamic and fragile environment (e.g., sensors floating in the sea).
- **High energy consumption:** An ItS network may need several gateways to provide coverage for the end devices within a specific area, such as offshore wind farms, to illustrate one example. The energy consumption (including gateway and network management entities (NME)) is a potential challenge, which may significantly exceed that of the end devices. Powering multiple gateways might be barely feasible in a fragile environment (e.g., snow covered mountains) due to a lack of power resources and infrastructure.
- **Security aspects:** Finally, a gateway may become a potential bottleneck for the system's reliability and security.

Alternative configuration options

One of the key open questions relevant to this approach is distributing the network-management functionalities within the hybrid network. To give a practical example, many LPWAN grade technologies use a star-of-stars topology composed of gateways (in LoRaWAN/Sigfox, eNodeB – in C-IoT) connected to some management entity (LoRaWAN network server, Sigfox cloud or MME for C-IoT) through an IP-based link. Notably, in this architecture, there are three alternative configuration options, shown as Configuration 1, Configuration 2, and Configuration 3 in Fig. 6, which define the distribution of the network-management functionalities (MNE) , i.e., a network server (NS) and an application server (AS):

1. The NME is located before the satellite link;
2. The NME is located after the satellite link;
3. The NME is located within the satellite constellation.

Each of these alternatives has pros and cons. Specifically, option (1) allows benefiting from aggregation and compression, thus reducing traffic through the satellite. The downside is a more sophisticated and costly on-ground infrastructure, which may result in a bottleneck performance and dependability wise. Option (2) enables the local gateway design to be simplified by moving all the burden of network management to the ground component beyond the satellite link. The downside of this approach is increased traffic through the satellite channel. More than this, the latency, throughput, and reliability constraints coming from satellite links must be considered when configuring the LPWAN network. This aspect must also be considered when selecting the height of the satellite's orbit. LEO satellites enjoy the lowest propagation losses and delays compared to the two other orbit classes. Still, LEO challenge the system with high orbital velocity, bringing high Doppler and rapid channel attenuation fluctuation. Finally, option (3) is a compromise between the two others.

Finally, the network might adopt a hybrid configuration that leverage the functionalities of these three configurations.

3.1.2 Direct-to-satellite

The "direct" architecture empowers each end device to directly transmit data to the satellite onboard a non-terrestrial gateway without relying on any local terrestrial network. The MNE can be placed on a satellite or the terrestrial segment after the satellite. The satellite payload could be designed to be either transparent or regenerative as discussed in Section 2.1.2. DtS simplifies the network topology and makes the ground component more homogeneous. Unlike ItS, DtS can offer reliable connectivity in dynamic and fragile environments. Notably, the satellite higher altitude increases the LOS probability for the end devices. Therefore, a single DtS gateway serves a significantly larger number of end devices than an ItS gateway. Due to its higher coverage, DtS has the potential to offer global connectivity for IoT applications using multiple satellites and optimal constellation designs. However, the implementation of this approach introduces some exciting design challenges. The four notable challenges associated with this approach are as follows:

- **Massive connectivity:** Due to the absence of a terrestrial gateway, the DtS connectivity cannot benefit from data aggregation and compression. Consequently, the satellite gateway will likely receive many uplink radio packets from the end devices deployed within its footprint area. This raises several challenges related to interference and on-board processing capabilities.
- **High path loss:** Notably, most LPWAN MTC technologies operate on Sub-GHz frequency bands and do not suffer from the strong attenuation caused by atmospheric gases, rain droplets, and fog. However, the hundreds to thousands of kilometers of communication distance between an end device and a gateway on satellite introduces high path loss and reduces the signal strength. This also raises the question about the selection (and, importantly, adaptation) of suitable mMTC RAT to enable DtS communication.

- **Satellite mobility:** The LEO satellite mobility changes the channel characteristics and introduces a dynamic round-trip time (RTT) and high Doppler shift, resulting in time and frequency synchronization problems. Notably, time and frequency synchronization are critical for some MAC protocols. For LEO satellites, it is challenging to achieve time and frequency synchronization due to high mobility. The misalignment and loss of synchronization can lead to radio communication failure [48].
- **Non-uniform frequency spectrum:** The radio spectrum of LPWAN technologies exhibits non-uniformity globally. This may require satellites to support and/or switch between the different frequency bands and the use of beamforming, for example.

3.2 System model

This section discusses the satellite geometry, Doppler effect, path loss, and channel models, which are essential for analytical and simulation modeling.

3.2.1 Satellite geometry

To investigate the DtS network performance, it is fundamental to understand the satellite$\leftrightarrow$end-device geometry depicted in Fig. 7.

Slant distance

The mobility of a LEO satellite rapidly changes the elevation angle E, resulting in variations of the slant distance d, defined as the link distance between the end device and the gateway deployed on the Earth-orbiting satellite. Based on the geometric relations shown in Fig. 7, one can find d from a given E and vice versa as [88, 90]

$$d(E) = R\left[\sqrt{\left(\frac{H+R}{R}\right)^2 - \cos^2(E)} - \sin(E)\right], \tag{4}$$

$$E(d) = \sin^{-1}\left(\frac{H^2+2HR-d^2}{2dR}\right), \tag{5}$$

where R = 6371 km is the radius of Earth, H is the orbital height of the satellite and E is expressed in degrees.

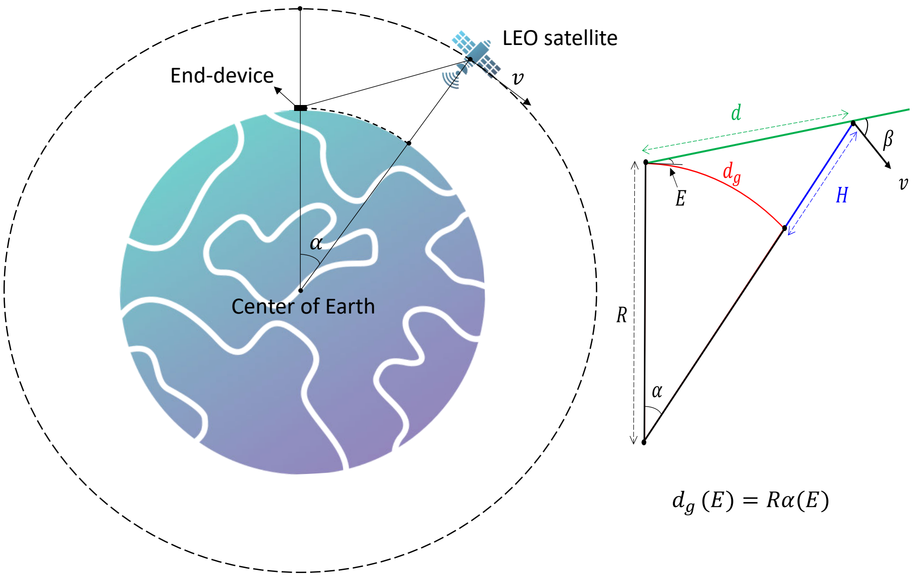

Fig. 7. The satellite $\leftrightarrow$ end-device (ground terminal) basic geometry (Modified from Paper [45]).

Ground range

The projection on the Earth's surface of the segment connecting the end-device and the satellite creates an arc defined as the ground range $d_g(E)$. The length of the arc is equivalent to the product of Earth's radius R and the central angle $\alpha(E)$ as [104, 105]

$$d_g(E) = R\,\alpha(E) = R\sin^{-1}\left(\frac{d(E)\cos(E)}{R+H}\right), \tag{6}$$

where α is in radians.

Visibility time

For a given H, the maximum satellite visibility time V_T depends on $d_g(E_{\min})$. Let $E_{\min}$ be the minimum elevation angle, which, in the most simple case, will be equal to 1 degree. Following the satellite orbital velocity and ground range relation, the visibility time (V_T) is defined by

$$V_T = 2\frac{d_g(1)}{v}, \tag{7}$$

where v is the velocity of the satellite in the circular orbit and can be computed by $v = \sqrt{\frac{g \cdot R}{1+\frac{H}{R}}}$, where g is gravitational acceleration on the Earth [34].

3.2.2 Doppler effect

The DtS communication undergoes a significant Doppler effect due to the relative motion between the terrestrial end device and the Earth-orbiting LEO satellite. The communication performance can degrade due to the shift in the carrier frequency of the received signal [34–37, 80, 91–93]. Therefore, it is crucial to study the impact of the Doppler effect on communication.

Doppler shift and rate

The relative motion of the satellite relative to a stationary observer/end device on the Earth's surface introduces a significant frequency shift in the received radio signal, hindering proper demodulation. Specifically, at a given instant of time, the difference between the transmitted carrier frequency F_{C} and the received carrier frequency $F_{\mathrm{R}}(t)$, the latter varying in time owing to the satellite motion, is known as Doppler shift, given by

$$F_{\mathrm{D}}(t) = F_{\mathrm{R}}(t) - F_{\mathrm{C}}, \tag{8}$$

whereas its derivative

$$\Delta F_{\mathrm{D}}(t) = \frac{d(F_{\mathrm{D}}(t))}{dt}, \tag{9}$$

is called the Doppler rate.

Given the geometry depicted in Fig. 7, the mathematical expression of $F_{\mathrm{R}}(t)$ as a function of F_{C} is given by [34]

$$F_{\mathrm{R}}(t) = \frac{1}{1 + \frac{v}{c}\cos(\beta(t))} F_{\mathrm{C}}, \tag{10}$$

with

$$\cos(\beta(t)) = \frac{\sin(\varphi(t))}{\sqrt{(1+\frac{H}{R})^2 - 2(1+\frac{H}{R})\cos(\varphi(t)) + 1}}, \tag{11}$$

where β is the angle between the satellite velocity vector and the direction to the terrestrial end-device and $\varphi(t)$ is expressed as [34]

$$\varphi(t) = t\sqrt{\frac{g}{R}}\left(1 + \frac{H}{R}\right)^{-3/2}, \tag{12}$$

being $t = -\frac{V_T}{2} : 1 : \frac{V_T}{2}$ the relative elapsed time. Note that $t = 0$ is when the satellite is at $E = 90°$ and has a minimum slant distance $d = H$ to the observer/end-device.

3.2.3 Path loss models

This thesis uses two path loss models for different channel conditions and scenarios. Specifically, the publications [41,43] use a free space path loss model, publications [42, 44] use a log-distance path loss model.

$$\Gamma = \begin{cases} 10\log_{10}\left(\left(\frac{4\pi d F_C}{c}\right)^{\eta}\right) & \text{for free space} \\ \Gamma_0 + 10\log_{10}\eta\frac{d}{d_0} + X_g & \text{for log-distance} \end{cases}, \tag{13}$$

where F_C is the carrier frequency, d is the path length between the transmitter and receiver (for DtS, d is the slant distance calculated by (4)), η is the path loss exponent, c is the speed of light. For log-distance path loss model, Γ_0 is the constant free space path loss at d_0 reference distance, and $X_g \sim \mathcal{N}(0, \sigma^2)$ is a zero-mean Gaussian random variable with standard deviation σ, which accounts for the shadowing.

3.2.4 Channel fading

The channel coefficient (h) accounts for the nature of fading (Rayleigh or Rician) and is expressed as

$$h = \sqrt{\frac{K}{K+1}}h_{LOS} + \sqrt{\frac{1}{K+1}}h_{NLOS}, \tag{14}$$

where K is the Rician factor. $K = 0$ denotes the Rayleigh fading, while $K > 0$ (typically $K > 1$) for Rician fading.

3.3 Link level analysis

It is worth recalling that LEO satellites orbit hundreds of kilometers far from the Earth's surface. The orbital geometry creates a large coverage footprint and a long link distance between the end devices and the satellite, resulting in a high co-channel interference and a high path loss. In this thesis, a link-level analysis answers the following three questions:

- **Question 1:** Does the low-power signal transmitted by terrestrial end devices maintain a sufficient signal-to-noise ratio (SNR) upon reaching the satellite, making communication feasible?

– **Question 2:** What is the impact of interference, taking into account the capture effect on DtS performance, specifically considering collisions from simultaneous transmissions of other end devices within the satellite footprint? Will the packet be received at the satellite in the presence of same-channel interference?
– **Question 3:** How do the link budget and interference jointly influence communications performance considering different data traffic scenarios and channel conditions?

To answer similar questions in terrestrial networks, the state-of-the-art LoRa publications [76–79, 106] use term *success probability* (P_S) to assess the network performance. P_S is a product of two probabilities namely the *connection probability* (P_{SNR}), which accounts for the probability of maintaining sufficient link budget, and the *capture probability* (P_{SIR}), which evaluates random access scalability aspects accounting for the capture effect. P_{SNR} and P_{SIR} answer **Question 1** and **Question 2**, respectively. This thesis uses the same notation for link-level simulations to align with the existing literature. To answer **Question 3**, the overall *success probability* of packet delivery is calculated as

$$P_S = P_{SNR} P_{SIR}, \tag{15}$$

3.3.1 Connection probability

This work assumes that in the absence of interference, a gateway successfully decodes an uplink packet if the SNR of the received signal is higher than the demodulator's SNR threshold. For LoRa modulation, the SF-specific SNR threshold is equal to $D_{SNR} = \{-6, -15, -20\}$ dB for SF7, SF10, and SF12, respectively [106]. A minimum SNR of $D_{SNR} = 3.96$ dB is required for successful LR-FHSS signal reception [88, 90]. The probability of the correct packet reception, named *connection probability*, is denoted by

$$P_{SNR} = \mathbb{P}\left[\frac{P_{tx} G_t G_r \Gamma' |h|^2}{\sigma_w^2} \geq D_{SNR}\right], \tag{16}$$

where $\Gamma' = \frac{1}{\Gamma}$, $\sigma_w^2 = -174 + NF + 10\log_{10}(B)$ dBm is the variance of the additive white Gaussian noise (AWGN) [77], NF = 6 dB is the gateway receiver's design architecture noise figure, G_t is the end device's antenna gain, and G_r is the directive antenna gain of each beam generated by the satellite.

3.3.2 Capture probability

Empirical and analytical studies have demonstrated the presence of the capture effect for LoRa radio signals, which enables a receiver to demodulate the stronger signal under interference from the weaker ones. To account for the co-channel interference, this thesis applies a packet collision model that accounts for the capture effect. Mathematically, the *capture probability* accounting for the same-channel interference can be defined as

$$P_{SIR} = \mathbb{P}\left[\frac{P_{tx} G_t G_r \Gamma' |h|^2}{\sum P_{tx} G_t G_r \Gamma'(i) |h_i|^2} \geq \delta\right], \tag{17}$$

where i denotes the interfering signal and δ is the capture effect power threshold [76]. Notably, this model considers no inter-channel interference between the transmissions in the different frequency channels.

3.4 Analytical and simulation tools

We use this system model to develop MATLAB-based Monte Carlo simulators and analytical tools. These tools enable us to gain a deeper understanding of the feasibility and potential trade-offs linked with LoRaWAN DtS connectivity. We have made these tools openly accessible to the research community on GitHub [49–51, 53].

3.5 Summary and discussion

This chapter discusses two alternative network architectures for MTC and LEO satellite integration, highlighting the pros, cons, and trade-offs. The system model is presented to evaluate the DtS performance, which serves as a foundation for the analysis in the remaining thesis, specifically in **Chapter 4** and **Chapter 5**. The system model in the current chapter discusses the satellite's orbital geometry, Doppler effect model, and link level model. In DtS connectivity, a visible satellite can lose synchronization with a terrestrial end device due to the Doppler effect, causing a time-varying Doppler shift and rate. The Doppler shift impacts the receiver's ability to lock onto the received carrier frequency when an incoming packet is detected (i.e., at the beginning of the packet reception). On the contrary, the Doppler rate is related to the receiver's ability to remain locked onto the received carrier despite deviations from the initial value over time. To this end, **Chapter 4** investigates the impact of the Doppler effect on LoRa and LR-FHSS DtS using the model presented in the current chapter. For the link-level studies, the *connection probability* examines the communication link budget accounting for the high path loss caused by hundreds to thousands of kilometers of link distance. In a signal's link budget, the transmit power and the antenna gain are two key elements. Notably, the wireless end devices follow regional specifications. Therefore, the maximum allowed transmit power cannot exceed a certain threshold. A higher satellite antenna gain can help improve the link budget in the space segment. However, it may increase the size of the satellite, resulting in higher launch costs. Therefore, the key antenna design requirements include a lightweight structure, high efficiency in the space environment, and the ability to handle multiple beam operations simultaneously. Similarly, the *capture probability* accounts for co-channel interference, which is one of the critical challenges in satellite networks. A non-terrestrial LoRaWAN gateway deployed on a satellite will likely receive many uplink radio packets from the end devices deployed within its footprint. Therefore, if not carefully accounted for, the interfering radio signals can significantly degrade the DtS network performance due to possible destructive collisions. Finally, the overall *success probability* is the product of the connection and the capture probability, accounting for link budget and interference aspects. Maintaining higher *connection* and *capture probability* is essential to ensure reliable communication. For instance, the *connection probability* will be high in scenarios where an end device operates in an open sky with perfect LOS. However, the *capture probability* might decrease if the same end device is surrounded by thousands of neighboring end devices served by the same satellite. Consequently, despite possessing a strong SNR, the satellite might fail to receive the data from the target end device successfully. Bearing in mind these considerations, the performance analysis of LoRa and LR-FHSS are presented in **Chapter 5**.

4 LoRaWAN direct-to-satellite communications: doppler aspects

The Doppler effect is one of the main challenges for satellites orbiting in LEO. As of today, only a few studies examine the influence of the Doppler effect on LoRaWAN DtS performance. Specifically, the majority of the available literature consists of empirical studies that analyze the Doppler effect on LoRa solely for a specific set of communication parameters [34–37, 80, 91–93]. To the best of my knowledge, there is no work available that assesses the impact of Doppler effect on LR-FHSS DtS connectivity. There remains a need for extensive examination of LoRaWAN DtS performance under a strong Doppler effect in the LEO scenario. This chapter is primarily based on publication [45], which assesses the influence of the Doppler effect on the reliability of LoRa satellite links. Notably, the LR-FHSS outcomes presented in this chapter in Fig. 14 are notably original and exclusive to this work, with no prior publication in the academic literature. This chapter introduces an analytical model designed to investigate packet losses, which distinguish the effect of Doppler shift from the Doppler rate caused by the variation in the relative speed of a LEO satellite concerning a terrestrial IoT end device alone. Leveraging the key findings of our work [45], this chapter summarizes the effects of key communications parameters and settings, such as bandwidths, carrier frequency, the orbital height of LEO satellites, code rate, and LoRaWAN LDRO. Notably, these results can facilitate the selection of suitable parameters for future system designs.

4.1 Doppler effect components

This chapter extensively studies the Doppler effect and distinguishes between static Doppler, which refers to the Doppler shift experienced by the receiver at the beginning of packet reception, and the dynamic Doppler also known as the Doppler rate, which represents the additional, time-varying, frequency shift that occurs throughout the packet reception interval. The former pertains to the receiver's ability to lock onto the received carrier frequency when an incoming packet is detected (i.e., at the beginning of the packet reception). The latter is related to the receiver's ability to remain locked onto the received carrier despite its deviations from the initial value over time.

LoRa DtS state-of-the-art results in [34–37, 80, 91–93] consider both the Doppler shift and the Doppler rate, and the key findings indicate:

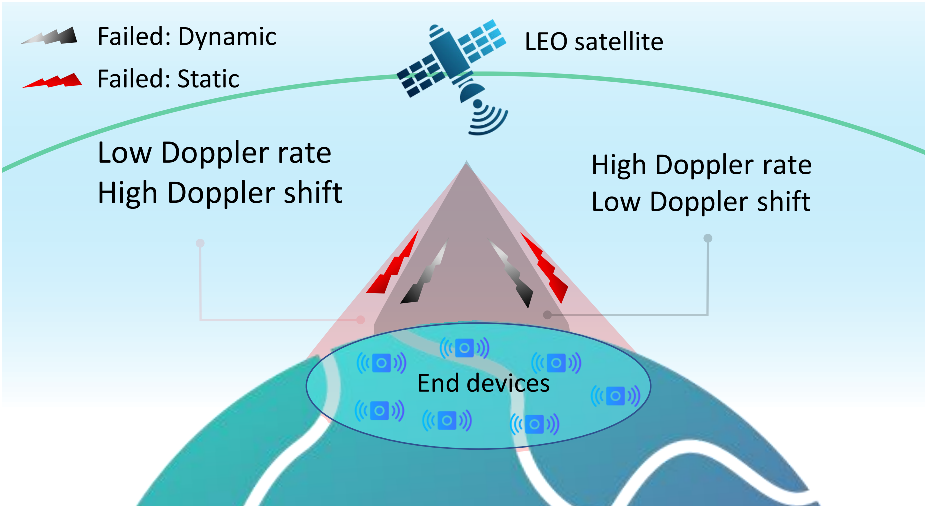

Fig. 8. Illustration of the communication failure due to Doppler shift (failed: static) and Doppler Rate (failed: dynamic) in a DtS IoT scenario (Modified from Paper [45]).

- the Doppler shift degrades the communication link at the lowest elevation angles and the maximum link distance.
- also, the Doppler rate leads to packet losses at high elevation angles when the satellite is closer to the end-device on the ground.

To visually present this problem, Fig. 8 illustrates the region affected by the Doppler shift marked in red and the Doppler rate indicated in gray.

The previous studies present experimental results obtained by considering only a limited subset of the parameters that affect the sensitivity of LoRa to the Doppler effect. Moreover, some critical settings (e.g., the orbital height) were fixed. Finally, of utmost importance, most of these studies and operational LoRa satellites focused solely on communications around the 433 MHz band, which experiences the least impact from the Doppler effect among those allowed for LoRa signals [80]. This further motivates a comprehensive investigation into LoRa DtS performance for higher bands. To the best of my knowledge, no existing research or literature currently evaluates the influence of the Doppler effect on LR-FHSS. The current chapter addresses this shortcoming by investigating all aspects affecting the robustness of LoRa and LR-FHSS DtS communications to the Doppler effect.

4.2 Analytical framework

Flight-test experiments [80] and Semtech documents [63] on the LoRa modulation provide the Doppler shift and rate tolerance thresholds for robust demodulation against the Doppler effect. These aspects will be discussed in the following section.

Doppler shift tolerance

According to flight-testing experimental work [80] and Semtech documents [82, 87], LoRa tolerates a frequency offset up to $\pm 25\%$ of the bandwidth B without any sensitivity degradation. Thus, the immunity limit for the static Doppler becomes

$$F_{\text{static}} = \pm 0.25 \times B. \tag{18}$$

Semtech does not provide any explanation for this threshold. The tolerance limit for the frequency offset depends on the hardware and receiver design. Considering the integration of both LoRa and LR-FHSS modulation in the new Semtech devices, it can be assumed that the LR-FHSS frequency offset tolerance is the same as the LoRa modulation.

Doppler rate tolerance

Similarly, proper demodulation requires that the carrier frequency variation within the duration of the received packet, which is due to the experienced Doppler rate, does not exceed a given threshold. More precisely, the carrier frequency variation over the packet reception time (between the beginning and the end of the packet) should remain below the thresholds as given in [83, 107].

$$F_{\text{dynamic}} = \begin{cases} \frac{16\times B}{3\times 2^{\text{SF}}} & \text{for LoRa if LDRO enabled,} \\ \frac{1\times B}{3\times 2^{\text{SF}}} & \text{for LoRa if LDRO disabled,} \\ 300\ \text{Hz/s} & \text{for LR-FHSS.} \end{cases} \tag{19}$$

Notably, LDRO is recommended when the LoRa symbol duration is more than 16.38 ms [108]. With B=125 kHz, SF11 and SF12 have symbol times greater than 16.38 ms. Thus, LDRO is mandated by the LoRaWAN specification for these SFs. Due to the larger frequency separation between chirps, LDRO enhances the LoRa immunity to dynamic Doppler. Table 4 shows the values of LoRa F_{dynamic} for different SF and bandwidths B, with and without LDRO. LR-FHSS can tolerate a frequency drift up to 300 Hz/s (subject to 1.5 dB sensitivity degradation), making it a prominent

Table 4. LoRa intra-packet dynamic Doppler shift F_{dynamic} limits in Hz.

SFs	LDRO Disabled		LDRO Enabled	
No.	125 kHz	500 kHz	125 kHz	500 kHz
SF7	325.5	1302.1	5208.3	20833.3
SF8	162.8	651	2604.2	10416.7
SF9	81.4	325.5	1302.1	5208.3
SF10	40.7	162.8	651	2604.2
SF11	–	81.4	325.5	1302.1
SF12	–	40.7	162.8	651

technology for LEO scenarios [63]. To model the effect of the Doppler effect on LoRa and LR-FHSS DtS performance, we suggest the following conditions to account for the packet loss due to (i) static Doppler, (ii) dynamic Doppler and (iii) joint static and dynamic Doppler.

Let $L_{\text{static}}(t) \in \{0,1\}$, which reflects a successful or lost packet due to Doppler shift, where:

$$L_{\text{static}}(t) = \begin{cases} 1 & \text{if } |F_{\text{D}}(t)| \geq |F_{\text{static}},| \\ 0 & \text{else.} \end{cases} \tag{20}$$

Let $L_{\text{dynamic}}(t) \in \{0,1\}$, which reflects a successful or lost packet due to Doppler rate, where:

$$L_{\text{dynamic}}(t) = \begin{cases} 1 & \text{if } |\Delta F_E| \geq F_{\text{dynamic}}, \\ 0 & \text{else,} \end{cases} \tag{21}$$

with ΔF_E denoting the overall change in the carrier frequency from the beginning to the end of the packet, defined as

$$\Delta F_E = \begin{cases} F_{\text{D}}[t_{\text{start}}] - F_{\text{D}}[t_{\text{end}}] & \text{for LoRa} \\ \left(\frac{F_{\text{D}}[t_{\text{start}}] - F_{\text{D}}[t_{\text{end}}]}{\text{ToA}}\right) \times 10^3 & \text{for LR-FHSS} \end{cases}, \tag{22}$$

where t_{start} denotes the time instant at the beginning of the packet reception, and $t_{\text{end}} = t_{\text{start}} + \text{ToA}$ represents the time instant at the end of the packet reception. One can calculate the ToA (in milliseconds) for LoRa using (1), and for LR-FHSS, either (2) or (3). However, the LR-FHSS experimental measurements conducted in **Chapter 6** reveal that these models are inaccurate and exhibit a higher relative error rate of -9.2 to 3.4% compared to the measured and our proposed ToA model. Thus, it is recommended

Table 5. **LoRaWAN key communication parameters.**

Parameters	Values
General	
Orbital height	560-1500 km
Packet reporting period (R_p)	5 s
LoRa	
Bandwidth (B)	31.25, 62.5, 125, 250, 500 kHz
Carrier frequency (F_{C})	433, 436.7, 868 MHz & 2.1 GHz
Spreading Factor (SF)	7, 10, 12
Code Rate (CR)	4/5
MAC Payload	1-59, 55, 250 bytes
LDRO	Enabled & Disabled
LR-FHSS	
OCW Bandwidth (B)	137 kHz
Carrier frequency (F_{C})	433, 868 MHz & 2.1 GHz
Code Rate (CR)	2/3
Header replica (N_H)	1
PHY Payload	55 bytes

to use the LR-FHSS ToA model (33) proposed in **Chapter 6** based on [46] which exhibits a relative error of less than 0.3%.

Let $L_{\mathrm{joint}}(t) = L_{\mathrm{static}}(t) \times L_{\mathrm{dynamic}}(t)$ be the packet loss due to the joint Doppler shift and Doppler rate, where $L_{\mathrm{joint}}(t)$ is 1 for a lost packet and 0 otherwise. It is important to mention that we use $L_{\mathrm{static}}(t)$, $L_{\mathrm{dynamic}}(t)$, and $L_{\mathrm{joint}}(t))$ in Algorithm 1, intending to help potential readers to understand how we have generated the results for our analysis. Algorithm 1 assesses the performance during a full satellite visibility time interval, i.e., $-\frac{V_T}{2} \leq t \leq \frac{V_T}{2}$; therefore, lines 9-27 in Algorithm 1 represent a loop going through all possible time instances (t) and covering the entire range of elevation angles.

4.3 Network configurations

Our scenario considers an ideal satellite pass, assuming that the satellite passes directly over the end device and the elevation angle reaches 90°. Table 5 shows the key parameters for the network configurations and orbital heights investigated. This study uses the analytical framework detailed in Chapter 3, Section 3.2 and the MATLAB

Satellite Communications (SatCom) Toolbox to model the time-varying Doppler shift in the LoRaWAN DtS communication links. To compare with actual flight-tests [80], the SatCom toolbox uses Norby's TLE to calculate the Doppler shift and rate. Norby is 6U CubeSat nanosatellite launched into LEO on September, 2020 [80]. Therefore, unless otherwise stated, this work considered H = 560 km as in [80]. For the same reason, unless otherwise indicated, the LoRa DtS network is configured to F_C = 436.7 MHz, and a variable bandwidth of B = 31.25, 62.5, 125 kHz and $P_L = 55$ bytes. In the LR-FHSS configuration, the bandwidth remains constant, and a small payload of 10 bytes is used to investigate the impact of the header replica, code rate, and data rate configuration on the system performance. To facilitate potential readers and the reproduction of results, we have made the script code for the proposed analytical framework openly accessible on GitHub [52].

4.4 Numerical results

This chapter is based on the paper [45], which extensively investigates the impact of SFs, payload, bandwidth, LDRO, payload, and orbital height on LoRa DtS performance. However, this chapter only presents selected results highlighting the impact of the Doppler effect on LoRa DtS performance. It is worth recalling that this analysis only accounts for packet losses due to the Doppler effect. The model considers a single end device with no co-channel interference. Secondly, the model does not consider the channel link budget and assumes that the signal is strong enough to reach a LEO satellite in orbit. Note that the interference and link budget have been extensively and separately studied in the next chapter of this thesis. For a complete LoRa and LR-FHSS DtS network analysis, consideration of the link budget and interference can be added on top of the current Doppler effect model. Fig. 9 shows the Doppler shift and Doppler rate for carrier frequencies F_C equal to 436.7 MHz, 868 MHz, and 2.1 GHz, with solid lines denoting Norby's TLE[3], corresponding to H = 560 km, and markers representing analytical results, respectively.

4.4.1 LoRa

Bandwidth

As (18) indicates, the LoRa modulation becomes increasingly vulnerable to the static Doppler as the bandwidth B decreases. Considering B = 31.25 kHz and a payload length

[3]A TLE is a data format encoding a list of orbital elements of an Earth-orbiting object.

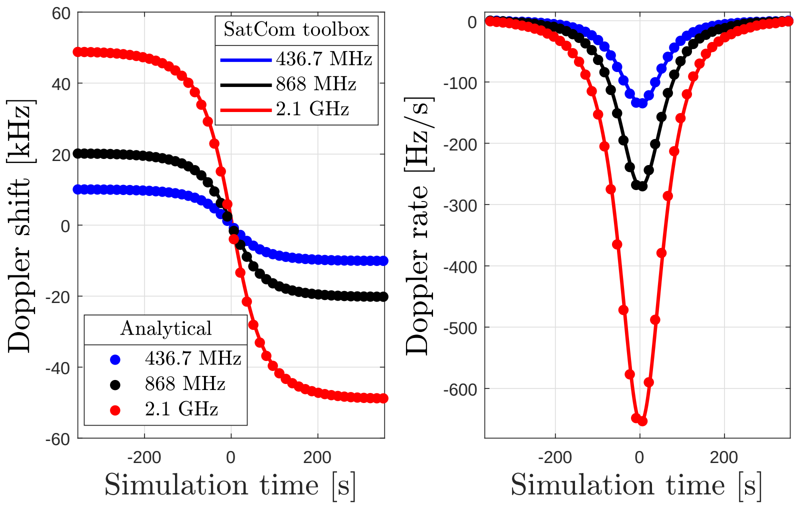

Fig. 9. Comparison of the Doppler shift and Doppler rate generated from TLE and the analytical framework (Under CC BY 4.0 license from [45] ©2024 Authors).

of 55 bytes, Fig. 10 shows the correct (blue dot) or incorrect (black, red, and yellow dots) reception of packets for each time instant (x-axis) and corresponding elevation angle E (y-axis) during the satellite visibility interval. The color code specified in the legend makes it possible to distinguish whether the failure is due to a static Doppler effect, dynamic Doppler effect, or both.

It can be observed that, in the considered case, the static Doppler shift leads to packet losses for $E \leq 40°$, whichever SF is adopted. Differently from SF7, which performs well when $E > 40°$, SF10 and SF12 are irreparably affected by the dynamic Doppler shift (the change in frequency from the beginning until the end of the packet) caused by the rate of change of the Doppler shift. Higher elevations lead to higher (in terms of absolute value) Doppler rates (see Fig.9), which, together with the longer ToA due to a higher SF, cause the frequency deviation within the packet duration to exceed the threshold in Table 4. In particular, SF10 appears vulnerable to the dynamic Doppler shift from $E > 40°$, while SF12 starts to suffer as early as $E > 13°$.

Better performance is instead expected for larger bandwidths. Indeed, increasing B raises F_{static}, thus improving the robustness of LoRa to the static Doppler, and reduces ToA, thus increasing the ability to combat the dynamic Doppler effect. This analysis reveals that SF7 and SF10 have strong immunity to the Doppler effect when $B = 62.5$ kHz and $B = 125$ kHz, with correct packet reception in 100% of cases. However, as evident

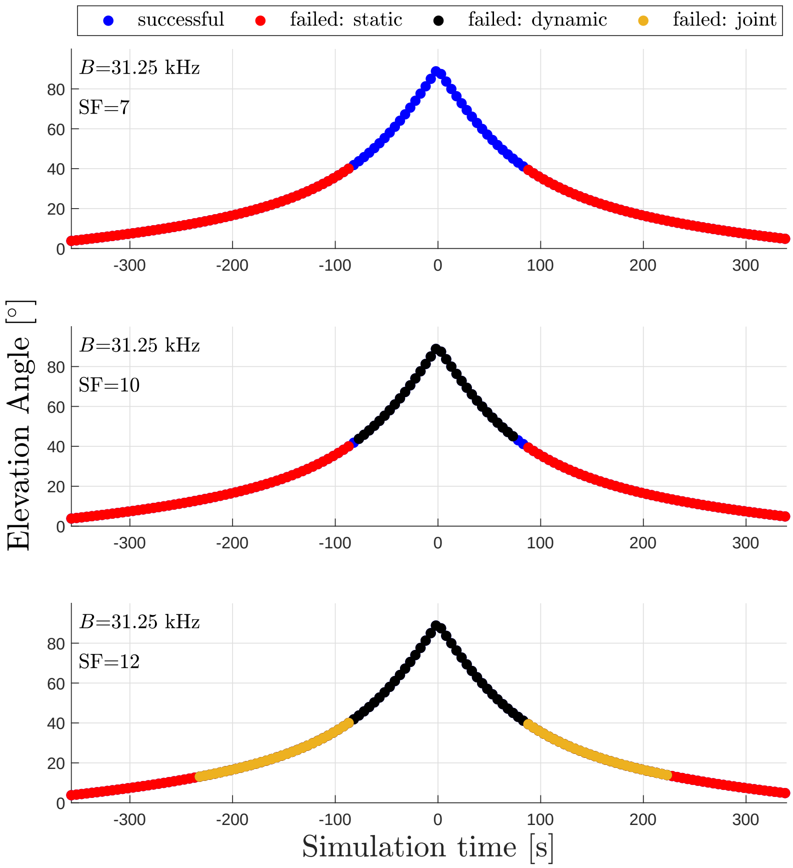

Fig. 10. LDRO-enabled LoRa performance under the Doppler effect at $B = 31.25$ kHz, $P_L = 55$ bytes, F_C = 436.7 MHz, and H = 560 km for SF = [7, 10, 12] with ToA = [595, 3285, 10517] ms, respectively (Under CC BY 4.0 license from [45] ©2024 Authors).

in Fig. 11, SF12 remains vulnerable to the dynamic Doppler effect when $E > 24^\circ$ and $E > 45^\circ$ for B = 62.5 kHz and B = 125 kHz, respectively.

Low Data Rate Optimization

The analysis reveals that SF7 has a high tolerance to intra-packet frequency deviations, with and without LDRO. Specifically, when B = 125 kHz, SF7 supports a maximum MAC payload of 250 bytes, resulting in ToA = 548 ms. From Fig. 9 one observes that

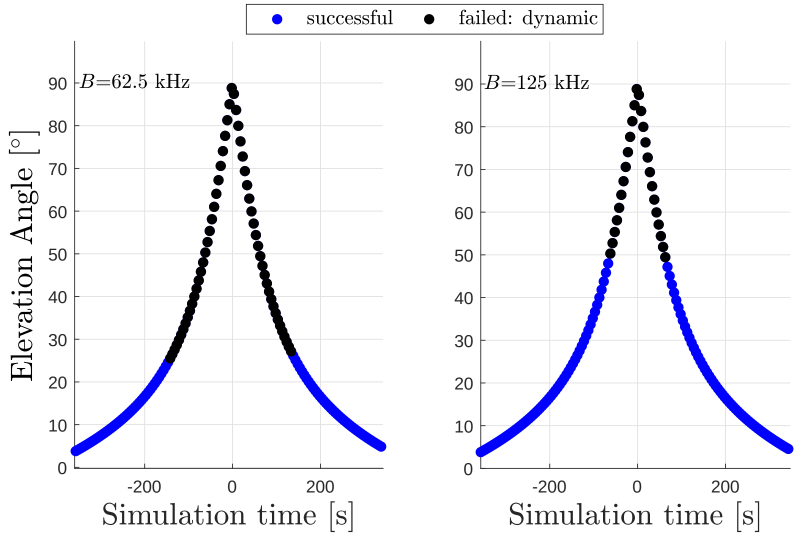

Fig. 11. LDRO-enabled LoRa performance under Doppler effect for $SF = 12$ at B = 62.5 kHz and 125 kHz, $P_L = 55$ bytes, ToA = [5259, 2629] ms, F_C = 436.7 MHz, and H = 560 km (Under CC BY 4.0 license from [45] ©2024 Authors).

when F_C = 436.7 MHz, the maximum Doppler rate is 144 Hz/s. Consequently, a 548 ms long SF7 packet will experience a dynamic Doppler shift of 78.9 Hz, far lower than the limits in Table 4. On the other hand, by increasing the SF, and consequently ToA, one expects less immunity to the dynamic Doppler effect. Looking at Fig. 12, packet losses occur for an SF10 packet of 59 bytes (the maximum allowed length) when LDRO is disabled and $E \geq 47°$. Interestingly, no packet loss is observed when LDRO is enabled.

Carrier frequency

The role played by the carrier frequency is investigated in Fig. 13, in the case $B = 125$ kHz and $P_L = 55$ bytes for SF = [7, 10, 12] with ToA = [149, 821, 2629] ms. It can be seen that, despite the high Doppler effect at 868 MHz, SF7 and SF10 (and therefore also the intermediate SF) the results show high stability without any losses, whereas SF12 suffers from the dynamic Doppler effect (owing to the increased ToA) when $E \geq 35°$. However, significant packet losses occur by increasing the carrier frequency to 2.1 GHz. Specifically, SF7 and SF10 packets are lost when $E \leq 50°$ due to the static Doppler effect, whereas SF12 always fails to deliver packets due to static, dynamic, and joint Doppler shifts.

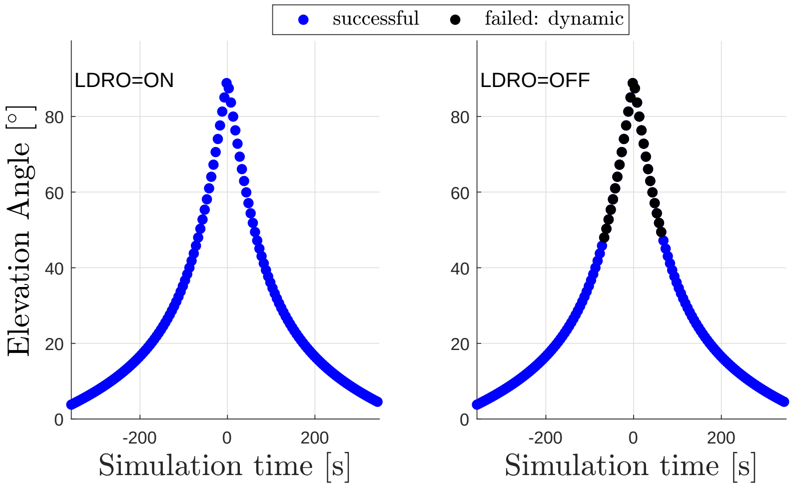

Fig. 12. The impact of LDRO on LoRa performance for SF=10 and B = 125 kHz, F_C = 436.7 MHz, H = 560 km with maximum allowed MAC payload $P_L = 59$ bytes (Under CC BY 4.0 license from [45] ©2024 Authors).

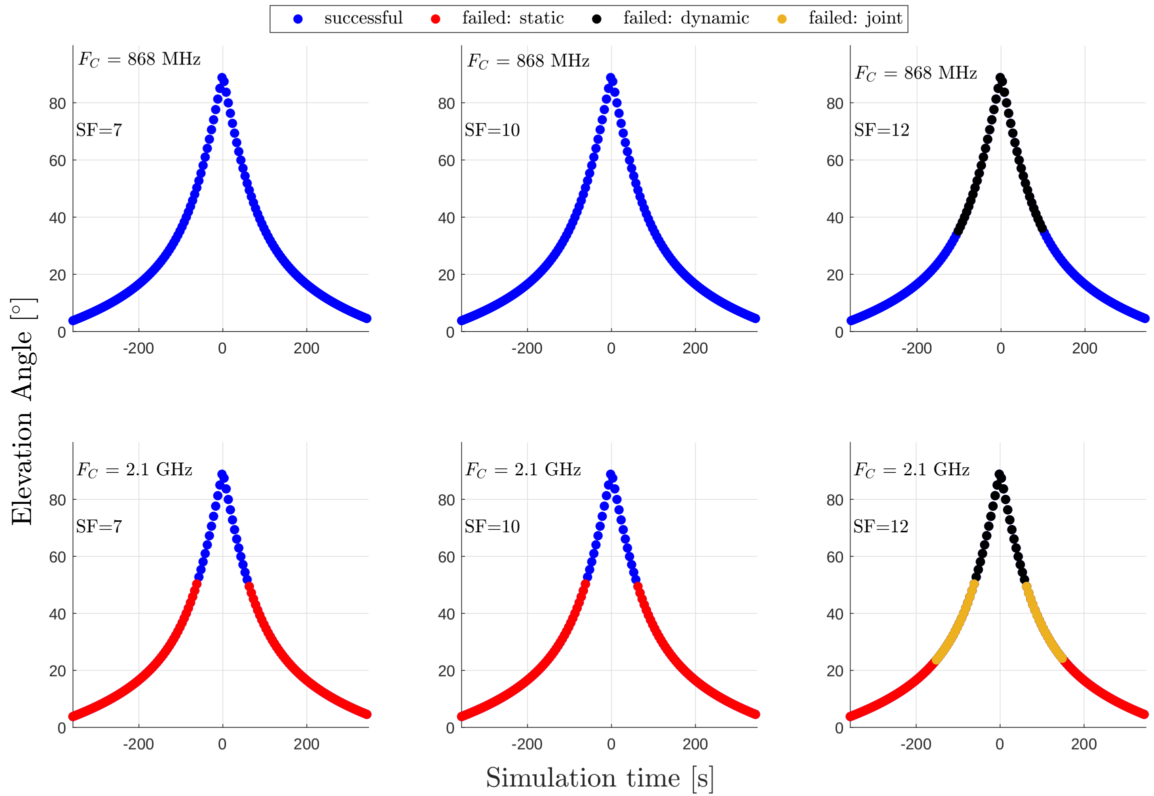

Fig. 13. The impact of a high carrier frequency on LDRO-enabled LoRa performance for $B = 125$ kHz, H = 560 km and $P_L = 55$ bytes for SF = [7, 10, 12] with ToA = [149, 821, 2629] ms, respectively (Under CC BY 4.0 license from [45] ©2024 Authors).

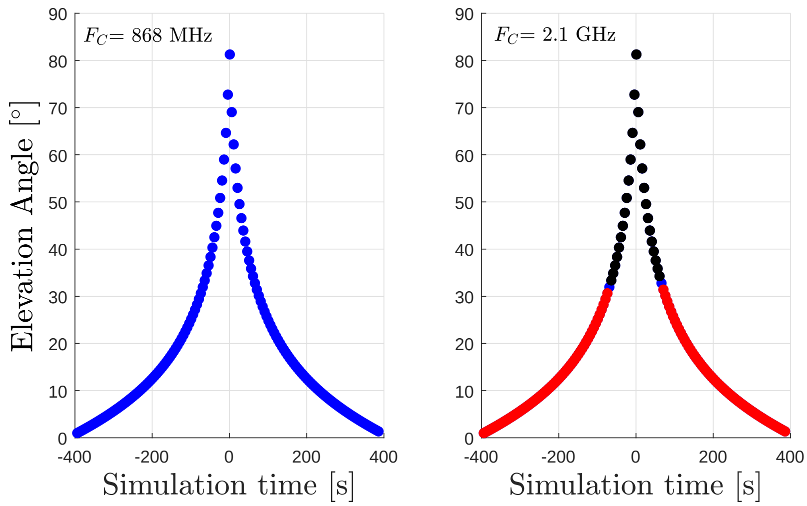

Fig. 14. The impact of the carrier frequency on the LR-FHSS performance for and B = 137 kHz, F_C = 868 MHz and 2.1 GHz, H = 560 km with PHY payload $P_L = 55$ bytes, header replica N_H = 1, CR = $\frac{2}{3}$.

4.4.2 LR-FHSS

It is worth recalling that the whole frequency band is divided into multiple OCW channels [87]. For frequency hopping, a single LR-FHSS OCW channel is subdivided into multiple subchannels, named OBW channels. Each OBW has a bandwidth of 488 Hz. This work considers a 137 kHz OCW channel for evaluating the impact of the Doppler effect on the LR-FHSS DtS performance.

Carrier frequency

Fig. 9 demonstrates the Doppler shift and Doppler rate for 436.7 MHz, 868 MHz, and 2100 GHz. An increase in the carrier frequency increases the Doppler shift, resulting in a higher Doppler rate. The peak Doppler rate for these bands is -134, -270, and -653 Hz/s, respectively. The LR-FHSS performance under the influence of the Doppler shift for 868 MHz and 2100 GHz bands is depicted in Fig. 14. 868 MHz (also the lower bands) remains robust against the static and dynamic Doppler shift for the entire range of elevation angles. On the contrary, the connectivity in the 2.1 GHz band is affected by static and dynamic Doppler shift. Specifically, the static Doppler shift causes packet losses for $E < 30°$ when configured to a 137 kHz OCW channel. The dynamic Doppler shift degrades the performance for elevation angles $E > 33^\circ$ due to a higher Doppler rate of -653 Hz/s in the 2.1 GHz frequency band and at an orbital height of 560 km.

Header replicas and Code rate

Unlike LoRa modulation, LR-FHSS allows the header replications $N_H = 1 \dots 4$, which increases the probability of successful packet reception at the gateway, costing a higher ToA [88, 90, 109]. The dynamic Doppler shift accounts for the carrier frequency variation over the packet reception time. Each header duration is 233 ms; higher header replicas increase the packet ToA. This is unlike the LoRa tolerance to the Doppler rate, which accounts for a total change in the Doppler shift between the packet's beginning and end. The LR-FHSS Doppler rate tolerance threshold is a function of time in (19) which is 300 Hz/s and equivalent to 0.3 Hz/ms [63] . The key factors influencing the Doppler rate are the carrier frequency and satellite orbital height. Therefore, following (19), the number of header replicas does not influence the LR-FHSS performance at F_C = 868 MHz and 2.1 GHz, H = 560 km with a PHY payload of $P_L = 55$ bytes. Similar to header replications, the code rate contributes to the ToA. Our initial observations do not reveal any impact of these parameters on the LR-FHSS performance under the Doppler effect. However, these results might differ for other configuration settings, thus, the impact of the Doppler effect on LR-FHSS requires further studies.

4.5 The impact of key parameters

This chapter is built on publication [45], which extensively examines LoRa DtS accounting for the effects of SFs, payload, bandwidth, LDRO, and orbital height. However, the current chapter presents only selected results, with the LR-FHSS findings being preliminary and not published to date. For LoRa, there is a good match between the obtained results and the Norby flight test results (referring to Fig. 9 and Table 3 in [80]), which confirms the validity of the presented methodology and the framework proposed. However, the results in this chapter are more comprehensive than those presented in [80], as it explored the robustness of the LoRa modulation against the Doppler effect by considering parameters/settings that were not addressed in [80] (e.g., disabling LDRO), and by varying the configurations that were fixed (e.g., carrier frequency, orbital height) in [80].

Notably, LoRa DtS connectivity responds differently to each parameter as reported in publication [45]. As shown in Table 6, changes in the SF, payload length, and

Table 6. The impact of key parameters on the Doppler effect in LoRa DtS connectivity.

Parameter	Modulation	Static Doppler	Dynamic Doppler	Impact
SFs	LoRa	×	✓	High
Payload	LoRa	×	✓	Moderate
Bandwidth	LoRa/LR-FHSS	✓	✓	Very high
LDRO	LoRa	×	✓	Very high
Carrier frequency	LoRa/LR-FHSS	✓	✓	Very high
Orbital height	LoRa/LR-FHSS	✓	✓	Moderate

LDRO have no impact on the robustness against static Doppler effect. However, these parameters influence the vulnerability to dynamic Doppler effect. Conversely, variations in the channel bandwidth, carrier frequency, and satellite orbital height affect both static and dynamic Doppler effects. To ensure high reliability, one should carefully select these key parameters, also considering the link budget aspects. For example, using larger bandwidths helps to counteract the Doppler effect but increases noise and interference, negatively impacting the link budget and scalability.

Like LoRa, LR-FHSS is highly sensitive to the carrier frequency as illustrated in Fig. 14. The data rate, code rate, and header replica increase the LR-FHSS time-on-air, making the transmission experience more Doppler effect. The preliminary observations suggest that changing the data rate, code rate, and header replica do not affect the performance when configured to F_C = 868 MHz and 2.1 GHz, H = 560 km with a PHY payload of $P_L = 55$ bytes. However, a more thorough analysis is required to verify this claim for different settings.

4.6 Summary and discussion

This chapter investigates the impact of the Doppler effect on LoRa and LR-FHSS DtS performance. The results show key communication and orbital parameters' pros, cons, and trade-offs. Static and dynamic Doppler effects can disrupt the communication link, resulting in packet losses. The former is particularly harmful at low elevation angles. At the same time, the latter has a greater impact at high elevation angles when the satellite is closer to the end device, creating a hole in the middle of the satellite footprint, thus significantly reducing the effective coverage area. In both cases, the Doppler effect lowers the useful connection time. Consequently, even if a satellite is visible, the end devices might not be able to communicate due to the Doppler effect.

The reported results and analysis provide insights for selecting suitable parameters and settings to mitigate the Doppler effect in the DtS link. The presented results benefit researchers in academia and practitioners in the industry by helping them understand the LoRa and LR-FHSS Doppler limits for LEO satellites. For example, it can give an idea for selecting a suitable set of communication parameters, e.g., frequency band, channel bandwidth, Data rate for a given satellite orbital height, or vice versa. To make a fair comparison with the work in [80], this work considered the specifications for LoRa transceivers SX1276/77/78/79. It is worth noting that immunity to the Doppler effect also heavily relies on the designers' choices at the circuit level, and system performance can be enhanced through improvements in electronic design. For the LR-FHSS study, this work considers the specifications of LR-FHSS first transceiver LR1120 model. However, it is noteworthy that no operational satellite is known to use Semtech's latest transceivers. Consequently, comparing the reported LR-FHSS results against actual flight tests is barely feasible. In this work, we assume an ideal satellite pass, where the satellite directly passes over the end device. However, in actual scenario, satellite pass may not always reach 90° elevation angle. We consider LoRaWAN DtS Doppler effect analysis for different scenario using real-world satellites trajectories as a direction for future research. We also consider cellular NTN Doppler effect analysis as an interesting research direction. To solve the Doppler effect challenge in cellular NTN, 3GPP recommends the end device should support global navigation satellite system (GNSS) to determine its location and pre-compensate the frequency offset. For service link, one proposed solution under discussion involves the 5G new radio NTN UE should use its position and satellite ephemeris information in RRC idle and RRC inactive modes for frequency offset pre-compensation. Concerning the downlink, satellite base stations can effectively pre-compensate for Doppler shift by using the beam-specific common Doppler shift values.

5 LoRaWAN direct-to-satellite communications: link-level aspects

This chapter is based on the following publications [41, 43, 44] contributing to this thesis, offering more in-depth insight into the feasibility of LoRa and LR-FHSS DtS by using the *connection, capture* and *success probability* models outlined in **Chapter 3** Section 3.2. LR-FHSS was a brand new technology and was in the development phase, at the time of publication [43, 44]. Neither an LR-FHSS product nor any receiver sensitivity information was publicly available. Therefore, the publications [43, 44] only focus on LR-FHSS network scalability leveraging the proposed analytical and simulation models. However, after these publications, the LR1120 model featuring LR-FHSS was released, and datasheets reveal further information on the receiver sensitivity [63, 86]. To align well with the LoRa analysis reported in this chapter coming from publication [41], the LR-FHSS *connection probability* results illustrated in Fig. 22 are specifically generated for this thesis and are not published anywhere else. Both LoRa and LR-FHSS demonstrate the feasibility of such a system and illustrate some of the relevant trade-offs between the network configurations and communication performance. The results demonstrate the effects of different parameters on the connectivity performance. To compare the LoRa and LR-FHSS scalability, this chapter considers an illustrative use case scenario, situational awareness for ships. The network configurations use real-life positions of ships and satellites and traffic patterns. The obtained analytical results illustrate that LR-FHSS has a better capacity and outperformed LoRa.

5.1 LoRa

5.1.1 Analytical and simulation models

To evaluate the LoRa DtS performance, the simulator follows the link-level model outlined in Section 3.3. Specifically, it uses (15), (16), and (17) to calculate the *success, connection*, and *capture probability*, respectively. LoRa DtS simulators consider how shadowing, propagation, the capture effect, and fading affect communications performance. Since LoRa uses Aloha-like medium access control, the analytical average success probability of packet delivery can be calculated using the multi-frequency-channel unslotted Aloha model as

$$P_{ALOHA} = \exp\left(-\alpha_t \alpha_f \lambda_{tf}\right), \tag{23}$$

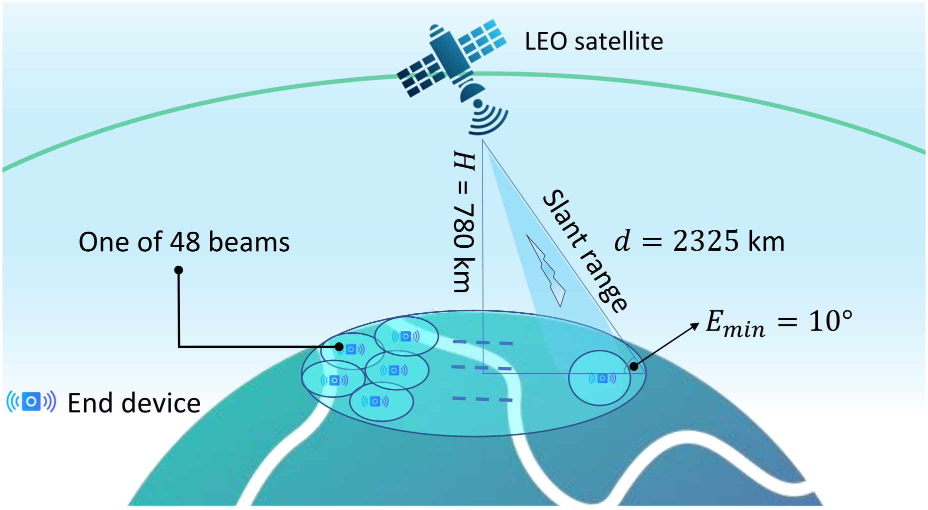

Fig. 15. Simulated scenario and key notations (Modified from Paper [41]).

where λ_{tf} is the traffic load, $\alpha_t = 2$ and $\alpha_f = 1$ (refer to [110] for details). Unlike the simulations model in Section 3.3, the analytic model P_{ALOHA} does not account for the shadowing, propagation, capture effect, Rician, or Rayleigh fading.

5.1.2 Network configuration

For LoRa modulation, underlying the LoRaWAN protocol, the SF is one of the key elements of the network configurations [76]. Higher SFs improve the gateway's ability to correctly demodulate a radio packet in the presence of noise [77]. At the same time, an increase in SFs almost doubles the on-air time for sending the same payload, thus increasing the number of collisions [78, 79]. Therefore, for the numerical results in this thesis, the two extreme SF settings – SF7 and SF12, and one mid-range configuration SF10, were selected.

Studies were conducted as part of this research using a specially developed MATLAB-based Monte Carlo simulator to obtain a more in-depth insight into the feasibility and potential trade-offs associated with LoRa DtS connectivity. The network scenario is illustrated in Fig. 15, and the key parameters of the system model (specifically (15), (16) and (17)) are summarized in Table 7. The simulation's key considerations and assumptions were as follows:

- As illustrated in Fig. 15, we assume an ideal satellite pass, where the satellite directly passes over the end device and elevation angle reaches 90°.

Table 7. System Model's Assumptions and Monte Carlo Simulation Parameters.

Parameters	Values/Requirements
Carrier frequency (F_C)	868 MHz
Bandwidth (B)	125 kHz
Channels	8
Transmit power (P_{tx})	14 dBm
End device antenna gain (G_t)	2.15 dBi
Gateway antenna gain (G_r)	22.6 dBi
Pathloss exponent (η)	2
Power threshold (δ)	6 dB
End device in a satellite coverage ($\bar{N}$)	100k, 250k, 500k
Spreading factor (SF)	7, 10, 12
MAC payload	9 bytes
Report time (R_p)	900 s
Elevation angles (E)	$10^\circ \leq E \leq 90^\circ$
Rician Factor (K)	$1.24 \leq K \leq 25.11$
Orbital height (H)	780 km

- The network considers LoRaWAN class A end devices equipped with omnidirectional half-wavelength dipole antennas with a gain of G_t = 2.15 dBi. All end devices were deployed under the open sky on the Earth surface, therefore, communication follows free space path loss model as in (13).
- This work envisions a LoRaWAN gateway deployed on a LEO satellite, which has the orbit height and characteristics (e.g., the feasible elevation angles) similar to that of the Iridium system. Specifically, each satellite is equipped with directive antennas which cover an area of 15,299,900 km^2 with 48 beams, while the area covered by a single beam increases towards the edge of the footprint [38].
- The antenna gain for each beam equals G_r = 22.6 dBi, and the signals of the end device served by the different beams do not interfere with each other.
- Importantly, the simulations also account for the time-varying channel characteristics due to satellite mobility by considering the dynamic Rician Factor (K) as in [111].
- The network considers that the physical and link-layer procedures are similar to the LoRaWAN protocol. The system operates in the EU 868 MHz ISM band (using eight duty-cycle-limited channels with a bandwidth of 125 kHz).

– It is assumed that the satellite employs an advanced mechanism to compensate for the Doppler shift; hence, the impact of the Doppler effect is not accounted for in the current analysis.
– No adaptive data rate is employed, and all end devices use a fixed SF (varied from one experiment to another) and transmit their signals with a transmit power of P_{tx} = 14 dBm.
– The simulation focuses specifically on the uplink transmissions, assuming no downlink. Therefore, uplink-downlink interference or the potential effect of the half-duplex operation of a LoRaWAN gateway are not relevant.
– End devices are uniformly distributed in the satellite coverage area and transmit their packets randomly with an average reporting period R_p of 15 minutes.

5.1.3 Numerical results

The numerical results obtained from our developed MATLAB-based Monte Carlo simulator focus on investigating two key aspects: (i) the feasibility and (ii) the scalability of LoRa DtS communication. The probability of a successful packet reception by a LoRaWAN gateway, denoted as *success probability (P_S)*, is composed of these two components. The former, denoted the *connection probability* (P_{SNR}), represents the probability of a received signal SNR exceeding the SF-specific LoRa demodulation threshold (D_{SNR}), allowing correct packet demodulation. The latter, *capture probability* expressed as P_{SIR}, accounts for the interference due to the transmission of the other LoRaWAN end devices. P_{SIR} accounts for the presence of the capture effect, i.e., the gateway successfully decodes a packet under co-SF interference, which is at least 6 dB weaker [76]. Fig. 16 shows the two components (i.e., P_{SNR} and P_{SIR}) of the success probability independently for the different number of end devices, configured with the minimum and the maximum SF (i.e., SF7 and SF12). The simulations also account for the influence of satellite mobility that rapidly changes the channel characteristics, elevation angle, and distance from the end device to the satellite. Fig. 17 reveals the *success probability* (P_S) as a function of the distance towards the satellite for SF7, SF10, and SF12.

Connection probability

Given the high orbital speed of the satellite (i.e., 7.44 km/s) and the elevation angle ranging ($10° \leq E \leq 90°$) results in the distance variation (2,325 km $\geq d \geq$ 780 km) between an end device and a satellite. The P_{SNR} curves in Fig. 16 reveal that even

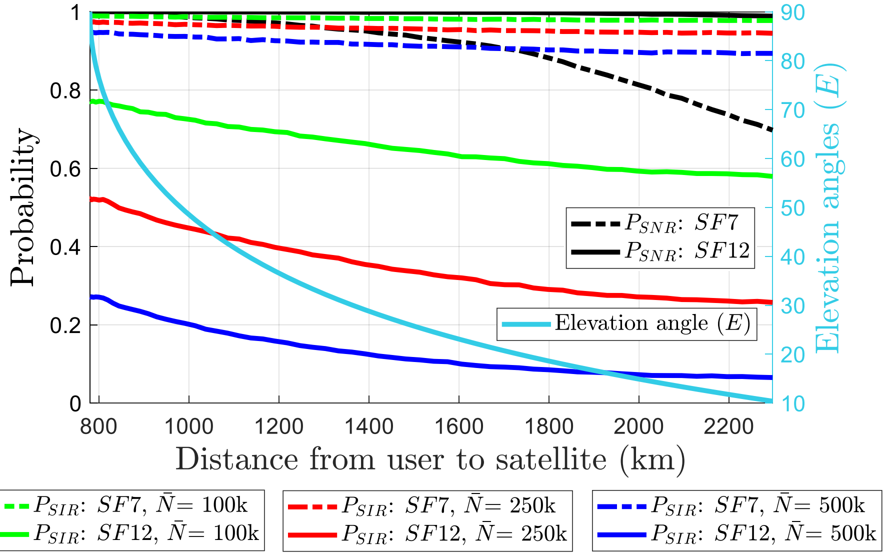

Fig. 16. P_{SNR} **- the probability of the signal-to-noise ratio (SNR) at the gateway exceeding an SF-specific LoRa demodulation threshold, and** P_{SIR} **- the probability of mitigating the co-SF interference as a function of the distance between an end device and the satellite for different SF configurations and end device densities. The right y-axis illustrates the elevation angle as a function of distance from a terrestrial end device to a satellite (Reprinted with permission from [41] ©2021, IEEE).**

when operating with SF7, a signal from the end device can reach the satellite with a probability exceeding 90% when the distance to it is below 1,700 km. However, this probability drops to less than 0.69 at the maximum distance considered (i.e., 2,325 km, which corresponds to a 10° elevation angle and the worst link budget case scenario). With SF12, the P_{SNR} stands steady at 100% until the end device to satellite distance reaches almost 2,100 km, and after that, it declines to 0.98 when the distance touches the coverage border of 2,325 km.

Capture probability

In Fig. 16, the P_{SIR} is affected by the two trends. First, the increase of an area served by a single beam increases the average number of the end devices under the uniform end device distribution implication, causing a slight decrease of P_{SIR} with the distance increase between a satellite and an end device. Specifically, for 500,000 end devices (denoted 500k in the chart) for SF7, with the increase of the distance from the minimum to the maximum, the P_{SIR} drops from 0.95 to about 0.9, while for SF12, the decline is

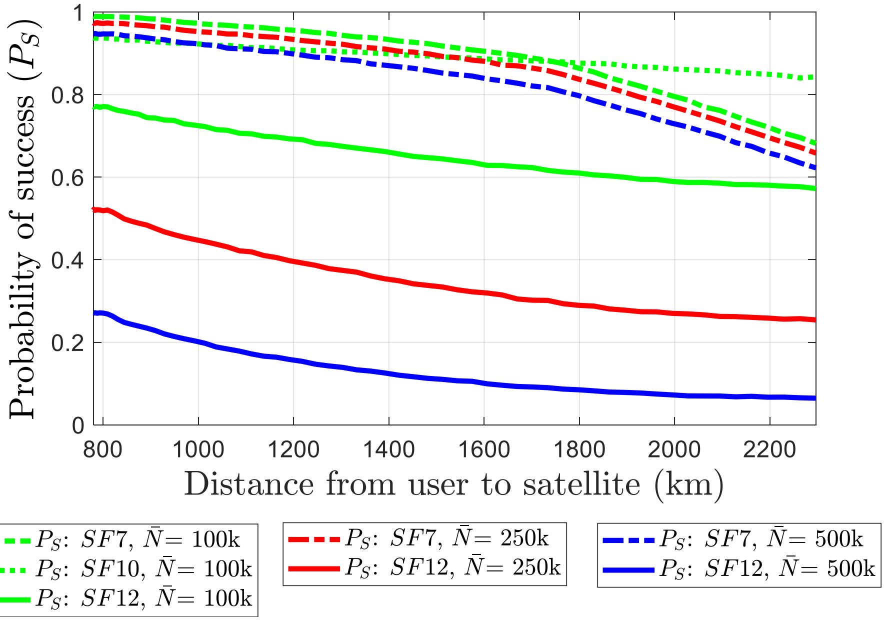

Fig. 17. The joint *success probability* (P_S) as a function of the end device's distance to the satellite for different SF configurations and end device densities. SF10 illustrates the performance of an SF between the minimum and the maximum ones (Reprinted with permission from [41] ©2021, IEEE).

from 0.27 to 0.08. Second, owing to the rapid increase of the on-air time (1.5 to two-fold with each next SF), with the increase of the SF, the P_{SIR} decreases with an increase in the distance between an end device and a satellite. For example, for a 100,000 end devices at 1,000 km distance, the P_{SIR} for SF7 is about 0.97 and drops below 0.72 for SF12.

Overall success probability

Both these trends merge in terms of their overall *success probability* (P_S), which is depicted for SF7, SF10, and SF12 and different end device densities in Fig. 17. The results clearly show the optimal SF's existence depending on the distance between a satellite and an end device, which is also affected by the network density. As can be seen, in the case of 100,000 active end devices, SF7 achieves the best performance for end devices located within 1,700 km from the satellite, while SF10 works better for distances exceeding 1,700 km.

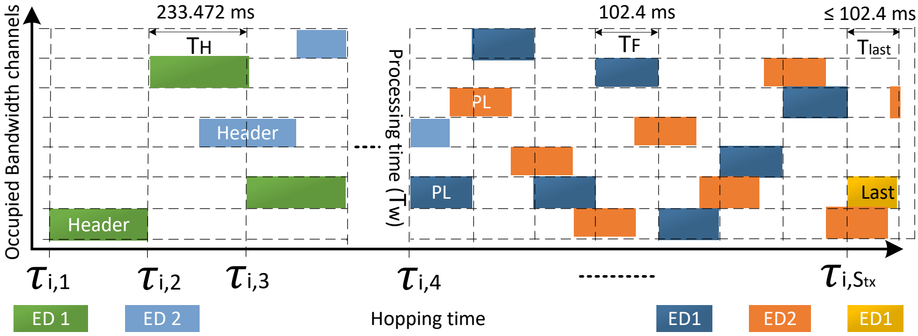

Fig. 18. Simultaneous transmission of two end-devices following the LR-FHSS scheme. This illustrative example considers a typical LR-FHSS transmission scenario where the packet elements of two end devices are not aligned in time. This illustration mainly shows the timestamps of the packet elements of the first end device, named ED 1.

5.2 LR-FHSS

To the best of the author's knowledge, this work is the first one to propose analytical and simulation models specifically for the LR-FHSS scalability analysis.

5.2.1 Analytical and simulation models

The LoRaWAN gateway can successfully receive and decode the LR-FHSS packet if the following two conditions are satisfied [109]:

- first, at least one of the N_H header replicas is successfully received
- second, the number of received data fragments is more than the pre-defined reception threshold (γ). In other words, if more than $\frac{1}{3}$ (or $\frac{2}{3}$) of the physical payload fragments are received and the first condition is met, the payload reception will be successful.

Following these conditions, the LR-FHSS analytical model examines the scalability without including the capture effect. Therefore, following the system model in Section 3.2, the simulator (system diagram illustrated in Fig. 20) is designed to take into account the impact of shadowing, radio propagation, capture effect, as well as fading on communication performance, providing more realistic results that better reflect the complexities of the communication environment.

Analytical

Let $\overline{N}$ be the total number of end devices, and let S_{tx} denote the total elements within an LR-FHSS packet, which comprises the sum of the number of headers N_H and payload fragments N_F. Each end device randomly generates $Q = 4$ uplink packets during an hour ($D = 3600$ s) and broadcasts them to LEO satellites. Therefore, $n = \overline{N} \times Q \times S_{tx}$ is the packet element that arrives in interval $(0;D)$ resulting in the average arrival rate $\mu = \frac{\overline{N}QS_{tx}}{D}$. Specifically, the average arrival rate for headers, payload fragments, and last fragments is represented by $\mu_H = \frac{\overline{N}QN_H}{D}$, $\mu_F = \frac{\overline{N}Q(S_{tx}-N_H-1)}{D}$, and $\mu_L = \frac{Q\overline{N}}{D}$, respectively. Let t_1 denote the starting time of the first packet and the timestamps of the subsequent packets be given by $t_{i+1} = t_i + \sum_{i=1}^{n-1} A(i)$, where $A(i) = t_{i+1} - t_i$ is the interarrival time of the two subsequent packets. As illustrated in Fig. 18, during an LR-FHSS packet, an end device changes the OBW frequency channels multiple times. We denote these moments $\tau_{i,j} = \{\tau_{i,1}, \tau_{i,2}, \ldots, \tau_{i,S_{tx}}\}$, where j denotes the hop within a packet, $j = 1,2,3\ldots,S_{tx}$. The timestamp of each hop is thus given by:

$$\tau_{i,j} = \begin{cases} t_i + (j-1)T_H & j \leq N_H, \\ t_i + N_H T_H + T_W + (j - N_H - 1)T_F & N_H + 1 \leq j \leq S_{tx}. \end{cases} \tag{24}$$

Since LR-FHSS uses an Aloha-like channel access protocol, if two or more packet elements collide, the reception of the colliding elements on the gateway can fail. Note that LR-FHSS applies frequency hopping, and the end device splits data into S_{tx} elements comprising headers and data fragments which have different transmission duration denoted as T_H, T_F, and $T_{F_{last}}$. Therefore, to accurately model this, we present a collision model for the LR-FHSS, which separately accounts for the number of colliding packet elements for transmitting a header, data fragment, and the last fragment. The vulnerable times for LR-FHSS are illustrated in Fig. 19. Thus, the average number of packet elements arrivals during a target header's vulnerable interval $(\tau_{i,j} - T_H; \tau_{i,j} + T_H)$, for $j = 1,\ldots,N_H$ is defined as

$$A_H = \mu_H 2T_H + \mu_F (T_H + T_F) + \mu_L \left(T_H + T_{F_{last}}\right), \tag{25}$$

where $T_{F_{last}}$ is the duration of the last fragment. Let T_{PHY} be the on-air time required to transfer payload data fragments (S_{tx} - N_H) and the duration of the last fragment be $T_{F_{last}} = T_{PHY} \pmod{T_F}$ which can differ from T_F. The average number of uplink packet elements transmitted in the interval $(\tau_{i,j} - T_F; \tau_{i,j} + T_F)$, for $j = N_H + 1,\ldots,S_{tx} - 1$ is thus given by

$$A_F = \mu_F 2T_F + \mu_H (T_H + T_F) + \mu_L \left(T_F + T_{F_{last}}\right). \tag{26}$$

Similarly, A_L, which denotes the average number of packet elements transmitted during the last fragment interval, is

$$A_L = \mu_L 2T_{F_{last}} + \mu_H \left(T_H + T_{F_{last}}\right) + \mu_F \left(T_F + T_{F_{last}}\right). \tag{27}$$

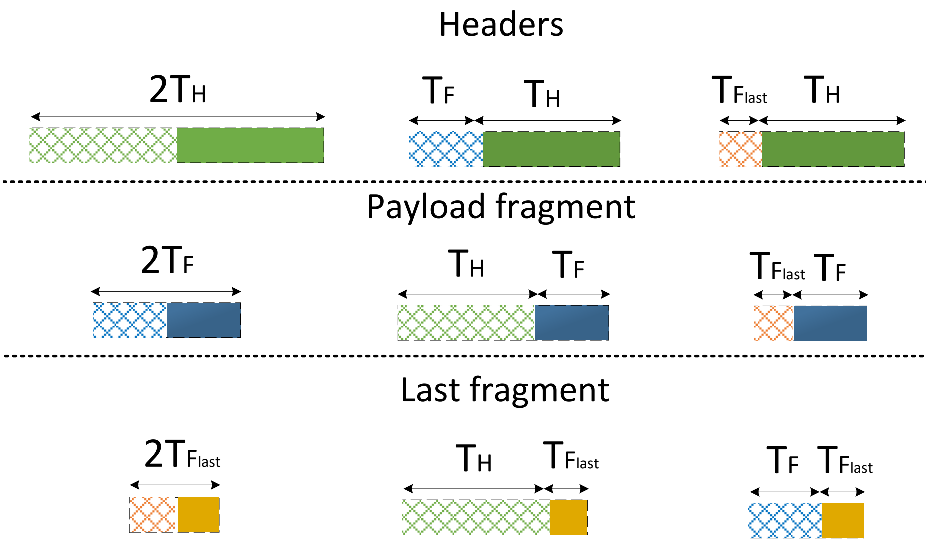

Fig. 19. Vulnerable times for LR-FHSS scheme (Reprinted [adapted] under CC BY 4.0 license from [43] ©2022 Authors).

Let us focus on an end device and investigate the uplink performance under the co-channel interference caused by simultaneous transmissions. The overall average success probability is composed of two components as

$$P_A = P_H(N_H)P_F(\gamma), \tag{28}$$

where the $P_H(N_H)$ represents the probability of successfully receiving at least one of N_H transmitted header replicas [4], thus

$$P_H(N_H) = 1 - \left(1 - \left(\frac{C-1}{C}\right)^{A_H-1}\right)^{N_H}, \tag{29}$$

where $C = 280$ denotes the number of non-overlapping OBW frequency channels for DR8/DR9 and A_H is given by (25). The $P_F(\gamma)$, denotes the probability of correctly decoding more than γ broadcasted payload fragments as

$$P_F(\gamma) = \Pr[F_{rx} \geq \gamma] = 1 - \sum_{k=0}^{\gamma-1} \Pr[F_{rx} = k], \tag{30}$$

$$\Pr[F_{rx} = k] = \binom{F_{tx}}{k} p_F^k (1-p_F)^{F_{tx}-k}, \tag{31}$$

where F_{tx} denotes the number of transmitted physical payload fragments, F_{rx} is the number of received fragments. Note that $T_{F_{last}}$ can differ from T_F, which requires

[4] Notably, this model only works for higher numbers of end devices when $A_H \geq 1$ and $A_F \geq 1$.

determining the average success probability of a single data fragment separately. Overall, p_F is the average success probability[5] of a single data fragment, and it is given as

$$p_F = \frac{(F_{tx}-1)\left(\frac{C-1}{C}\right)^{A_F-1} + \left(\frac{C-1}{C}\right)^{A_L-1}}{F_{tx}}. \tag{32}$$

Simulator model

To validate the analytic models and enable more complex scenarios, which can be hard to approach analytically, a MATLAB-based Monte Carlo simulation model for LR-FHSS has been developed as a part of this thesis (available, along with further details about its design and operation, from GitHub [49]). The structural diagram and sequence of the simulator's operation are illustrated in Fig. 20.

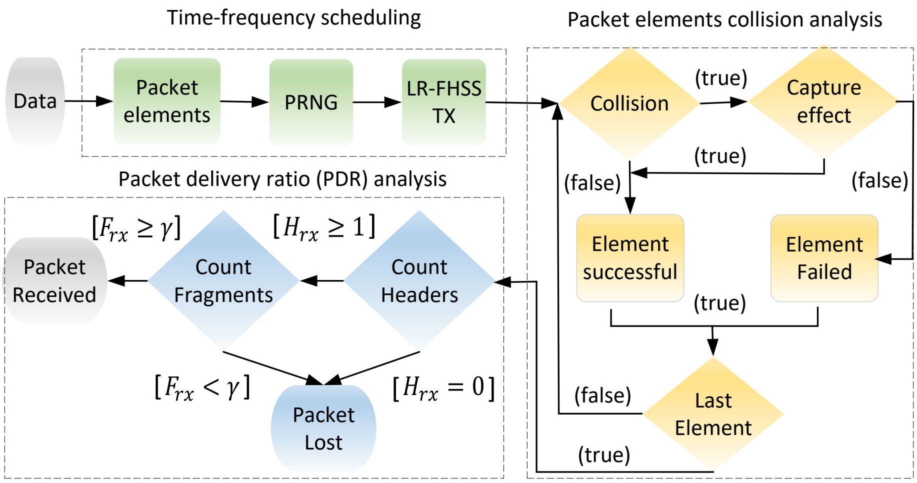

Fig. 20. System diagram of LR-FHSS simulator (Reprinted [adapted] under CC BY 4.0 license from [43] ©2022 Authors).

Like the LoRa simulator, the LR-FHSS simulator accounts for the satellite's mobility, rapidly changing the distance between the satellite gateway and the terrestrial end devices. The rapid variation in elevation angle results in fluctuations of the channel characteristics. To reflect this fact in the model, the simulator accounts for the temporal change of

[5]To account for the difference in T_F and $T_{F_{last}}$ duration, we calculate the average overall success probability (p_F) of a single data fragment which takes the average of the probabilities of the first $F_{tx}-1$ payload fragments and the last fragment.

the Rician fading effect. A collision occurs when two or more end devices transmit simultaneously on the same OBW channel. The capture effect, i.e., the possibility of a LoRaWAN gateway to receive the strongest packet element under interference from weaker signals, is accounted for through the *capture probability* by (17). Notably, LR-FHSS is brand new technology, and it requires empirical measurements to find capture effect power threshold value. In this study, we assume that LR-FHSS capture effect power threshold is equal to δ = 6 dB same as LoRa modulation [76]. The probability of the correct reception of a full element needs to meet two conditions: (i) the successful reception of at least one of the N_H transmitted header replicas, and (ii) successfully receiving more than γ transmitted payload fragments.

5.2.2 Network configurations

The script code for the LR-FHSS analytical and simulation model is available on the author's GitHub repository [49]. Table 8 lists the key parameters for generating analytical and simulation results. The network configurations are as follows:

- A LoRaWAN gateway is deployed on an LEO satellite with orbital characteristics similar to Iridium satellites. The orbital parameters are shown in Table 8, and Section 2.2.1 discusses Iridium satellites and the key orbital characteristics.
- A single gateway serves $\overline{N}$ = 0-300k (in Fig. 21) and $\overline{N}$ = 50k (in Fig. 22) end devices, unless stated otherwise, which are uniformly distributed within a satellite's footprint. Additionally, we assume that satellite creates a single spot beam.
- Each end device generates Q = 4 uplink packets at random times during an hour (D = 3600 s).
- The end devices have G_t = 2.15 dBi of antenna gain and transmit their signals with a transmit power of P_{tx} = 14 dBm. The gateway at the satellite has a gain of G_r = 22.6 dBi.
- The network considers only the uplink, i.e, end device to satellite communications.
- The carrier frequency (F_C), transmit power (P_{tx}), antenna gains, path loss exponent (η), capture effect power threshold (δ), satellite orbital height (H), elevation angles (E), and time-varying Rician Factor (K) are similar to the LoRa DtS configuration as in Table 7.

Table 8. Key Model Parameters.

Parameters	Values/Requirements
OCW Channel	1
OCW Bandwidth (B)	137 kHz
DR8/DR9 OBW Channels (C)	280
OBW minimum separation	3.9 kHz
Header replicas (N_H)	DR8 = 3, DR9 = 2
Coding rate (CR)	DR8 = $\frac{1}{3}$, DR9 = $\frac{2}{3}$
Header replica duration (T_H)	233 ms
Fragment duration (T_F)	50 ms
Receiver Sensitivity	-137 dBm
End devices ($\overline{N}$)	0-300k, 50k
PHY payload	10 bytes
Report period (R_p)	900 s
Elevation angles (E)	$10^\circ \leq E \leq 90^\circ$
Orbital height (H)	780 km
Orbital inclination	86.4°

5.2.3 Numerical results

Fig. 21 depicts the analytical results for average success probability for the packet delivery P_A using (28), as well as that for headers $P_H(N_H)$ (29) and the necessary number of data fragments $P_F(\gamma)$ by (30) as a function of the number of end devices $\overline{N}$ obtained analytically. Fig. 22 shows simulation results. From the presented results in Fig. 21, one can see that when $\overline{N}$ is below 150k, the P_A for end devices operating with DR8 is higher than that using DR9. However, for denser networks, DR9 slightly outperforms DR8.

Notice that the P_A for DR8 is dominated by $P_H(N_H)$, while $P_F(\gamma)$ degrades much more slowly than $P_H(N_H)$. For DR9, featuring fewer header repetitions but a higher coding rate for payload fragments, the $P_H(N_H)$ is higher than that for DR8. The $P_F(\gamma)$, for DR9, however, stays below that for DR8 owing to a higher decoding threshold (γ). Specifically, the P_A for DR8 and DR9 is around 74.35% and 68.22%, respectively, at $\overline{N}$ = 50k. Furthermore, the P_A of both data rates gradually declines to 8.11% when the $\overline{N}$ reaches 150k. For the maximum number of end devices considered, the P_A drops to 0.02% for both data rates.

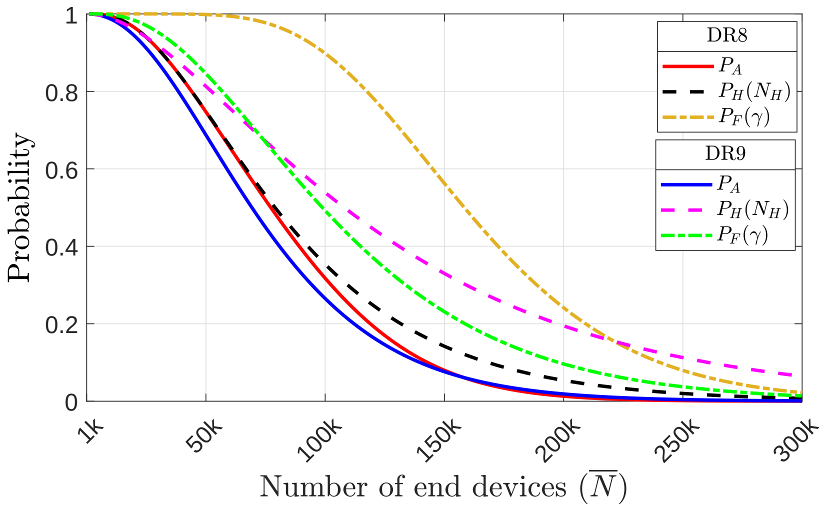

Fig. 21. The average probability of packet delivery P_A and its components: header success probability ($P_H(N_H)$) and probability of sufficient payload fragment reception exceeding the threshold $P_F(\gamma)$ implying $Q = 4$ (Reprinted [adapted] under CC BY 4.0 license from [43] ©2022 Authors).

Connection probability

Note that each point on the simulation results charts averages 10^5 (i.e., 100k) random realizations of the end device distributions and traffic patterns. The P_{SNR} results in Fig. 22 reveal that a LR-FHSS packet can successfully reach a LoRaWAN gateway deployed on a satellite at the maximum slant distance higher than 2,200 km with over 99% probability. This shows that LR-FHSS has a similar P_{SNR} as LoRa SF12 in Fig. 16. LoRa and LR-FHSS require high antenna gain at the satellite for such a high P_{SNR}. The current simulation setup considers G_r = 22.6 dBi.

Capture probability

In Fig. 22, P_A shows the analytical success probability without accounting for channel conditions and the capture effect as in (28). Looking at P_{SIR}, one can see that the capture effect boosted the average success probability. Moreover, since very limited information was available about the capture effect for LR-FHSS at the time of publication [43], we assume that to be demodulated correctly, the target signal needs to be at least δ = 6 dB stronger than the sum of the interfering ones, as in legacy LoRa [76]. The P_{SIR} curve

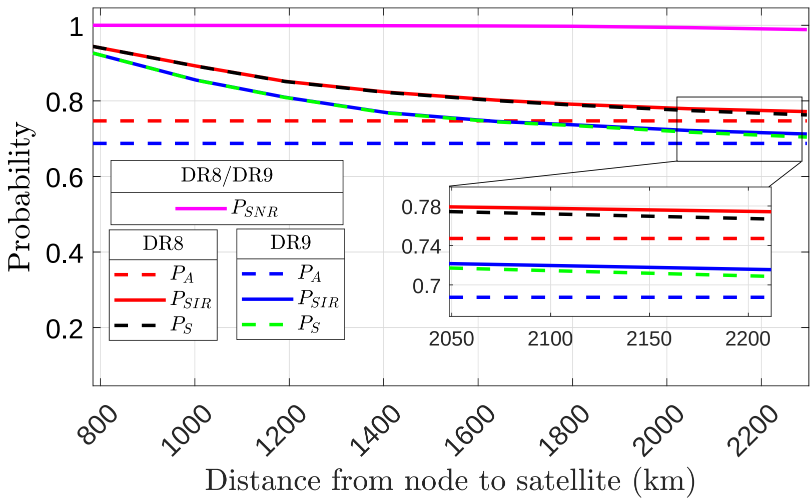

Fig. 22. The simulated average success probability P_S illustrating the product of P_{SNR} and P_{SIR} as a function of the distance from an end device to the satellite considering $\overline{N}$ =50 k and $Q = 4$, where P_A is the analytical average success probability calculated by (28) without accounting for the channel noise and capture effect. The simulated results P_{SIR} account for capture effect.

for DR8 shows that the gateway can successfully receive a packet with a probability exceeding 85.17% until the distance to a satellite reaches 1,200 km. However, this probability declines to 77.16% at the highest distance. With DR9, the P_{SIR} stays above 75% within 1,600 km from satellite and drops below 71.22% when the distance touches the coverage border.

Success probability

Fig. 22 illustrates the overall success probability as a function of the distance between a ground end device and the satellite for the case of $\overline{N}$ = 50k. Note that DR8 demonstrates the best performance, allowing a LoRaWAN end device packet to reach the satellite with P_S about 74.70%. With DR9, the P_S drops to 68.74% owing to the change in the code rate from $\frac{1}{3}$ to $\frac{2}{3}$.

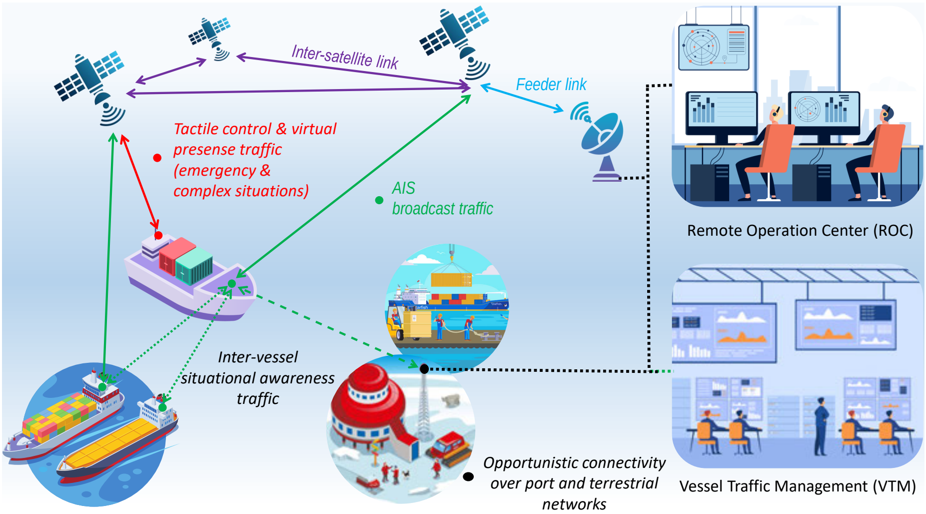

Fig. 23. Envisaged ship situational awareness communications architecture (Reprinted [adapted] with permission from [44] ©2022, IEEE).

5.3 LoRa and LR-FHSS comparison: an illustrative use case

Motivated by the progress with the DtS LPWAN mMTC networks, this section conceptualizes the LoRaWAN DtS communication use in the context of situational awareness for ships. The characteristics of the situational awareness data traffic (e.g., AIS) resemble the traffic of machines for which LPWAN mMTC have been developed [20, 21, 32]. This makes LPWAN mMTC DtS connectivity a suitable solution for transferring AIS data. We introduce a novel network architecture to facilitate the transmission of ship AIS data employing LoRa and LR-FHSS schemes using LEO satellites. In [44], we assess and compare the scalability of LoRa and LR-FHSS technologies using real-world ship and satellite location data, the network configuration follows LoRaWAN specifications. In the following sections, we discuss the proposed AIS communications architecture, operational scenario, network configuration parameters and the scalability results.

5.3.1 Situational awareness architecture for ships

Figure 23 illustrates the envisioned ship situational awareness connectivity architecture, where the traffic is divided into two main categories. The former comprises the situational awareness traffic (the AIS "heartbeat") for which DtS LPWAN mMTC networks are advocated. The latter, labeled in Fig. 23 as tactile control and virtual presence traffic, includes all the other data transfers (e.g., live streaming of sensor data to a remote operation center (ROC) or commands from the ROC to the ship) and should be carried via other means of connectivity (e.g., a broadband satellite or NTN channel; e.g., a very high frequency Data Exchange System (VDES) VDES or another technology). We assume that the latter traffic (i) is typically present only in an emergency case when the ship onboard intelligent system cannot handle the situation; and (ii) connects ship and the ROC. Meanwhile, the small-data awareness traffic is (i) transmitted continuously, and (ii) is relevant for the ROC, Vessel Traffic Management (VTM), and the other nearby ships.

Compared to conventional satellite-based AIS systems, the transfer of situational awareness data over LoRaWAN-like technology has following benefits:

- The LoRaWAN technologies do not apply any handovers between gateways. This enables multiple recipients (i.e., in space, at sea, or on the land) to receive the data. This allows for leveraging multi-connectivity in the uplink channel if multiple satellite gateways are above the horizon, enhancing the packet delivery probability. This thesis presents only selected results comparing LoRa and LR-FHSS; however, multi-connectivity results are reported in our paper [44].
- Unlike the conventional AIS, Self-Organized Time-Division Multiple Access (SOT-DMA), LoRaWAN DtS uses Aloha-like media access, which does not inquire about any connection establishment phase or waiting delays.

On the downside, the proposed connectivity architecture is more complex and uses the distribution of the two data traffic types between the two communication systems. However, the possibility of optimizing each of the systems for its dedicated traffic and distinguishing traffic with different priorities and quality-of-service requirements would, in our opinion, enable more efficiency in terms of performance and resource utilization operation overall.

5.3.2 Operation environment

It is worth recalling that the AIS system broadcasts a message every 2 to 360 seconds depending on the ship speed [98]. For example, a ship transmits an AIS message every 2 seconds when navigating at a speed higher than 23 knots, whereas the transmission period increases to 360 seconds when the ships is anchored. For our analysis, we account for the impact of the ship speed on the data traffic model. We have selected the Arctic region, which is very challenging for ships. To better understand the numbers, distribution, and traffic patterns of the ships in the Arctic, we have analyzed real-life

AIS data collected by the Arctic Data Center [112]. First, we divided all the AIS records into 10 minutes intervals and estimated (i) the number of ships, (ii) their location, and (iii) their activity. Our analysis shows that in the busiest interval - August 31, 2016, from 18:51:36 to 19:01:36 - as many as 832 ships were operational. The ships' locations and distribution during this period are illustrated in Fig. 24. Our analysis reveals that 39.3% of the ships were *en route* in the deep sea, followed by 25.96% in the internal waters. The territorial sea (i.e., area within 12 nautical miles from the coastline) contained 22.35% of active ships. The remaining 12.37% were anchored or static.

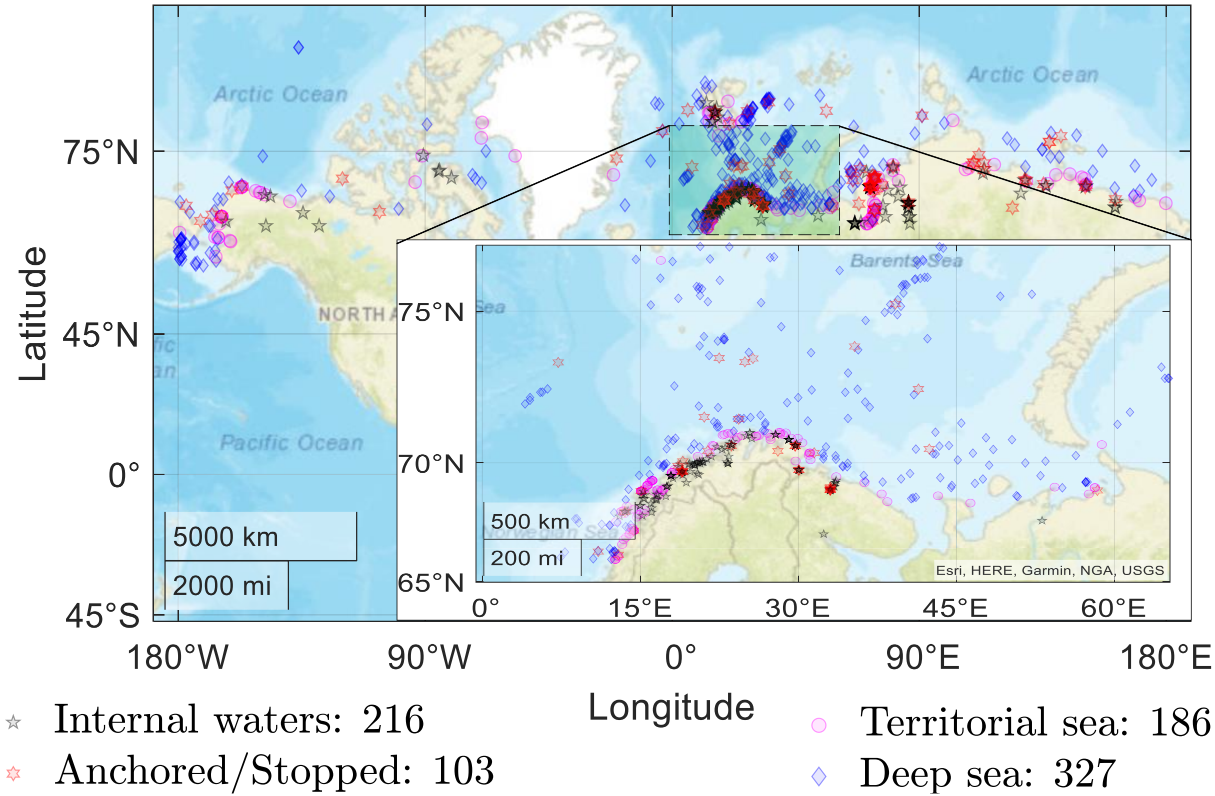

Fig. 24. Analysis of the ships' activity in the Arctic region during the most busy period (based on AIS data; 18:51:36 to 19:01:36 August 31, 2016) (Reprinted with permission from [44] ©2022, IEEE).

Table 9. Key network configuration parameters.

Parameters	Values/Requirements
LoRa	
Bandwidth (B)	125 kHz
Spreading factor (SF)	7, 10 or 12
Frequency Channels	16
LR-FHSS	
Header replica duration (T_H)	233.472 ms
Fragment duration (T_F)	102.4 ms
LR-FHSS OBW bandwidth	488 Hz
OBW minimum separation	3.9 kHz
DR8/DR9 OCW Bandwidth (B)	137 kHz
DR8/DR9 OBW Channels (C)	280
DR8/DR9 OBW Channels/end device	35
DR10/DR11 OCW Bandwidth (B)	336 kHz
DR10/DR11 OBW Channels (C)	688
DR10/DR11 OBW Channels/end device	86
Header replicas (N_H)	DR8/DR10 = 3, DR9/DR11 = 2
Code rate (CR)	DR8/DR10 = $\frac{1}{3}$, DR9/DR11 = $\frac{2}{3}$
Traffic model	
MAC payload	21 bytes
Report time (R_p)	2 s $\leq R_p \leq$30 s
Data transmissions	Unacknowledged
Traffic pattern	Periodic

5.3.3 Network configurations

Analytical models were used to determine the probability of successfully transferring the ship awareness data traffic over LoRaWAN-like networks employing both LoRa and LR-FHSS modulation-coding schemes to gain insight into the feasibility of the proposed architecture. We assume that a LoRaWAN gateway is onboard an LEO satellite. The key model parameters are listed in Table 9, and the key assumptions are as follows:

– Only one LoRaWAN end-device terminal is installed on top of each ship. The end devices are equipped with omnidirectional antennas with a gain of G_t = 2.15 dBi.

– We assume a LEO satellite orbits at an altitude of 1015 km (similar to the orbital height of Telesat [44]) which carry a single gateway which creates a single spot beam.
– We considered LoRa (i.e., DRs 0 to 5), and the LR-FHSS (DRs 8 to 11) which were introduced in 2020 [62, 88, 90].
– Following the conventional LoRaWAN configurations for the EU, we consider 16 frequency channels available for DRs 0-5, 280 OBW channels for DR8 and DR9, and 688 OBW channels for DR10 and DR11.
– The number and the position of the ships were modeled following the real-life situation during the busiest period as discussed in Section 5.3.2.
– Each active ship transmits a 21-byte AIS uplink packet with an average period of 2 s $\leq T \leq$ 30 s, and each anchored ship - with a period of 360 s.
– Since traffic is one-way and accounting for the limited downlink resources of satellites, no downlink traffic is assumed.
– The time-on-air ToA = 77.05, 452.6, 1810.32 milliseconds for DR5, DR2 and DR0, and the ToA = 1929.5, 1084.5 milliseconds for DR8/DR10 and DR9/DR11, respectively.
– Additionally, we assume that all the ships use the same modulation, either LoRa or LR-FHSS, and only the interference from the ships transmitting DtS awareness traffic within the satellite footprint is considered in this work.

When modeling the collisions, we assumed that for LoRa, any overlap in time and frequency causes packet loss and results are generated by (23), while for LR-FHSS modulation, a packet is received in case at least one header replica and a sufficient (the threshold depends on the data rates) number of payload data fragments are received as in (28).

5.3.4 Numerical results

The analysis focuses on the performance of both LoRaWAN modulations for a single satellite. Analyzing the position of the ships and the satellites' trajectories, there were, on average, 590 ships operating inside a single satellite's footprint. 529 ships were *en route*, and 61 were stationary. Considering this number of ships, the analytical probability of successful packet delivery for LoRa using P_{ALOHA} (23) and LR-FHSS using P_A (28) for AIS report periods was analyzed.

From Fig. 25 one can see that the DR selection directly affects the on-air time, coding rate and modulation, and strongly influences the average success probability. For the reporting period of 2 s, the probability for DR0, DR2, DR8, and DR9 stays below

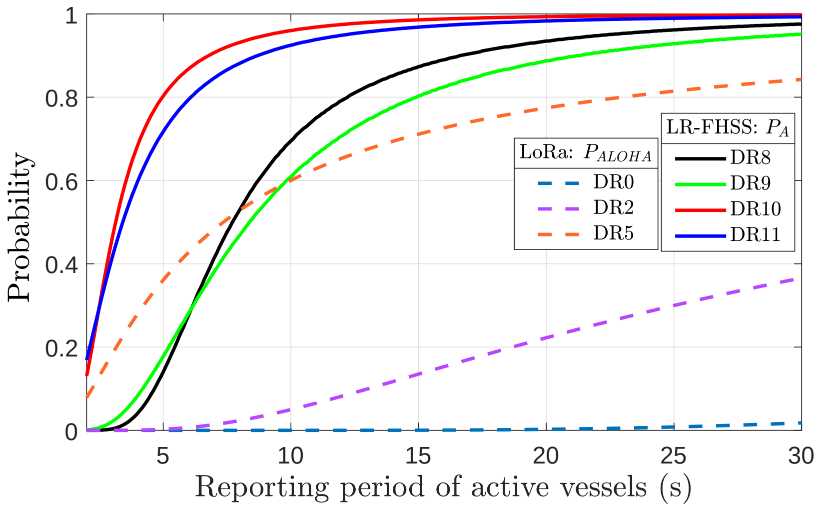

Fig. 25. The average analytical packet success probability (LoRa P_{ALOHA} (23) and LR-FHSS P_A (28)) as a function of the AIS reporting period for a single satellite (Reprinted [adapted] with permission from [44] ©2022, IEEE).

0.01, and DR5 achieves around 0.07. When using LoRa DR0, the performance remains close to zero for the whole range of the reporting periods 2 s $\leq T \leq$ 30 s. One can also see that DR8 and DR9 outperform DR5 when the reporting period exceeds 8 s and 10 s, respectively. When using DR2 and DR5, with a 30 s reporting period, the P_{ALOHA} is below 0.36 and 0.84, respectively.

Notably, the P_A curves for DR8 and DR9 show that the gateway can successfully receive a packet with a probability exceeding 0.88 for a reporting period higher than 20 s. However, DR10 and DR11 can perform similarly when R_p is as low as 8 s. Note that DR10 and DR11, featuring 688 channels for frequency hopping, demonstrate the best performance with P_A about 0.97 when R_p is 15 s, which further grows to over 0.99 when ships report every half minute. The standard deviation (std) fluctuates quite significantly; however, the standard deviation for LR-FHSS is generally lower than for LoRa. For example, for DR8, the standard deviation varies from 0.3788 to 0.0873 for 2 second and 30 second report periods, respectively. DR5 std is 0.2685 at the lowest and 0.3651 at the highest reporting period, respectively.

5.4 Summary and discussion

This chapter investigates the link budget and scalability of LoRa and LR-FHSS DtS connectivity. The presented results demonstrate the potential for a end device signal's to reach a satellite even when using the configurations typical for today's terrestrial LPWANs and reveals some interplay between the network settings and performance metrics. Specifically, to overcome the radio channel's attenuation due to the much longer communication range in direct connectivity, a LoRaWAN end device will likely have to use a higher transmit power and spreading factor more often. This can result in a higher average overall energy consumption of the end devices connected to a satellite. These results motivate further studies to take a deeper and more systematic look at LoRa DtS performance for specific application scenarios and study the new LoRa variant, LR-FHSS.

This chapter also comprises the results from one of the first publications focusing on the newly introduced LoRaWAN LR-FHSS modulation-coding scheme, which is particularly promising for DtS mMTC. To the best of our knowledge, we are the first to develop analytical and simulation models to examine the scalability of LR-FHSS. Our results show that LR-FHSS can support large-scale DtS networks. Notably, our analytical results reveal that the primary reason for packet loss is the loss of the headers. Our simulation model accounts for the capture effect which notably boosts performance.

Overall, our results show that the performance of LR-FHSS is higher than that of conventional LoRa modulation. This is primarily due to the hundreds of frequency channels, frequency hopping spread spectrum techniques, coding rates, and redundancy of physical headers employed in LR-FHSS. However, the technical information about LR-FHSS is limited today, we are not aware of any work that discusses the time-on-air, current consumption characteristics and battery lifetime of LR-FHSS. It is important to mention that the accurate time-on-air model is very important for calculating collisions and scalability analysis. Therefore, there's a clear need for further research to measure and investigate the LR-FHSS's time-on-air and power consumption. We hope this chapter will motivate future research, experimentation, and development of LR-FHSS solutions. We consider LoRa and LR-FHSS co-existence study for and terrestrial and non-terrestrial networks as a prospective research direction.

6 LR-FHSS current consumption and air-time modeling

The results presented in **Chapter 5** confirm that LR-FHSS is a promising technology for direct communication to LEO satellites. It is perfectly suited for use cases where long-range and low-power communication is required for many devices. The LR-FHSS end devices envisioned for DtS IoT will be primarily battery-powered. The primary aim of DtS IoT is to provide connectivity to machine applications, specifically in remote areas. Replacing batteries of the end devices installed in hard-to-reach areas presents significant challenges and expenses. For instance, replacing the end device battery on an offshore wind turbine's nacelle requires extensive labor. Therefore, it is crucial to investigate the current consumption characteristics and ToA of LR-FHSS technology. The ToA and current consumption models enable the estimation of the battery lifetime and facilitate network optimization to ensure a longer battery lifespan. An accurate ToA model is very important for collision modeling, scalability analysis and network optimization. However, no prior research has presented this newly introduced scheme's accurate ToA and current consumption models. This chapter, grounded in the paper [46], addresses this shortcoming through extensive measurements and the development of analytical models.

6.1 LR1120 development kit

The LR1120 is the first commercially available development kit featuring an LR-FHSS transceiver. This real transceiver allows us to get insight into the LR-FHSS operation, system modes, their duration, and associated current consumption. Therefore, in what follows, this section briefly introduces the LR1120 modem and respective development kit, which will be further used in the experimental campaign.

6.1.1 Power amplifiers

The LR1120 device includes a low-power amplifier (LPA) and high-power amplifier (HPA) to facilitate its sub-GHz operations. The selection between these amplifiers depends on the configured transmit power (P_{tx}). The LPA is primarily optimized for P_{tx} below +14 dBm, while it can also support +15 dBm. In contrast, the HPA is specifically designed for generating up to P_{tx} =+22 dBm [86].

6.1.2 System modes

Fig. 26 illustrates the LR1120 operational modes. The *power down* mode has the lowest power consumption since this mode stops all clocks and does not retain any data. Similarly, the *sleep* mode offers a low power consumption option. However, the *sleep* mode retains the configuration register values and stores the firmware data in random-access memory (RAM).

We briefly discuss the sequence of the operations that are relevant for this work. Upon *startup* (S_Startup), the *bootloader* performs firmware validation before transitioning to the *standby* state (S_STBY_RC), the default mode of LR1120. The *standby* modes, S_STBY_RC and S_STBY_XOSC, differ in their clock oscillator selection, with the former utilizing the internal resistance capacitance (RC) oscillator at 32 MHz. At the same time, the latter employs an external crystal clock, allowing faster transitions to other modes. To transmit a packet, the device leaves the *standby* mode and enters *frequency synthesis* (S_FS) mode to activate the Phase-Locked Loop and associated regulators.

The LR1120 user manual (see Figure 2-1 in [86]) does not present a *radio preparation* mode. However, the measurements carried out for this thesis indicate that the device enters a *radio preparation* (S_Radio_Prepare) state for around 100 milliseconds before *transmission* (S_TX) mode. Next, in the S_TX mode, the LR1120 transmits the LR-FHSS packet at the configured carrier frequency and DR using the relevant power amplifier to achieve the desired output power. After completing the transmission, the device enters a *radio off* (S_Radio_Off) mode, deactivating the power amplifier and regulators. It is worth noting that this mode is not documented in the LR1120 state diagram (see Figure 2-1 in [86]). Finally, the device reverts to the default *standby* mode (S_STBY_RC). However, in this thesis, the code used for testing is modified and specifically configures the device to enter the *sleep* (S_Sleep) mode and remain there until the next transmission.

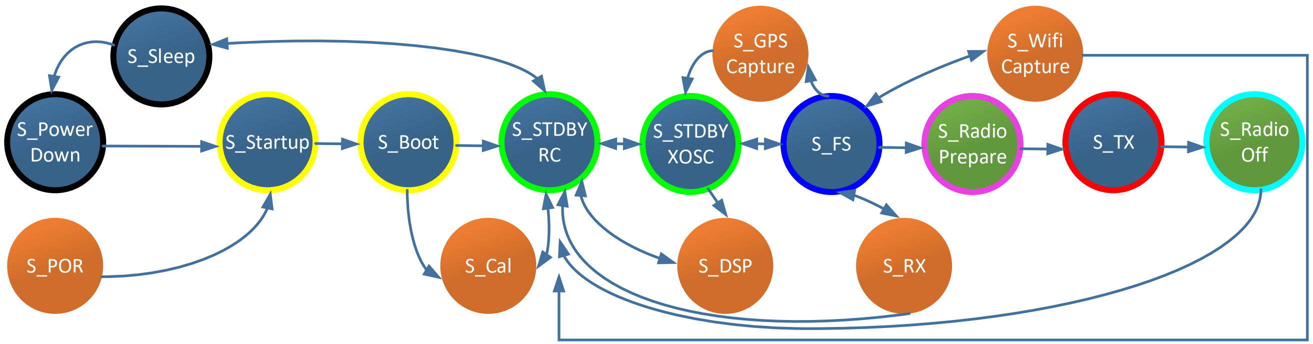

Fig. 26. LR1120 operational modes, where the states marked by green filled circles are not reported in the user manual [86]. These green states are identified from experimental measurements during this work and based on an analysis of the software code of the transceiver's firmware, while the orange ones are irrelevant for this work. Notably, color borders distinguish between the different states and build a relation with Fig. 30.

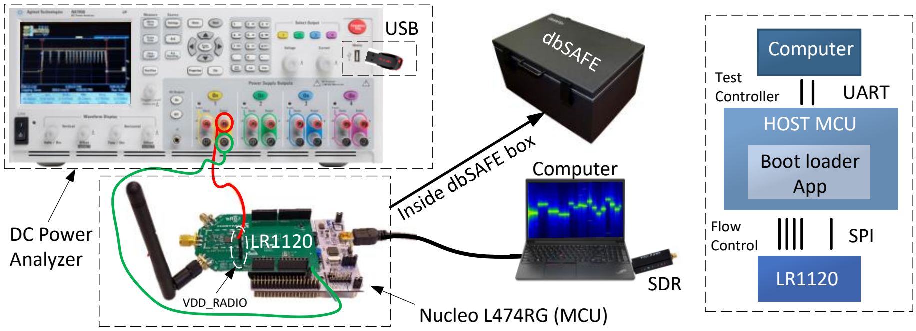

Fig. 27. The structural diagram of the experimental setup for current consumption measurements of LR-FHSS transmissions.

6.2 Experimental setup

6.2.1 Hardware

This work uses LR1120 development kits as a reference LR-FHSS transmitter for measurement [86]. Notably, the current consumption and ToA model developed in this chapter will remain valid for other LR-FHSS devices. However, different power amplifier configurations could impact the current consumption in *transmission* (S_TX) mode. Any such differences can be incorporated into our model through minor adjustments, which can be done later depending on the availability of LR-FHSS new device models.

Fig. 27 shows the structural diagram of the experimental setup. One can see that LR-FHSS-enabled LR1120 is further connected to the ST Microelectronic NUCLEO-L476RG, which serves as a host Microcontroller Unit (MCU). The software is installed on the host MCU responsible for programming the LR1120. MCU and LR1120 radio communication is based on a Serial Peripheral Interface (SPI) [113]. For measuring the current consumption, duration of each operation state, and ToA, we used the Agilent N6705B DC Power Analyzer. Specifically, the following steps were performed:

- To ensure accurate measurements and minimize energy consumption and fluctuations, the light-emitting diode (LED) (LD1) is removed from the MCU. Subsequently, LR1120 is mounted onto the MCU development board. A connection is established between the MCU and a computer to facilitate the installation of the LR-FHSS software and overall control over the experiment.
- Next, to monitor the current consumption of the LR-FHSS-enabled LR1120, the VDD_RADIO jumper is removed and the VDD_RADIO is directly connected to the positive output (red wire in Fig. 27) of a DC Power Analyzer. Simultaneously, the MCU and LR1120 radio ground (GND) are used as a common reference and

connected to the negative output (green wire in Fig. 27) of the DC Power Analyzer. A 3.3 V DC supply is used for the measurements, with a maximum current limit of 180 mA current and a sampling period of 20.48 microseconds (μs). The MCU was directly powered from a computer using a mini USB connector cable. This setup exclusively enables the current consumption and timing measurement of different LR-FHSS modes without considering the current consumption of the host MCU.
- In the third step, the testbed is placed inside a dbSAFE box to ensure RF isolation.
- Finally, a Nooelec RTL-Software Defined Radio (SDR) is used to observe and visualize the frequency spectrum of the LR-FHSS transmissions.

6.2.2 Software

The MCU was programmed using the LR11xx radio drivers published by Semtech on GitHub [114]. The Keil IDE is used to introduce changes and build the software, specifically implementing three modifications in the code:

- Firstly, the `LR1110_lr_fhss_ping.c` file disables the TX and RX LEDs of LR1120 to prevent measurement fluctuations and additional current consumption.
- Secondly, the radio is configured to transit into *sleep* mode after transmitting a packet, even though the default mode was standby mode. Specifically, we modify the `enter_standby_then_sleep_mode()` function in the `LR1110_lr_fhss_ping.c` file.
- Third, the `LR1110_lr_fhss_ping.c` file is updated to enable the following three measurement scenarios:
  - i) 10 bytes constant payload size and variable P_{tx} ranging from 0 to 22 dBm;
  - ii) constant P_{tx} 14 dBm and variable payload 10 to 65 bytes;
  - iii) repeating the measurements above for DR8 and DR9.

Lastly, we developed a MATLAB script (openly accessible on GitHub [53]) to process the collected data with the following functionalities:

i) to allow the identification of different transition states of LR-FHSS transmission,
ii) to calculate the duration and current consumption for each state and
iii) to carry out a total ToA calculation of the *transmission* (S_TX) mode.

6.3 Experimental results

A series of test measurements were initially conducted to ensure the accuracy and reliability of the hardware and software configuration. Fig. 28 depicts the LR-FHSS

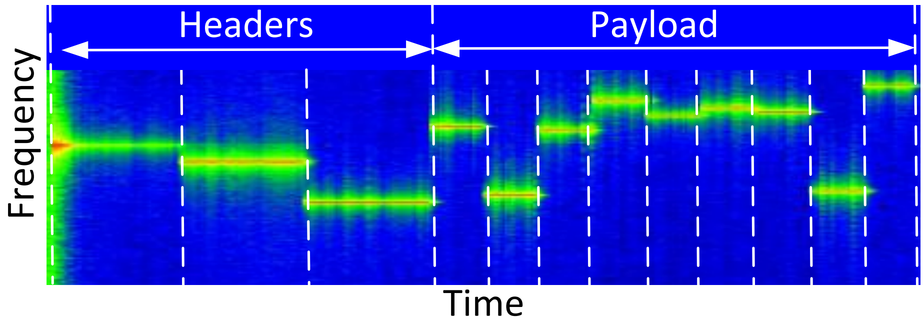

Fig. 28. The frequency spectrum of LR-FHSS illustrating intra-packet frequency hopping profile of a single LR-FHSS packet with a $L=$ 15-byte payload and DR8 featuring CR =$\frac{1}{3}$ and $N_H=3$.

packet spectrum captured by the CubicSDR software, visually representing the intra-packet frequency hopping. This validation step confirms the proper functioning and appropriateness of the implemented hardware and software setup.

Several measurements were performed to characterize the LR-FHSS average current consumption and ToA. To accomplish the former, twenty measurements were conducted under varying P_{tx} levels, ranging from 0 dBm to 22 dBm, specifically for DR8 and DR9. To develop a realistic ToA model, the measurements were carried out across various variable payload sizes, spanning from 10 to 65 bytes, for both LR-FHSS DRs, i.e., DR8 and DR9. This accounts for different CRs and header diversity configurations of the DRs.

Fig. 29 shows the current consumption for just one out of twenty experimental rounds. One can see that the current consumption increases significantly for P_{tx} exceeding 14 dBm when the power amplifier switches from LPA to HPA. Fig. 30 illustrates the current consumption profile of a single LR-FHSS transmission. The transmission undergoes different states, as mentioned in Section 6.1.2. Each state within the transmission process reveals distinct characteristics regarding the duration and associated current consumption. Table 10 summarizes these states, their duration, and the average current consumption computed over all 20 experiment runs.

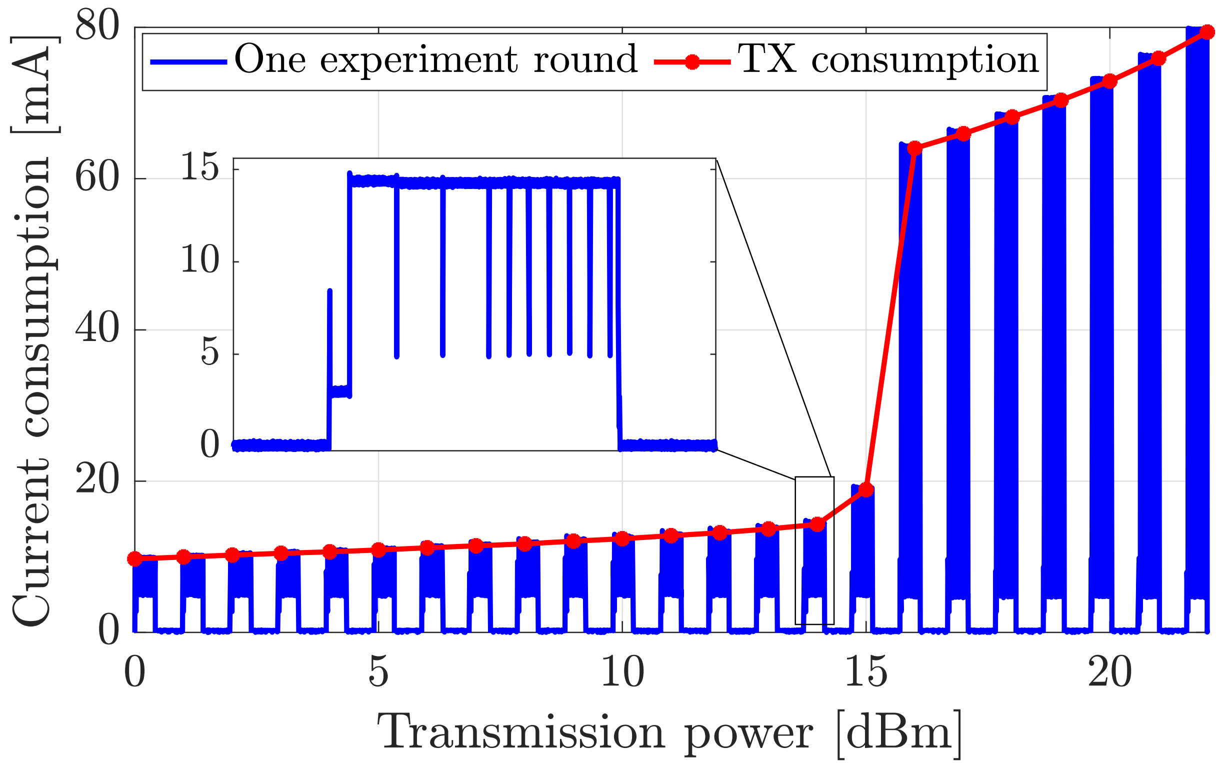

Fig. 29. The impact of variable transmit power on the LR-FHSS radio current consumption for one experimental round. We conducted twenty rounds of measurements, resulting in over 460 packet transmissions for each DR.

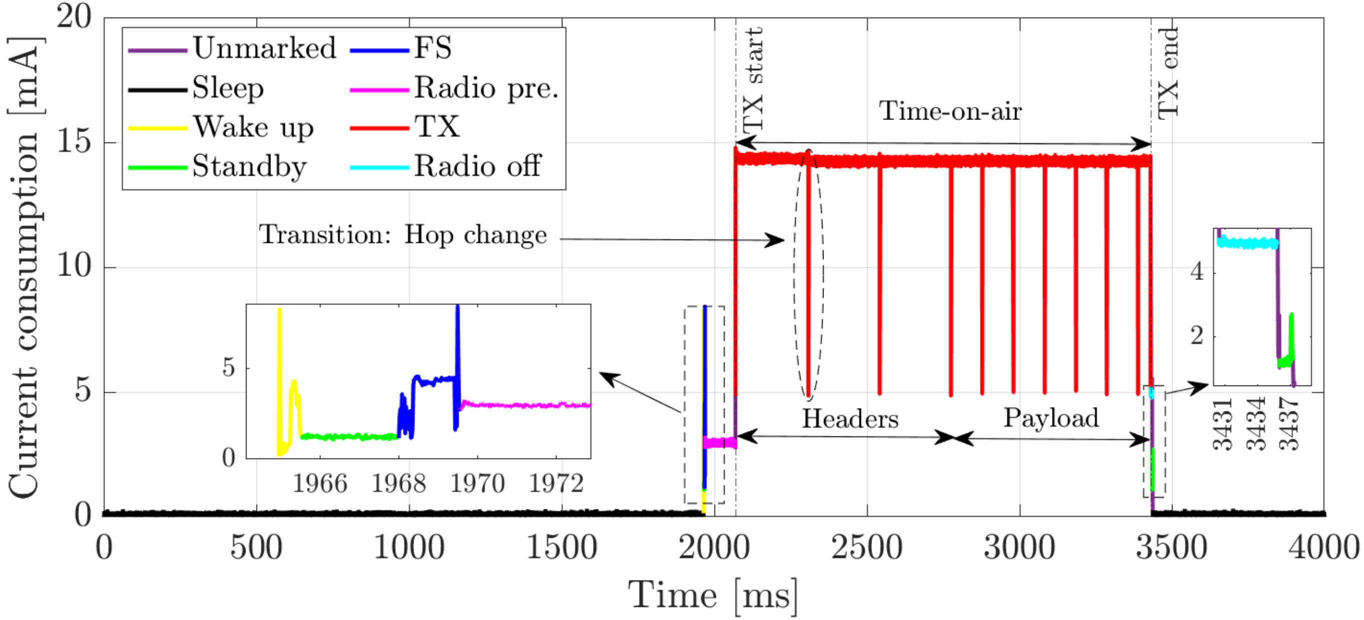

Fig. 30. The LR-FHSS current consumption for an illustrative packet transmission with different states of transmissions color-marked according to the operational modes shown in Fig. 26.

Table 10. LR-FHSS states during packet transmission, their duration, and average current consumption

State	State	Duration T_i		Current I_i	
no. i	name	sym	ms	sym	mA
1	Wake up	T_{wu}	0.4301	I_{wu}	1.9
2	Standby	T_{std}	Fig. 31	I_{std}	1.229
3	Frequency Synthesis	T_{fs}	Fig. 31	I_{fs}	3.7392
4	Radio Preparation	T_{pre}	99.67	I_{pre}	2.968
5	Transmission	T_{tx}	(33)	I_{tx}	Fig. 29
6	Radio off	T_{off}	9.45	I_{off}	4.94
7	Standby	T'_{std}	1.044	I'_{std}	1.229
8	Sleep	T_{sleep}	(42)	I_{sleep}	0.053

Specifically, in Fig. 30, one can see that initially, the device is in *sleep* mode, which has the lowest current consumption of $I_{sleep} = 0.053$ mA. To transmit a packet, the device *wakes up* (State 1) and enters the default *standby* mode (State 2). Notably, the duration of this state depends on the payload, as reported in Fig. 31. However, it is worth mentioning that the average current consumption in the *standby* state remains a constant $I_{std} = 1.229$ mA, irrespective of the payload size, DRs, and P_{tx} levels. Subsequently, the device engages in *frequency synthesis* named State 3. Similar to the *standby* mode (State 2), the duration of the *frequency synthesis* mode depends on the payload size as shown in Fig. 31.

The LR1120 device prepares the radio packet for transmission in the next phase. The measurement results reveal that the duration and current consumption of the *radio preparation* mode (State 4) remain consistent around $T_{pre} = 99.67$ ms $I_{pre} = 2.968$ mA across all configurations.

Following this, the device initiates the packet *transmission* (State 5), which has the highest current consumption compared to the other states. The current consumption is directly influenced by the selected transmit power level. The duration of the *transmission* state corresponds to the packet ToA, which is influenced by the payload size and the chosen DRs. From the measurements, we note that LR-FHSS exhibits an average transition time of $T_T = 0.61$ ms to switch the OBW channel for the next hop, as illustrated in Fig. 32. However, it is important to note that the total transition time experienced during packet transmission depends on the number of header replicas and payload fragments. To accurately model the LR-FHSS ToA, it is crucial to consider the total transition time.

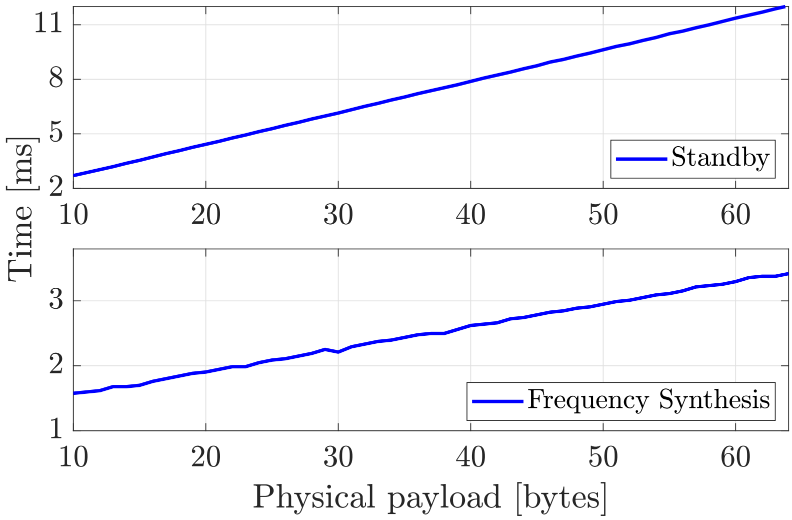

Fig. 31. The impact of the payload size on the timings of the *standby* and *frequency synthesis* modes.

Upon completing the transmission, the device transitions to the *radio off* mode (State 6) and returns to the default *standby* mode (State 7). Unlike the initial *standby* mode (State 2), the duration of the final *standby* state remains consistent across different configurations and payload sizes. Finally, the device returns to the *sleep* mode (State 8). Unlike LoRa, LR-FHSS is designed to support uplink transmissions only. Therefore, in experiments, the receiving windows were disabled, and our measurement does not account for the current consumption in the receive mode. This chapter analyzes and models the current consumption during the transmit process of LR-FHSS modulation. Notably, the LR-FHSS-enabled devices can use LoRa modulation for downlink communication. Therefore, existing LoRa ToA and energy consumption models [101, 102] can be used for the downlink analysis.

6.4 Proposed models

The research work of this chapter is grounded in real LR-FHSS measurement results presented in Section 6.3 and references to Semtech documents [87] and the LR1120 software [86]. This information is used to develop accurate analytical models for LR-FHSS ToA and current consumption.

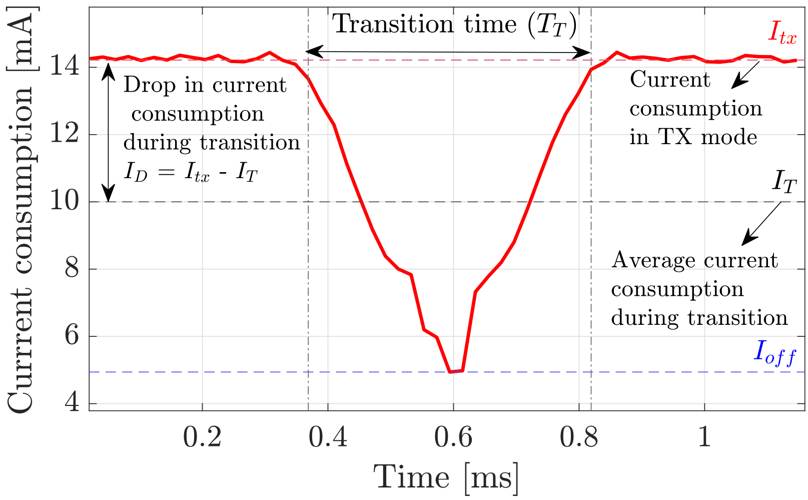

Fig. 32. The transition time between the hop changes during the intra-packet frequency hopping.

6.4.1 Air time modeling

This work considers ToA as the total time required to transmit all the encoded bits, including the header, payload, preambles, and CRC, at a given bit rate R_b. Additionally, the proposed ToA model accounts for the transition time T_T required to switch the OBW channels during frequency hopping, as illustrated in Fig. 32. The proposed model takes into account these facts to calculate the total ToA as

$$T_{tx} = \frac{P_B}{R_b} + T_T N_T, \tag{33}$$

where $N_T = N_H + N_F - 1$ is the number of transitions between the OBW channels for intra-packet frequency hopping, and P_B is the total number of encoded bits in an LR-FHSS packet calculated as

$$P_B = H_b N_H + P_L, \tag{34}$$

where H_b is the number of bits in a single header, N_H is the number of header replicas, P_L represents the total number of encoded payload bits in the LR-FHSS packet including the preamble ($P_b = 2$ bits) for each payload fragment as

$$P_L = P'_L + P_b N_F, \tag{35}$$

here P_L' denotes the number of payloads plus CRC bits after the FEC coding, i.e.,

$$P_L' = \frac{8(L+P_{CRC})}{\text{CR}} + O_B, \tag{36}$$

in this equation L is uncoded physical layer payload in bytes, and $O_B = 6$ denotes the number of overhead bits defined in the LR-FHSS software [114]. Finally, the number of payload fragments N_F in an LR-FHSS packet is given by

$$N_F = \left\lceil \frac{P_L'}{48} \right\rceil. \tag{37}$$

6.4.2 Current consumption modeling

LR-FHSS uses multiple OBW channels for intra-packet frequency hopping during a single transmission. Each transition between OBW channels, known as a hopping shift, requires a transition time (T_T). It is important to note that the current consumption undergoes a substantial reduction during these transitions, reaching as low as $I_{off} =$ 4.94 mA, as demonstrated in Fig. 32. This aspect is accounted for in the current study to model the current consumption behavior of LR-FHSS transmissions accurately.

Let $N_{\text{states}} = 8$ be the number of states, T_i and I_i represent the duration and current consumption of these states as given in Table 10. Thus, the total average current consumption becomes

$$\overline{I_{\text{avg}}} = \frac{T_{\text{active}}.I_{\text{active}} + T_{\text{sleep}}.I_{\text{sleep}}}{T_{\text{notification}}}, \tag{38}$$

$$= \frac{1}{T_{\text{notification}}} \left(\sum_{i=1}^{N_{\text{states}}} T_i.I_i - T_T.I_D.N_T \right), \tag{39}$$

where I_D accounts for the total drop in current consumption during the OBW channel changes for intra-packet frequency hopping as

$$I_D = I_{tx} - \overline{I_T}, \tag{40}$$

where $\overline{I_T}$ is the average current consumption during the transition time T_T. In Fig. 32, the drop in current from I_{tx} to I_{off} and then raise in current from I_{off} to I_{tx} exhibit a triangle shape. Using the triangle centroid formula, the equation for the average current consumption $\overline{I_T}$ can be expressed as

$$\overline{I_T} = \frac{I_{tx} + I_{off} + I_{tx}}{3}. \tag{41}$$

In (38) and (39), $T_{\text{notification}}$ is the reporting period (R_p), the time between two consecutive periodic transmissions calculated as

$$T_{\text{notification}} = T_{\text{sleep}} + T_{\text{active}}, \tag{42}$$

where T_{active} represents the total duration of all active states combined.

$$T_{\text{active}} = T_{wu} + T_{std} + T_{fs} + T_{pre} + T_{tx} + T_{off} + T'_{std}. \tag{43}$$

Next, these results can be used to estimate, e.g., the theoretical lifetime of operation of the battery. For example, if assuming a linear battery model, the lifetime is given by:

$$T_{\text{lifetime}} = \frac{C_{\text{battery}}}{\overline{I_{\text{avg}}}}, \tag{44}$$

where C_{battery} is the battery capability expressed in mAh. Note that (44) estimates the maximum lifespan of an ideal battery; however, real-world batteries degrade and experience a decline in their rated capacity over time.

6.5 Analytical results

Fig 33 shows the LR-FHSS ToA as a function of a variable payload. The ToA values obtained from the proposed analytical model closely align with the experimental measurements, confirming the validity of the developed model. However, the existing state-of-the-art *Model I* [62] reports up to 55 ms higher ToA than the results obtained from the proposed analytical model and measured data. Conversely, *Model II* [88, 90] gives a ToA which is approximately 47 ms lower. The lower section of Fig. 33 reveals the relative error of ToA from different models relative to the measurement results. One can see that the proposed analytical ToA model features the lowest relative error, which is only 0.3%. For 10 bytes payload, *Model I* and *Model II* demonstrate maximum errors of -9.2% and 3.4%, respectively. These differences and fluctuations are mainly due to the mathematical formulation of (2) and (3). Specifically, the *Model I* depicts sawtooth behavior because (2) does not account for the fact that the last payload fragment could be shorter than 102.4 ms. Thus, this model introduces significant inaccuracy. Notably, the relative maximum error gradually decreases with the increase of the payload size for all the models. The proposed approach reveals the best performance among these models, demonstrating the smallest relative error as it accounts for the transition time T_T.

Fig. 34 compares the average current consumption $\overline{I_{\text{avg}}}$ during one packet transmission obtained from the measurement and proposed analytical model as a function of variable transmit power. The results reveal a strong correlation, thereby confirming the

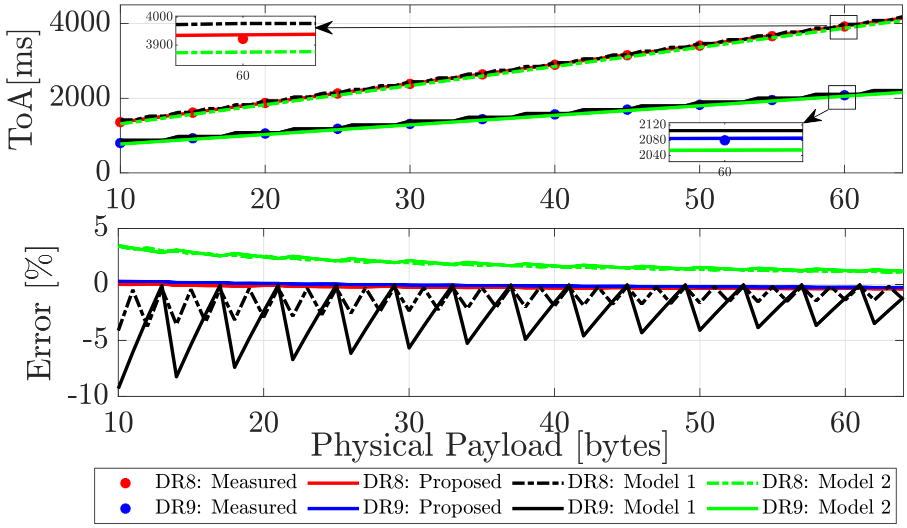

Fig. 33. The top section of the figure compares the ToA results obtained from the measurements, the proposed model, and the state-of-the-art models [62, 88, 90] as a function of a variable payload. The bottom part of the figure reveals the error percentage when compared

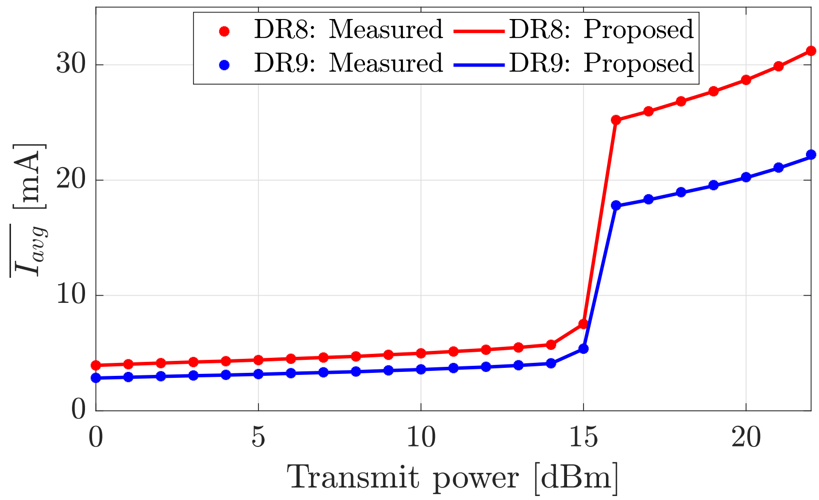

Fig. 34. Comparison of measured and analytical average current consumption ($\overline{I_{avg}}$) for single packet transmission as a function of transmit power (P_{tx}).

accuracy of our LR-FHSS current consumption model. To my knowledge, no available research or literature presents a current consumption model for LR-FHSS. Therefore, these results cannot be compared to any other model.

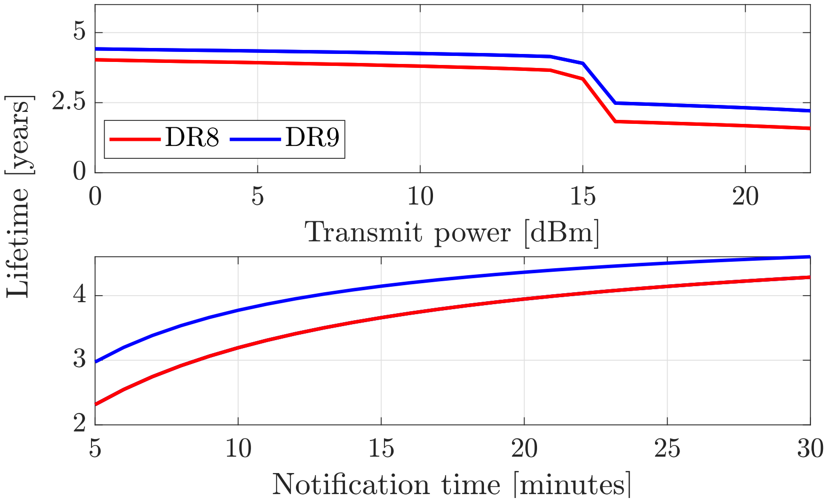

Fig. 35. The subplot at the top presents the battery theoretical lifetime for 10 bytes LR-FHSS transmission as a function of transmit power and 5 minutes notification time. The lower subplot applies a constant 14 dBm transmit power and variable notification time.

Finally, this chapter theoretically evaluates the battery life of an LR-FHSS-enabled device. The upper chart of Fig. 35 presents the theoretical battery life as a function of variable transmission power. The configuration assumes the end device transmits 10 bytes packets every 15 minutes. DR9 demonstrates a better lifetime owing to lower ToA. For both DRs, the battery lifetimes remain above 3.6 years up to a transmit power of 14 dBm. However, when the transmit power exceeds 14 dBm, and the device begins employing HPA, the battery life gradually decreases to almost half - nearly 2.2 and 1.58 years for DR8 and DR9, respectively, at the maximum transmit power.

More than this, the lower chart of Fig. 35 illustrates how the battery lifespan changes based on the notification time ($T_{\text{notification}}$). As expected, the results show that a longer $T_{\text{notification}}$ increases the battery life. Specifically, when using 5 minutes intervals, the battery remains operational for approximately 2.3 and 3 years for DR8 and DR9, respectively. However, with a 30 minutes notification interval, the battery's lifespan exceeds 4.2 years.

6.6 Generality of results

At the time of our experiments, only LR1120 model development kits were commercially available. Therefore, we used this model for measurements. In Fig. 30, our measurement results reveal that the time duration and current consumption both change across different operational states. In future LR-FHSS end device models, the current consumption in the *transmission* (S_TX) mode may be different than our measurements, particularly if the future models use different power amplifiers and radio designs. These possible variations can be added to the proposed analytical model with slight modifications. LR1121 [115] is a new LR-FHSS end device, and it exhibits the same power consumption characteristics as LR1120 (refer to Table 3-6: Transmit Mode Power Consumption of LR1120 in [116] and LR1121 in [115]). ToA mainly depends on the modulation scheme, therefore, we expect that the proposed ToA analytical model will remain valid for the future LR-FHSS device models, regardless of potential variations in current consumption.

6.7 Summary and discussion

LR-FHSS is emerging as a potential connectivity solution for battery-powered and tiny satellite IoT end devices operating in hard-to-reach areas. Replacing an end device's battery in remote industrial or fragile natural areas, e.g., offshore wind farms to give just one illustrative example, is challenging and costly. This chapter focuses on the LR-FHSS time and energy profiles and provides important insights for further studies. The main contributions of this chapter are the LR-FHSS current consumption and the ToA analytical models based on real experimental measurements. First, extensive measurements were conducted for variable transmit powers, data rates, and message payload sizes. The results offer valuable insights into the various system states associated with LR-FHSS transmissions, including their respective timing and current consumption characteristics. Importantly, this study identifies additional states, such as *Radio Preparation* and *Radio off*, which were not previously reported in the LR-FHSS-enabled LR1120 development kit user manual. Notably, the proposed ToA model demonstrates better accuracy than existing state-of-the-art models. Similarly, this work introduces the first analytical current consumption model for LR-FHSS, which estimates the battery lifetime as a function of a variable transmit power and the transmission notification time. The proposed models and results can be useful for further studies investigating the medium access control aspects and battery lifetime of LR-FHSS-enabled devices. They enable us to study the feasibility and performance of the applications (e.g., industrial use cases) based on them.

7 Conclusions and future work

7.1 Conclusion

This thesis explored the potential of massive machine-type communications and LEO satellite integration to enable global connectivity for IoT applications in remote areas. To this end, **Chapter 2** discusses the technical background of satellite communications systems and presents an overview of existing and potential technologies. Given the low-power, long-range, and cost-effective characteristics of LoRaWAN, this thesis advocates LoRa and LR-FHSS for mMTC and satellite integration for low data rate application. Therefore, **Chapter 2** provides the technical background of these two schemes, laying the foundation for modeling and performance analysis in the remaining chapters. Finally, this chapter conducts a state-of-the-art review to identify recent technological developments, research gaps, and open challenges concerning integrating LoRaWAN and LEO satellite systems. Among the major open challenges, this thesis focuses on the following:

1. The mobility of LEO satellites introduces a strong Doppler effect, resulting in time-varying Doppler shifts and rates. The Doppler effect presents significant challenges for successful packet reception on satellites.
2. Time-varying elevation angles affect the link distance (slant range) between a terrestrial end device and an LEO satellite. The link distance varies from 550 km to approximately 2,000 km depending on the elevation angle and orbital height. This long distance introduces significant path loss and attenuation, lowering the SNR.
3. A single satellite serves thousands of end devices within its coverage footprint. As a result, simultaneous transmissions from multiple end devices on the same channel introduce interference issues.
4. Due to the long link distance and absence of knowledge on the satellite location, the terrestrial end device transmits at the maximum allowed power. Therefore, it is vital to understand the current consumption characteristics and satellite IoT end device battery lifetime.

Considering these challenges, **Chapter 3** discusses two alternative network architectures, DtS and ItS, exploring potential configuration options while highlighting the pros, cons, and relevant trade-offs. It discusses the system model to evaluate the network performance accounting for the Doppler effect, massive interference, and high propagation losses. To align with the terrestrial LPWAN literature, the link level analysis defines the overall *success probability* in two components: (i) the *connection probability*, which measures whether the receiver SNR is more than the required SNR, and (ii) the *capture probability* which allows a signal to recover from collision and whether the SIR is more than the power threshold. This system model is the foundation for an in-depth performance analysis in **Chapter 5**.

Focusing on the Doppler effect, note that most previous studies present just the experimental results obtained by considering only a limited subset of the parameters. Second, the existing literature focuses mainly on a carrier frequency closer to the 433 MHz band, which experiences the least impact from the Doppler effect among those allowed for LoRaWAN. Third, to the best of the author's knowledge, the impact of the Doppler effect on LR-FHSS performance has not been examined as of today. There remains a need for an extensive and comprehensive examination of LoRa and LR-FHSS performance under a strong Doppler effect in the LEO scenario. **Chapter 4** addresses this shortcoming and develops an analytical framework to evaluate the LoRa and LR-FHSS performance considering the entire elevation angle range and variable communications parameters. The results reveal that the Doppler shift affects communication at lower elevation angles, while the Doppler rate primarily affects communication at higher elevation angles. These results from the proposed analytical framework can be useful in finding a suitable set of communication parameters for a given satellite orbit to combat the packet losses due to the Doppler effect.

For a link-level analysis, the developed model assumes that the satellite has a mechanism to estimate and compensate for the Doppler effect. Therefore, **Chapter 5** primarily focuses on investigating the link budget and scalability aspects using specially designed Monte Carlo simulators and analytical models. Notably, this is the first work focusing on LoRa and LR-FHSS's performance in LEO satellite links. To the author's knowledge, this is the first study to develop analytical and simulation models allow LR-FHSS scalability analysis. The *success probability* results obtained from the model presented in **Chapter 3** confirm the feasibility of both LoRa and LR-FHSS for DtS communications. **Chapter 5** analytically compares LoRa and LR-FHSS scalability for an illustrative use case scenario, namely situational awareness for ships. The LR-FHSS outperforms conventional LoRa modulation because it uses frequency hopping and features lower coding rates and redundant physical headers. LR-FHSS is a prominent choice for mMTC DtS connectivity to serve numerous IoT end devices in remote areas.

The IoT end devices envisioned for DtS connectivity are anticipated to operate on battery power. The task of replacing batteries in hard-to-reach areas poses considerable challenges and costs. Hence, it is vital to understand the current consumption characteristics of IoT end devices. The results in **Chapter 4** and **Chapter 5** confirm that LR-FHSS is robust to the Doppler effect and is promising for massive DtS communications. However, there is currently no existing work that discusses the current consumption characteristics of this modulation scheme. To this end, **Chapter 6** conducts experiments to measure the air time and current consumption of LR-FHSS modulation. The empirical results are used to develop analytical models for airtime and current consumption, which facilitates estimating the LR-FHSS end device's average battery life. These outcomes could serve as valuable inputs for accurate collision modeling and network optimization in future works.

Finally, the reported results confirm the potential feasibility of direct mMTC LPWAN end device to satellite communication even when employing network configurations typical for today's terrestrial LoRaWAN. This thesis introduces several research challenges and open questions that may offer additional guidance for future works. These results are expected to motivate further studies to conduct a more comprehensive and systematic analysis of such systems and their operations. This thesis also inspired multidisciplinary work pioneering a groundbreaking research topic known as underground direct-to-satellite (U-DtS) connectivity [54–56]. This thesis has developed and introduced Monte Carlo simulation and analytical models aimed at evaluating and addressing the challenges mentioned above. The script code for these models and LR-FHSS measurement data have been deposited on GitHub [49–53], thereby serving to facilitate the replication of the results and support future research.

7.2 Future work

The thesis confirms the feasibility and demonstrates the promising performance of LoRaWAN DtS communications, considering different design dimensions and configuration parameters. This motivates the further research and development of such systems to enable global connectivity for IoT in hard-to-reach areas. The results show that the DtS communications performance degrades due to poor SNR resulting from long-distance or LOS blockage. Developing a method for detecting LOS blocking and avoiding transmission when the communication channel is not optimal can substantially improve the efficiency of DtS communication, saving the scarce power and frequency resources available to IoT end devices. Additionally, we assume an ideal satellite pass, where the satellite directly passes over the end device. However, in actual scenario, satellite pass may not always reach 90° elevation angle. As a future work, we consider it worth investigating that how LoRaWAN DtS communications behaves when applying the real-world satellites trajectories.

Terrestrial LoRaWAN networks often employ an optional Adaptive Data Rate (ADR) mechanism to optimize network and device performance. ADR offers the opportunity to reduce interference, increase network capacity, and improve battery lifetime. However, the high velocity of LEO satellites and limited energy resources make ADR implementation challenging. A Doppler-enabled Adaptive Data Rate, i.e., SF allocation mechanism, is a promising topic for future research on LoRa DtS. The co-existence study of LoRa and LR-FHSS can be a perspective research direction.

Interference is one of the major challenges for DtS networks. One may think that some existing MAC protocol may solve this problem. However, there are several reasons why most classical terrestrial MAC protocols are not efficient enough to support massive DtS connectivity demands. The design of an optimal MAC protocol for satellite IoT applications is worth investigating.

In this thesis, the Doppler effect analysis does not incorporate considerations of channel characteristics, such as path loss, shadowing, and noise. LoRa and LR-FHSS Doppler analysis accounting for the noise, attenuation, and sensitivity are prospective research directions for future work. More than this, it is worth investigating how LoRa and LR-FHSS modulation behaves in the very LEO (VLEO) scenario. Notably, there is a lack of information about the specific thresholds for static and dynamic Doppler, which requires further investigation.

In **Chapter 6**, the LR-FHSS experimental setup uses an LR1120 modem to measure air time and current consumption. Future LR-FHSS end devices may employ different radios and amplifiers, potentially influencing current consumption. It is worth looking at the current consumption characteristics of forthcoming LR-FHSS device models. Additionally, comparing the current consumption and battery life of LoRa, NB-IoT, and RedCap technology is another interesting research direction.

Finally, it is also worth looking at integrating 3GPP technologies and satellites. RedCap recently added to 5G technology, offers higher data rates than LoRa and LR-FHSS. We are evaluating the feasibility of RedCap DtS communications theoretically and experimentally using software-defined radios. Within the scope of proprietary satellite technologies, SpaceX is a winner with more than 6,000 operational Starlink satellites today. Our ongoing investigation focuses on evaluating the capabilities and limitations of Starlink connectivity across various channel and usage scenarios. Furthermore, we consider the 3D network using terrestrial drones and satellites as a potential research direction.

References

[1] M. Jouhari, N. Saeed, M.-S. Alouini, and E. M. Amhoud, “A Survey on Scalable LoRaWAN for Massive IoT: Recent Advances, Potentials, and Challenges,” *IEEE Communications Surveys & Tutorials*, vol. 25, no. 3, pp. 1841–1876, 2023.

[2] N. H. Mahmood, H. Alves, O. A. López, M. Shehab, D. P. M. Osorio, and M. Latva-Aho, “Six Key Features of Machine Type Communication in 6G,” in *2020 2nd 6G Wireless Summit (6G SUMMIT)*, 2020, pp. 1–5.

[3] H. B. Salem, N. Kouzayha, A. E. Falou, M.-S. Alouini, and T. Y. Al-Naffouri, “Exploiting Hybrid Terrestrial/LEO Satellite Systems for Rural Connectivity,” in *GLOBECOM 2023 - 2023 IEEE Global Communications Conference*, 2023, pp. 4964–4970.

[4] M. Feldmann, J. A. Fraire, F. Walter, and S. C. Burleigh, “Ring Road Networks: Access for Anyone,” *IEEE Communications Magazine*, vol. 60, no. 4, pp. 38–44, 2022.

[5] J. A. Fraire, O. Iova, and F. Valois, “Space-Terrestrial Integrated Internet of Things: Challenges and Opportunities,” *IEEE Communications Magazine*, vol. 60, no. 12, pp. 64–70, 2022.

[6] J. Sedin, S. Gopinath, X. Lin, O. Liberg, T. Khan, E. Yavuz, and S. Euler, “5G Massive Machine Type Communication Performance in Non-Terrestrial Networks with LEO Satellites,” in *2021 IEEE Global Communications Conference (GLOBECOM)*, 2021, pp. 01–06.

[7] O. Kodheli *et al.*, “Satellite Communications in the New Space Era: A Survey and Future Challenges,” *IEEE Commun. Surv. Tutorials*, vol. 23, no. 1, pp. 70–109, 2021.

[8] M. Centenaro, C. E. Costa, F. Granelli, C. Sacchi, and L. Vangelista, “A Survey on Technologies, Standards and Open Challenges in Satellite IoT,” *IEEE Communications Surveys & Tutorials*, vol. 23, no. 3, pp. 1693–1720, 2021.

[9] D. C. Nguyen, M. Ding, P. N. Pathirana, A. Seneviratne, J. Li, D. Niyato, O. Dobre, and H. V. Poor, “6G Internet of Things: A Comprehensive Survey,” *IEEE Internet of Things Journal*, vol. 9, no. 1, pp. 359–383, 2022.

[10] X. Fang, W. Feng, T. Wei, Y. Chen, N. Ge, and C.-X. Wang, “5G Embraces Satellites for 6G Ubiquitous IoT: Basic Models for Integrated Satellite Terrestrial Networks,” *IEEE Internet of Things Journal*, vol. 8, no. 18, pp. 14 399–14 417, 2021.

[11] M. M. Azari, S. Solanki, S. Chatzinotas, O. Kodheli, H. Sallouha, A. Colpaert, J. F. Mendoza Montoya, S. Pollin, A. Haqiqatnejad, A. Mostaani, E. Lagunas, and B. Ottersten, “Evolution of Non-Terrestrial Networks From 5G to 6G: A Survey,” *IEEE Communications Surveys & Tutorials*, vol. 24, no. 4, pp. 2633–2672, 2022.

[12] F. Guo, F. R. Yu, H. Zhang, X. Li, H. Ji, and V. C. M. Leung, “Enabling Massive IoT Toward 6G: A Comprehensive Survey,” *IEEE Internet of Things Journal*, vol. 8, no. 15, pp. 11 891–11 915, 2021.

[13] J. A. Fraire *et al.*, “Direct-To-Satellite IoT - A Survey of the State of the Art and Future Research Perspectives,” in *Ad-Hoc, Mobile, and Wireless Networks*, M. R. Palattella, S. Scanzio, and S. Coleri Ergen, Eds. Cham: Springer International Publishing, 2019, pp. 241–258.

[14] G. M. Capez, S. Henn, J. A. Fraire, and R. Garello, “Sparse Satellite Constellation Design for Global and Regional Direct-to-Satellite IoT Services,” *IEEE Transactions on Aerospace and Electronic Systems*, vol. 58, no. 5, pp. 3786–3801, 2022.

[15] G. Álvarez, J. A. Fraire, K. A. Hassan, S. Céspedes, and D. Pesch, "Uplink Transmission Policies for LoRa-Based Direct-to-Satellite IoT," *IEEE Access*, vol. 10, pp. 72 687–72 701, 2022.

[16] P. Ilabaca, S. Céspedes, and S. Montejo-Sánchez, "Network Size Estimation in Direct-to-Satellite IoT," in *2021 IEEE 8th International Conference on Space Mission Challenges for Information Technology (SMC-IT)*, 2021, pp. 107–111.

[17] K. Vogelgesang, J. A. Fraire, and H. Hermanns, "Uplink Transmission Probability Functions for LoRa-Based Direct-to-Satellite IoT: A Case Study," in *2021 IEEE Global Communications Conference (GLOBECOM)*, 2021, pp. 01–06.

[18] S. Jung, S. Jeong, J. Kang, J. G. Ryu, and J. Kang, "Transceiver Design and Performance Analysis for LR-FHSS-Based Direct-to-Satellite IoT," *IEEE Communications Letters*, vol. 27, no. 12, pp. 3310–3314, 2023.

[19] S. Herrería-Alonso, M. Rodríguez-Pérez, R. F. Rodríguez-Rubio, and F. Pérez-Fontán, "Improving Uplink Scalability of LoRa-Based Direct-to-Satellite IoT Networks," *IEEE Internet of Things Journal*, pp. 1–1, 2023.

[20] S. Aslam, M. P. Michaelides, and H. Herodotou, "Internet of Ships: A Survey on Architectures, Emerging Applications, and Challenges," *IEEE Internet of Things Journal*, vol. 7, no. 10, pp. 9714–9727, 2020.

[21] T. Xia, M. M. Wang, and X. You, "Satellite Machine-Type Communication for Maritime Internet of Things: An Interference Perspective," *IEEE Access*, vol. 7, pp. 76 404–76 415, 2019.

[22] K. Mikhaylov, H. Alves, and M. Höyhtyä, "Drivers, use-cases, key indicators, and requirements for satellite-based machine type connectivity and IoT," in *39th Int. Commun. Satell. Syst. Conf.* Institution of Engineering and Technology IET, 2022.

[23] G. Pasolini, "On the LoRa Chirp Spread Spectrum Modulation: Signal Properties and Their Impact on Transmitter and Receiver Architectures," *IEEE Transactions on Wireless Communications*, vol. 21, no. 1, pp. 357–369, 2022.

[24] V. Y. Prokopyev *et al.*, "NORBY CubeSat nanosatellite: design challenges and the first flight data," *Journal of Physics: Conference Series*, vol. 1867, no. 1, p. 012038, apr 2021.

[25] TinyGS, "TinyGS, the Open Source Global Satellite Network," [Online]. Available: https://tinygs.com/satellites, 2023, accessed: Jan. 5, 2023.

[26] T. Ahmmed *et al.*, "The Digital Divide in Canada and the Role of LEO Satellites in Bridging the Gap," *IEEE Communications Magazine*, vol. 60, no. 6, pp. 24–30, 2022.

[27] H. Saarnisaari, S. Dixit, M.-S. Alouini, A. Chaoub, M. Giordani, A. Kliks, M. Matinmikko-Blue, N. Zhang, A. Agrawal, M. Andersson *et al.*, "A 6G white paper on connectivity for remote areas," *arXiv preprint arXiv:2004.14699*, 2020.

[28] A. Chaoub, M. Giordani, B. Lall, V. Bhatia, A. Kliks, L. Mendes, K. Rabie, H. Saarnisaari, A. Singhal, N. Zhang, S. Dixit, and M. Zorzi, "6G for Bridging the Digital Divide: Wireless Connectivity to Remote Areas," *IEEE Wireless Communications*, vol. 29, no. 1, pp. 160–168, 2022.

[29] P. Pirinen, H. Saarnisaari, J. van de Beek, M. Matinmikko-Blue, R. Nilsson, and M. Latva-aho, "Wireless Connectivity for Remote and Arctic Areas – Food for Thought," in *2019 16th International Symposium on Wireless Communication Systems (ISWCS)*, 2019, pp. 43–47.

[30] X. Lin, S. Cioni, G. Charbit, N. Chuberre, S. Hellsten, and J.-F. Boutillon, "On the Path to 6G: Embracing the Next Wave of Low Earth Orbit Satellite Access," *IEEE Communications Magazine*, vol. 59, no. 12, pp. 36–42, 2021.

[31] F. Rinaldi, H.-L. Maattanen, J. Torsner, S. Pizzi, S. Andreev, A. Iera, Y. Koucheryavy, and G. Araniti, "Non-Terrestrial Networks in 5G & Beyond: A Survey," *IEEE Access*, vol. 8, pp. 165 178–165 200, 2020.

[32] T. Xia, M. M. Wang, and X. You, "Satellite Machine-Type Communication for Maritime Internet of Things: An Interference Perspective," *IEEE Access*, vol. 7, pp. 76 404–76 415, 2019.

[33] S. Cioni, R. De Gaudenzi, O. Del Rio Herrero, and N. Girault, "On the Satellite Role in the Era of 5G Massive Machine Type Communications," *IEEE Network*, vol. 32, no. 5, pp. 54–61, 2018.

[34] A. A. Doroshkin *et al.*, "Experimental Study of LoRa Modulation Immunity to Doppler Effect in CubeSat Radio Communications," *IEEE Access*, vol. 7, pp. 75 721–75 731, 2019.

[35] G. Colavolpe *et al.*, "Reception of LoRa Signals From LEO Satellites," *IEEE Transactions on Aerospace and Electronic Systems*, vol. 55, no. 6, pp. 3587–3602, 2019.

[36] J. Kang *et al.*, "Regression based Pilot Design for Doppler Effect Estimation and Compensation in LEO Satellite Communication with LoRa," in *2022 27th Asia Pacific Conf. on Communications (APCC)*, 2022, pp. 631–632.

[37] A. Doroshkin, A. Zadorozhny, O. Kus, V. Prokopyev, and Y. Prokopyev, "Laboratory testing of LoRa modulation for CubeSat radio communications," in *MATEC Web of Conferences*, vol. 158. EDP Sciences, 2018, p. 01008.

[38] C. E. Fossa, R. A. Raines, G. H. Gunsch, and M. A. Temple, "An overview of the IRIDIUM (R) low Earth orbit (LEO) satellite system," *Proc. IEEE 1998 Natl. Aerosp. Electron. Conf. NAECON 1998. Celebr. 50 Years (Cat. No.98CH36185)*, pp. 152–159, 1998.

[39] H. Jia, Z. Ni, C. Jiang, L. Kuang, and J. Lu, "Uplink Interference and Performance Analysis for Megasatellite Constellation," *IEEE Internet of Things Journal*, vol. 9, no. 6, pp. 4318–4329, 2022.

[40] G. Pasolini, "On the LoRa Chirp Spread Spectrum Modulation: Signal Properties and Their Impact on Transmitter and Receiver Architectures," *IEEE Transactions on Wireless Communications*, vol. 21, no. 1, pp. 357–369, 2022.

[41] M. Asad Ullah, K. Mikhaylov, and H. Alves, "Massive Machine-Type Communication and Satellite Integration for Remote Areas," *IEEE Wireless Communications*, vol. 28, no. 4, pp. 74–80, 2021.

[42] ——, "Enabling mMTC in Remote Areas: LoRaWAN and LEO Satellite Integration for Offshore Wind Farm Monitoring," *IEEE Transactions on Industrial Informatics*, vol. 18, no. 6, pp. 3744–3753, 2022.

[43] ——, "Analysis and Simulation of LoRaWAN LR-FHSS for Direct-to-Satellite Scenario," *IEEE Wireless Communications Letters*, vol. 11, no. 3, pp. 548–552, 2022.

[44] M. Asad Ullah, A. Yastrebova, K. Mikhaylov, M. Höyhtyä, and H. Alves, "Situational Awareness for Autonomous Ships in the Arctic: mMTC Direct-to-Satellite Connectivity," *IEEE Communications Magazine*, vol. 60, no. 6, pp. 32–38, 2022.

[45] M. Asad Ullah, G. Pasolini, K. Mikhaylov, and H. Alves, "Understanding the Limits of LoRa Direct-to-Satellite: The Doppler Perspectives," *IEEE Open Journal of the Communications Society*, vol. 5, pp. 51–63, 2024.

[46] M. Asad Ullah, K. Mikhaylov, and H. Alves, "Experiment-based Models for Air Time and Current Consumption of LoRaWAN LR-FHSS," *IEEE Internet of Things Journal*, 2024, under review.

[47] M. A. Ullah, K. Mikhaylov, and H. Alves, "An Overview of Direct-to-Satellite IoT: Opportunities and Open Challenges," in *2023 IEEE 9th World Forum on Internet of Things (WF-IoT)*, 2023, pp. 1–8.

[48] M. Asad Ullah, F. Clazzer, A. Munari, K. Mikhaylov, and H. Alves, *An Overview of Medium Access Control Protocols in Machine-Type Communication Satellite Internet-of-Things Networks*. John Wiley & Sons, Ltd, 2024, ch. 6, pp. 119–146.

[49] Muhammad Asad Ullah, "Analysis and Simulation of LoRaWAN LR-FHSS," [Online]. Available: https://github.com/MuhammadAsadUllah1/Analysis-and-Simulation-of-LoRaWAN-LR-FHSS.git, 2021, accessed: Jan. 5, 2024.

[50] ——, "Situational Awareness for Autonomous Ships in the Arctic mMTC Direct-to-Satellite Connectivity," [Online]. Available: https://github.com/MuhammadAsadUllah1/Situational-Awareness-for-Autonomous-Ships-in-the-Arctic-mMTC-Direct-to-Satellite-Connectivity, 2021, accessed: Jan. 5, 2024.

[51] ——, "LoRaWAN and LEO-Satellite Integration for Offshore Wind Farms Monitoring," [Online]. Available: https://github.com/MuhammadAsadUllah1/LoRaWAN-and-LEO-Satellite-Integration-for-Offshore-WindFarms-Monitoring, 2021, accessed: Jan. 5, 2024.

[52] ——, "LoRa Direct-to-Satellite Connectivity: The Doppler Perspectives," [Online]. Available: https://github.com/MuhammadAsadUllah1/LoRa-Direct-to-Satellite-The-Doppler-perspectives, 2023, accessed: Jan. 5, 2024.

[53] ——, "LR-FHSS-air-time-and-current-consumption," [Online]. Available: https://github.com/MuhammadAsadUllah1/LR-FHSS-air-time-and-current-consumption.git, 2024, accessed: Jan. 5, 2024.

[54] K. Lin, M. Asad Ullah, H. Alves, K. Mikhaylov, and T. Hao, "Energy Efficiency Optimization for Subterranean LoRaWAN Using A Reinforcement Learning Approach: A Direct-to-Satellite Scenario," *IEEE Wireless Communications Letters*, pp. 1–1, 2023.

[55] ——, "Subterranean mMTC in Remote Areas: Underground-to-Satellite Connectivity Approach," *IEEE Communications Magazine*, pp. 1–7, 2022.

[56] ——, "Enabling Subterranean mMTC: LoRaWAN Underground-to-Satellite Connectivity for Urban Underground Pipelines Monitoring," *IEEE Internet of Things Journal*, under review.

[57] C. D. Gedara, M. D. Khattak, M. A. Ullah, and K. Mikhaylov, "Direct-to-Satellite Connectivity for IoT: Overview and Potential of Reduced Capability (RedCap)," in *2023 IEEE 9th World Forum on Internet of Things (WF-IoT)*, 2023, pp. 1–8.

[58] K. Lin and T. Hao, "Experimental Link Quality Analysis for LoRa-Based Wireless Underground Sensor Networks," *IEEE Internet of Things J.*, vol. 8, no. 8, pp. 6565–6577, 2021.

[59] M. Asad Ullah, M. Tayyab, N. Mangalvedhe, R. Ratasuk, and S. Lee, "Conditional Device-to-Device Communications," *(Patent Application No. 63/526,256)*, Jul 2023.

[60] N. Saeed, A. Elzanaty, H. Almorad, H. Dahrouj, T. Y. Al-Naffouri, and M.-S. Alouini, "CubeSat Communications: Recent Advances and Future Challenges," *IEEE Communications Surveys & Tutorials*, vol. 22, no. 3, pp. 1839–1862, 2020.

[61] H. Al-Hraishawi, H. Chougrani, S. Kisseleff, E. Lagunas, and S. Chatzinotas, "A Survey on Nongeostationary Satellite Systems: The Communication Perspective," *IEEE Communications Surveys & Tutorials*, vol. 25, no. 1, pp. 101–132, 2023.

[62] *RP2-1.0.3 LoRaWAN®Regional Parameters*, LoRa Alliance, May 2021.

[63] *AN1200.64 LR-FHSS System Performance*, Semtech Corporation, Oct 2022.

[64] M. Höyhtyä, S. Boumard, A. Yastrebova, P. Järvensivu, M. Kiviranta, and A. Anttonen, "Sustainable Satellite Communications in the 6G Era: A European View for Multilayer Systems and Space Safety," *IEEE Access*, vol. 10, pp. 99 973–100 005, 2022.

[65] *Technical report (TR) 38.811, Study on New Radio (NR) to support non-terrestrial networks*, 3GPP, Oct 2020.

[66] G. Y. HAN Jiren, "General Introduction of Non-Terrestrial Networks for New Radio," *ZTE Communications*, vol. 20, no. S1, p. 72, 2022.

[67] F. Granelli, R. Bassoli, J. Nötzel, F. H. P. Fitzek, H. Boche, N. L. S. da Fonseca, and A. Guerrieri, "A Novel Architecture for Future Classical-Quantum Communication Networks," *Wirel. Commun. Mob. Comput.*, vol. 2022, jan 2022.

[68] S. Ma, Y. C. Chou, H. Zhao, L. Chen, X. Ma, and J. Liu, "Network Characteristics of LEO Satellite Constellations: A Starlink-Based Measurement from End Users," in *IEEE INFOCOM 2023 - IEEE Conference on Computer Communications*, 2023, pp. 1–10.

[69] A. Yastrebova-Castillo, M. Höyhtyä, M. Majanen, T. Ojanpera, J. Scholliers, and S. J. Rantala, "Improving the safety of autonomous driving by using Direct-to-Satellite connectivity: the case of Iridium and Starlink satellite constellations," in *IEEE Conference on Standards for Communications and Networking, CSCN 2023*, 2023.

[70] M. Conti, A. Guidotti, C. Amatetti, and A. Vanelli-Coralli, "NB-IoT over Non-Terrestrial Networks: Link Budget Analysis," in *GLOBECOM 2020 - 2020 IEEE Global Communications Conference*, 2020, pp. 1–6.

[71] *Technical specifications (TS) 38.101-5, NR; User Equipment (UE) radio transmission and reception; Part 5: Satellite access Radio Frequency (RF) and performance requirements*, 3GPP, January 2024.

[72] *Technical report (TR) 38.741, Non-Terrestrial Networks (NTN) L-/S-band for NR*, 3GPP, January 2024.

[73] S. Boumard, I. Moilanen, M. Lasanen, T. Suihko, and M. Höyhtyä, "A Technical Comparison of Six Satellite Systems: Suitability for Direct-to-Device Satellite Access," in *2023 IEEE 9th World Forum on Internet of Things (WF-IoT)*, 2023, pp. 01–06.

[74] *Technical report (TR) 38.875, Study on support of reduced capability NR devices*, 3GPP, March 2021.

[75] *Technical report (TR) 38.865, Study on further NR RedCap UE complexity reduction*, 3GPP, September 2022.

[76] A. Hoeller *et al.*, "Analysis and Performance Optimization of LoRa Networks With Time and Antenna Diversity," *IEEE Access*, vol. 6, pp. 32 820–32 829, 2018.

[77] A. Mahmood, E. Sisinni, L. Guntupalli, R. Rondón, S. A. Hassan, and M. Gidlund, "Scalability Analysis of a LoRa Network Under Imperfect Orthogonality," *IEEE Transactions on Industrial Informatics*, vol. 15, no. 3, pp. 1425–1436, 2019.

[78] J. M. de Souza Sant'Ana *et al.*, "LoRa Performance Analysis with Superposed Signal Decoding," *IEEE Wireless Communications Letters*, vol. 9, no. 11, pp. 1865–1868, 2020.

[79] J. M. d. S. Sant'Ana, A. Hoeller, R. D. Souza, S. Montejo-Sánchez, H. Alves, and M. d. Noronha-Neto, "Hybrid Coded Replication in LoRa Networks," *IEEE Transactions on Industrial Informatics*, vol. 16, no. 8, pp. 5577–5585, 2020.

[80] A. M. Zadorozhny *et al.*, "First Flight-Testing of LoRa Modulation in Satellite Radio Communications in Low-Earth Orbit," *IEEE Access*, vol. 10, pp. 100 006–100 023, 2022.

[81] J. A. Fraire, A. Guitton, and O. Iova, "Recovering Headerless Frames in LR-FHSS," *arXiv*, 2023.

[82] Semtech, "SX1276/77/78/79 - 137 MHz to 1020 MHz Low Power Long Range Transceiver," `https://www.semtech.com/products/wireless-rf/lora-connect/sx1276`, May 2020, accessed: Jan. 5, 2023.

[83] ——, "AN1200.59 Selecting the Optimal Reference Clock," `https://www.semtech.com/products/wireless-rf/lora-connect/sx1276`, July 2022, accessed: Jan. 5, 2024.

[84] G. Boquet *et al.*, "LR-FHSS: Overview and Performance Analysis," *IEEE Communications Magazine*, vol. 59, no. 3, pp. 30–36, 2021.

[85] M. Asad Ullah, K. Mikhaylov, and H. Alves, “Analysis and Simulation of LoRaWAN LR-FHSS for Direct-to-Satellite Scenario,” *IEEE Wireless Communications Letters*, vol. 11, no. 3, pp. 548–552, 2022.
[86] Semtech, “LR1120 Transceiver User Manual,” [Online] Available: https://www.semtech.com/products/wireless-rf/lora-edge/lr1120, 2022, accessed: May 25, 2023.
[87] SEMTEC, “Application Note: LoRa® Modulation Crystal Oscillator Guidance ,” `https://www.semtech.com/products/wireless-rf/lora-connect/sx1276`, July 2019, accessed: Jan. 5, 2024.
[88] A. Maleki, H. H. Nguyen, and R. Barton, “Outage Probability Analysis of LR-FHSS in Satellite IoT Networks,” *IEEE Communications Letters*, vol. 27, no. 3, pp. 946–950, 2023.
[89] G. Boquet *et al.*, “LR-FHSS: Overview and Performance Analysis,” *IEEE Communications Magazine*, vol. 59, no. 3, pp. 30–36, 2021.
[90] A. Maleki, H. H. Nguyen, E. Bedeer, and R. Barton, “D2D-aided LoRaWAN LR-FHSS in Direct-to-Satellite IoT Networks,” *arXiv*, 2022.
[91] J. Petäjäjärvi, K. Mikhaylov, M. Pettissalo, J. Janhunen, and J. H. Iinatti, “Performance of a low-power wide-area network based on LoRa technology: Doppler robustness, scalability, and coverage,” *International Journal of Distributed Sensor Networks*, vol. 13, 2017.
[92] Y. Li, S. Han, L. Yang, F.-Y. Wang, and H. Zhang, “LoRa on the Move: Performance Evaluation of LoRa in V2X Communications,” in *2018 IEEE Intelligent Vehicles Symposium (IV)*, 2018, pp. 1107–1111.
[93] R. M. Colombo, A. Mahmood, E. Sisinni, P. Ferrari, and M. Gidlund, “Low-cost SDR-based Tool for Evaluating LoRa Satellite Communications,” in *2022 IEEE Int. Symposium on Measurements & Networking (M&N)*, 2022, pp. 1–6.
[94] J. M. Marais, A. M. Abu-Mahfouz, and G. P. Hancke, “A Survey on the Viability of Confirmed Traffic in a LoRaWAN,” *IEEE Access*, vol. 8, pp. 9296–9311, 2020.
[95] J. P. Shanmuga Sundaram, W. Du, and Z. Zhao, “A Survey on LoRa Networking: Research Problems, Current Solutions, and Open Issues,” *IEEE Communications Surveys & Tutorials*, vol. 22, no. 1, pp. 371–388, 2020.
[96] M. Centenaro, L. Vangelista, and R. Kohno, “On the impact of downlink feedback on LoRa performance,” in *2017 IEEE 28th Annu. Int. Symp. Pers. Indoor, Mob. Radio Commun.*, 2017, pp. 1–6.
[97] F. Van den Abeele, J. Haxhibeqiri, I. Moerman, and J. Hoebeke, “Scalability Analysis of Large-Scale LoRaWAN Networks in ns-3,” *IEEE Internet of Things Journal*, vol. 4, no. 6, pp. 2186–2198, 2017.
[98] M. Urakami, N. Wakabayashi, and T. Watanabe, “A Study on Location Information Screening Method for Ship Application Using AIS Recorded Data,” in *2018 International Conference on Broadband Communications for Next Generation Networks and Multimedia Applications (CoBCom)*, 2018, pp. 1–6.
[99] A. K. Dwivedi, S. Chaudhari, N. Varshney, and P. K. Varshney, “Performance analysis of LEO satellite-based IoT networks in the presence of interference,” *IEEE Internet of Things Journal*, 2023.
[100] C. Gomez, S. M. Darroudi, H. Naranjo, and J. Paradells, “On the energy performance of iridium satellite IoT technology,” *Sensors*, vol. 21, no. 21, p. 7235, 2021.
[101] L. Casals, B. Mir, R. Vidal, and C. Gomez, “Modeling the energy performance of LoRaWAN,” *Sensors*, vol. 17, no. 10, p. 2364, 2017.
[102] T. Bouguera, J.-F. Diouris, J.-J. Chaillout, R. Jaouadi, and G. Andrieux, “Energy consumption model for sensor nodes based on LoRa and LoRaWAN,” *Sensors*, vol. 18, no. 7, p. 2104, 2018.

[103] R. K. Singh, P. P. Puluckul, R. Berkvens, and M. Weyn, "Energy consumption analysis of LPWAN technologies and lifetime estimation for IoT application," *Sensors*, vol. 20, no. 17, p. 4794, 2020.

[104] S. Cakaj *et al.*, "The Range and Horizon Plane Simulation for Ground Stations of Low Earth Orbiting (LEO) Satellites." *Int. J. Commun. Netw. Syst. Sci.*, vol. 4, no. 9, pp. 585–589, 2011.

[105] A. W. Doerry, "Earth curvature and atmospheric refraction effects on radar signal propagation." Sandia National Lab.(SNL-NM), Albuquerque, NM (United States), Tech. Rep., 2013.

[106] O. Georgiou and U. Raza, "Low Power Wide Area Network Analysis: Can LoRa Scale?" *IEEE Wireless Communications Letters*, vol. 6, no. 2, pp. 162–165, 2017.

[107] Semtech, "SX1268 Long Range, Low Power, sub-GHz RF Transceiver," `https://www.semtech.com/products/wireless-rf/lora-connect/sx1268`, June 2019, accessed: Jan. 5, 2024.

[108] C. A. Hofmann, K.-U. Storek, and A. Knopp, "Impact of Phase Noise and Oscillator Stability on Ultra-Narrow-Band-IoT Waveforms for Satellite," in *ICC 2021 - IEEE International Conference on Communications*, 2021, pp. 1–6.

[109] G. Boquet, P. Tuset-Peiró, F. Adelantado, T. Watteyne, and X. Vilajosana, "LR-FHSS: Overview and Performance Analysis," *IEEE Communications Magazine*, vol. 59, no. 3, pp. 30–36, 2021.

[110] C. Goursaud and Y. Mo, "Random unslotted time-frequency ALOHA: Theory and application to IoT UNB networks," in *2016 23rd International Conference on Telecommunications (ICT)*, 2016, pp. 1–5.

[111] J. Kim, C.-Y. Yang, and J. Jang, "Performance analysis of low-Earth-orbit (LEO) mobile-Satellite system using moment-based approximation of degradation factors," *IEEE Transactions on Vehicular Technology*, vol. 55, no. 3, pp. 876–886, 2006.

[112] P. A. Berkman *et al.*, "Baseline of Next-Generation Arctic Marine Shipping Assessments - Oldest Continuous Pan-Arctic Satellite Automatic Identification System (AIS) Data Record of Maritime Ship Traffic, 2009-2016," [Online]. Available: https://arcticdata.io/catalog/view/doi:10.18739/A2BV79W4V, 2016.

[113] Semtech, "Application Note: LR11xx Program Memory Upgrade," [Online]. Available: https://www.semtech.com/products/wireless-rf/lora-edge/lr1120, 2022, accessed: May 25, 2023.

[114] ——, "Drivers and Demos for Long-Range Frequency Hopping Spread Spectrum (LR-FHSS)," [Online]. Available: https://github.com/Lora-net/SWDM001, 2022, accessed: May 25, 2023.

[115] ——, "LR1121 Long Range, Low Power, Multi-band LoRa® Transceiver," [Online]. Available: https://www.semtech.com/products/wireless-rf/lora-connect/lr1121, 2023, accessed: Nov. 16, 2023.

[116] ——, "LR1120 Low Power Wi-Fi/ GNSS Scanner & Multi-band LoRa® Transceiver," [Online]. Available: https://www.semtech.com/products/wireless-rf/lora-edge/lr1120, 2023, accessed: Nov. 16, 2023.

Appendix 1 Algorithm for the impact of the Doppler effect

LoRa DtS performance under the Doppler effect for the entire visibility interval $-\frac{V_T}{2} \leq t \leq \frac{V_T}{2}$.

Algorithm 1 LoRa DtS performance under Doppler effect

Input: E , B , F_C, LDRO, SF, P_L, H
Initialization: $S_{\text{loss}} = 0$, $D_{\text{loss}} = 0$, $J_{\text{loss}} = 0$
Constants: $R = 6371$ km, $g = 9.80665$ m/s²
$V_T \leftarrow$ satellite total visibility time calculated by (7)
ToA $\leftarrow$ LoRa Time on Air depends on P_L
$F_{\text{static}} \leftarrow$ Doppler shift tolerance threshold by (18)
$F_{\text{dynamic}} \leftarrow$ Doppler rate tolerance threshold by (19)
$t = -\frac{V_T}{2} \leftarrow$ Initialization of the interval
while $t \leq \frac{V_T}{2}$ **do**
    $F_D(t) \leftarrow$ Doppler shift calculated by (8)
    $\Delta F_D(t) \leftarrow$ Doppler rate calculated by (9)
    $\Delta F_E(t) \leftarrow$ Total frequency change during packet transmission by (22)
    $L_{\text{static}}(t) \leftarrow$ Packet status under Doppler shift calculated by (20)
    $L_{\text{dynamic}}(t) \leftarrow$ Packet status under Doppler rate calculated by (21)
    $L_{\text{joint}}(t) \leftarrow$ Packet status under Doppler shift and rate as $L_{\text{static}}(t) \times L_{\text{dynamic}}(t)$
    if $L_{\text{static}}(t) == 1$ **then**
        S_{loss}++; ▷ Packet fail due to Doppler shift
    end if
    if $L_{\text{dynamic}}(t) == 1$ **then**
        D_{loss}++; ▷ Packet fail due to Doppler rate
    end if
    if $L_{\text{joint}}(t) == 1$ **then**

        J_{loss}++; ▷ Packet fail due to both Doppler shift and rate
    end if
    t++; ▷ Step increment of the time
end while
Output: $L_{\text{static}}(t)$, $L_{\text{dynamic}}(t)$, $L_{\text{joint}}(t)$

946. Singh, Sumit Pratap (2024) Radio receiver front-end ICs at the sub-THz/THz frequency range in silicon technology
947. Asgari, Somayyeh (2024) Theoretical and numerical studies of dynamically tunable terahertz graphene-based chiral and anisotropic metamaterials
948. Järvinen, Topias (2024) Sensor applications of MoS_2 and WS_2 thin films
949. Autio, Anna (2024) Integrated modelling of groundwater-surface water interactions in the boreal landscape
950. Büngener, Lina (2024) The fate of nitrogen and microplastics as wastewater contaminants in treatment wetlands under cold climate conditions
951. Sun, Zhaodong (2024) Facial video-based non-contact physiological signal measurement and applications
952. Tahir, Muhammad Naeem (2024) Advanced vehicular communications through cellular and short-range networks exploiting road weather and traffic observation data
953. Ren, Zhongfei (2024) Adsorption and advanced oxidation/reduction process for elimination of per- and polyfluoroalkyl substances and pharmaceutical pollutants in water
954. Beddiar, Djamila Romaissa (2024) Deep learning-based automatic captioning for medical imaging
955. Zhao, He (2024) Bismuth halide perovskites as photocatalysts for hydrogen production
956. Kaksonen, Rauli (2024) Transparent and tool-driven security assessment for sustainable IoT cybersecurity
957. Yastrebova-Castillo, Anastasia (2024) LEO satellite constellations for autonomous system operation in the Arctic region : situational awareness and communication aspects
958. Airaksinen, Susanna (2024) Oxide scale formation of stainless steel in transition of annealing and reheating towards fossil-free methods
959. Bahador, Nooshin (2024) Assessment of neurological function with multimodal and multichannel physiological signal analysis using machine and deep learning techniques
960. Akbar, Rehman (2024) CMOS integrated wideband, flexible and scalable beamforming architecture

Book orders:
Virtual book store
https://verkkokauppa.omapumu.com/fi/

UNIVERSITY OF OULU P.O. Box 8000 FI-90014 UNIVERSITY OF OULU FINLAND

ACTA UNIVERSITATIS OULUENSIS

UNIVERSITY OF OULU

ISBN 978-952-62-4199-9 (Paperback)
ISBN 978-952-62-4200-2 (PDF)
ISSN 0355-3213 (Print)
ISSN 1796-2226 (Online)